DESIGNING BETTER INDUCTION MOTOR DRIVE SYSTEMS FROM EFFICIENCY, RELIABILITY, AND POWER ELECTRONICS PERSPECTIVES

BY

ALI MOHAMAD BAZZI

DISSERTATION

Submitted in partial fulfillment of the requirements
for the degree of Doctor of Philosophy in Electrical and Computer Engineering
in the Graduate College of the
University of Illinois at Urbana-Champaign, 2010

Urbana, Illinois

Doctoral Committee:

Professor Philip T. Krein, Chair
Adjunct Associate Professor Patrick L. Chapman
Assistant Professor Alejandro Dominguez-García
Associate Professor Daniel M. Liberzon
Professor Peter W. Sauer

ABSTRACT

This dissertation addresses the design of better induction motor drives from several perspectives. Loss minimization in the machine using real-time optimization methods is studied thoroughly. These methods are categorized and discussed in detail, with special emphasis on the application of ripple correlation control for induction motor loss minimization. The effect of these methods on the overall drive reliability is studied. A complete reliability model considering machine, power electronics, and sensor faults is developed, and a safe-mode controller is chosen to achieve better drive reliability. Loss estimation in power electronics is also addressed in order to achieve system-level loss minimization and design more reliable inverters with better electro-thermal properties.

Loss minimization results show that average energy savings exceed 5% in applications such as propulsion and hybrid vehicles. This amount is significant when global energy savings are considered and when the savings are translated to monetary equivalents or reductions in emissions and generation. The effect of loss minimization techniques on the drive reliability is shown to be minimal where the drive maintains over 50 years of expected time to failure. The addition of safe-mode control to mitigate sensor faults enhances closed-loop control reliability and improves it to be closer to a more-reliable open-loop controller while maintaining the desired closed-loop transient response. The loss estimation tool is shown to predict losses in IGBT-diode pairs within an average of 8% error under both periodic and aperiodic switching. These results are essential to design more reliable inverters with appropriate component sizing and better thermal management.

The final outcome of this dissertation is a minimum-loss and highly reliable induction motor drive system for current and future applications.

In The Name of God, Most Gracious, Most Merciful

To My Mother and Father

ACKNOWLEDGMENTS

I am grateful to my adviser, Prof. Philip T. Krein, for his guidance and support, and for giving me the opportunity to join his research group. Reading several of his papers encouraged me to apply to the University of Illinois to work under his supervision. The acceptance e-mail and offer letter I received on March 28th, 2007, were life changing. Joining the power and energy group at the University of Illinois for my Ph.D. studies was a dream come true. Working with Prof. Krein opened wide doors of opportunities that I would have never been able to pursue without his help. I learned from him not only proper research methodologies and how to make ideas and innovations come true, but also how to be a patient teacher, tolerant supervisor, and concise writer. I am indebted to Prof. Krein for all the knowledge, responsibilities, and opportunities that he gave me.

I am thankful to all the other committee members for their help and guidance. I am very thankful to Prof. Sauer, whose advice and support in my job applications were very valuable. Prof. Sauer's presentation and teaching skills, and kind and fatherly attitude towards students, will always be my guides throughout any future teaching endeavor. I always discussed research ideas with Prof. Chapman, from whom I learned how to think about challenges in special ways. His advice was always enlightening in courses and research. Prof. Dominguez-García taught me reliability theory and triggered my enthusiasm to pursue research in this field. His knowledge and personality were great incentives for me to collaborate with him on different projects. Prof. Daniel Liberzon, my first teacher at the University of Illinois, introduced me to adaptive control. I learned from Prof. Liberzon very interesting ways of teaching graduate courses.

I could not have joined the University of Illinois without the generous funding from the National Science Foundation, Office of Naval Research, Grainger Center for Electric Machinery

and Electromechanics, Power Affiliates Program, and Mavis Memorial Scholarship. I would also like to thank the Grainger Center staff, Joyce Mast and Kevin Colravy, and all my undergraduate assistants, especially Kieran Levin, Sanghun Choi, Eric Hofreiter, and Xiangyu Ding, for their valuable help. I am thankful to all my friends at the University of Illinois who made me feel at home away from home. I would like to specifically mention Pradeep Shenoy, who has always been there for both personal and technical advice and discussions, and Rami Abdallah.

I am also grateful to my master's thesis adviser at the American University of Beirut (AUB), Prof. Sami Karaki, who supported me throughout my undergraduate and graduate studies, and whose research guidance and recommendations were extremely helpful throughout my professional life. I am indebted to Prof. Karaki for all his kind help. I am thankful to Dean Ibrahim Hajj at AUB for his encouragement and support to join the University of Illinois. I am also thankful to Prof. Hazem Chahine at AUB for his valuable support and advice.

Last but not least, I am grateful to my family, especially my mother Shadia and father Mohamad, who always encouraged me to pursue the Ph.D. I am indebted to my late grandmother Nahdiya and thankful to my great uncle Abdulkarim for his support. For my mother, this Ph.D. is a dream come true. She is the dearest and most valuable person in my life, and a true friend who has sacrificed greatly for the sake of my future, education, and welfare. No matter what I say, I cannot express how grateful I am for all her sacrifices. To my father, who sacrificed decades of his life for the well-being of our family, I will always be grateful. My parents' love, support, and encouragement always helped me move forward in good and hard times.

TABLE OF CONTENTS

CHAPTER 1

INTRODUCTION

1.1 Overview

Machines have been widely used in different grid-connected and stand-alone applications with variable complexities. Simple applications include pumps, fans, compressors, etc., while more complex applications include electric vehicles (EVs) [1, 2], hybrid electric vehicles (HEVs) [3], airplane oil pumps, ship propulsion systems, and others. In general, machines constitute over 50% of the grid-connected electric load [4, 5]. Industry publications, e.g. [6], report that motors consume 60% of the electrical energy in industries and infrastructures, 30% of the energy in buildings, and 85% of the energy of pumps, fans, and compressors worldwide. In standalone and transportation applications, energy storage devices store excess energy to supply the load once the mainstream energy is not available. Storage devices have limited capacity, and improving the efficiency of the machine would draw less power from any storage device so that the stored energy would last longer.

The shift towards energy-saving motor drives has been mainly driven by the depletion of oil and gas reserves, growing economies, and increased greenhouse-gas emissions. According to [6], the load will double while CO_2 emissions should be cut by half by the year 2050. Since machines constitute the main load in grid-connected and off-grid applications, energy savings in machines would reduce the global energy consumption, slow down the rate of depletion of non-renewable resources, and reduce greenhouse gas emissions from power plants and transportation vehicles.

Three main components constitute any motor drive system: machine, power electronics, and control. From a system-level perspective, improvements can be applied to one or more of

these three components. Such improvements include loss reduction in the machine or power electronics, voltage and current quality, fault tolerance and detection, optimal component sizing, improved component and overall drive reliability, cost effectiveness, drive size, and others. The driven load sets the priority of improvements. For example, in an all-electric airplane, safety is a major concern and is directly linked to reliability and fault tolerance of essential electric drives; in such an application, cost of redundant components is not a major concern. Also, in any system, system-level tradeoffs arise and can be modeled as multi-variable optimization problems. For example, reducing the flux in a machine reduces losses and increases efficiency; but, if such a machine is operating an EV and high torque is desired, the EV will stall because such high torques cannot be maintained at a low flux level. An overview of essential design aspects follows here: loss minimization in the machine, drive reliability, and improved thermo-electric power electronics designs. Further details about essential drive system design are given in Section 2.1.

Induction machines are most commonly used among machines due to their simple construction and control, robustness, and low cost. Therefore, minimizing losses in induction machines would be a major step towards minimizing the global electric load and energy consumption. Whether this loss minimization is possible or not depends on whether the machine losses can be pushed lower without affecting the driven load. While machines are designed for their highest efficiency at the rated load, most machines run under light loading conditions due to conservative designs or variable loads. An example of a 1.5 hp efficiency curve is given in Fig. 1. It is clear from Fig. 1 that when the machine is operating at light loads, its efficiency degrades significantly. This implies that there is room for loss minimization or efficiency enhancement in that region.

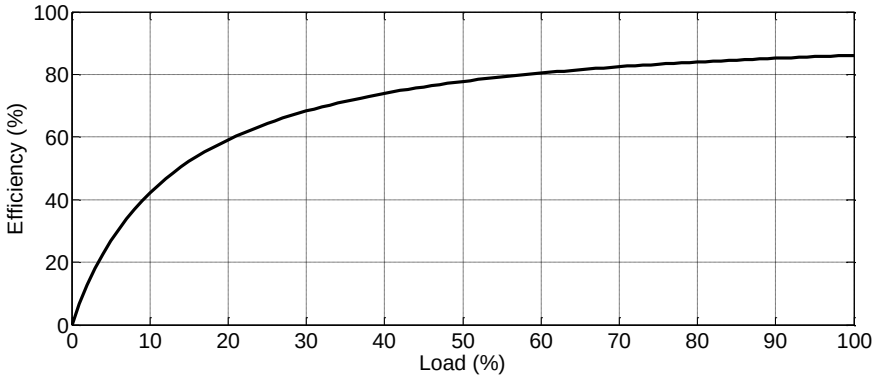

Fig. 1. Typical efficiency vs. load curve for a 1.5 hp induction machine

Loss minimization in induction machines has been studied for several years [7, 8], and it is usually built around available drive features, e.g., voltage and current measurements. Adding loss minimization algorithms or techniques to the drive could increase complexity, require estimation, or jeopardize the load. For example, the minimum motor input power (P_{in}) and power loss (P_{loss}) are $P_{in} = P_{loss} = 0$ W under unconstrained optimization. Then, the load is not supported and the machine does not operate. Since loss minimization techniques (LMTs) utilize a control variable to achieve minimum P_{in} or P_{loss}, drive reliability can be assessed by sweeping over the control variable and analyzing the system response under faults [9]. Two important factors should be considered: First, the drive reliability should not be affected by loss minimization under faults. Second, the load should be considered before applying loss minimization, with the most straightforward approach being constrained optimization.

The most common faults in a motor drive occur in power electronics. These are usually related to overheating, thermal management problems, or thermal fatigue [10]. Since thermal management of power electronics is usually designed based on power losses, accurate loss estimation is desired. This estimation is well established in the literature but with ideal

assumptions regarding current waveforms, switching frequencies, and other operational considerations. In real induction motor drives, these assumptions might not hold.

1.2 Problem Statement

There is a basic need for more efficient and reliable induction motor drive systems for current and future applications.

1.3 Research Statement

This dissertation provides a comprehensive overview of induction motor LMTs where they are categorized, characterized, compared, applied in common practical applications, and analyzed from a reliability perspective. Ripple correlation control (RCC), a real-time ripple-based optimization technique, is studied as a hybrid LMT. The effect of LMTs on drive reliability under machine, power electronics, and sensor faults is studied. Reliability analysis is extended to different induction motor control methods and a systematic reliability modeling procedure is developed. A safe-mode controller is identified. In all LMT and reliability analyses, simulations, and experiments, indirect FOC (IFOC) is used as the controller. A loss estimation tool for insulated-gate bipolar transistors (IGBTs) and diodes is developed for periodic and aperiodic switching. Better power loss estimates from the tool are expected to improve electro-thermal designs and enhance the drive reliability with and without LMTs.

The work is organized as follows: Chapter 2 provides a literature review of system-level design considerations of drives, LMTs, RCC, reliability modeling, and loss estimation in IGBTs and diodes. Chapter 3 elaborates on RCC as extremum-seeking (ES) control and as an LMT with operational challenges at high frequencies and possible solutions. Chapter 4 presents an example

of commercial energy-saving drives, and LMTs in more advanced applications, specifically a propulsion system and an HEV. Simulation and experimental results are shown. Drive reliability modeling is presented in Chapter 5 where the mathematical preliminaries of the modeling procedure are presented, a simulation model is experimentally validated, and reliability functions with mean-time-to-failure (MTTF) estimates are found. A safe mode is also discussed in Chapter 5. Chapter 6 describes an IGBT-diode loss estimation tool for better thermo-electric power electronics designs and fewer thermal failures in motor drives due to overheating or inaccurate loss estimation. Conclusions and open research questions are presented in Chapter 7.

CHAPTER 2

LITERATURE REVIEW

2.1 Design Considerations for Induction Motor Drive Systems

It is not a straightforward task to survey all design aspects in induction motor drives as the importance of every aspect, except fundamental requirements, varies from one application to another.[1] For example, in traction applications, reliability is a major concern, but cost is more important for mass production of small pumps. Design requirements affect the three subsystems of an induction motor drive: machine, power electronics, and control and sensing. A better overall drive can be achieved through design improvements in each subsystem.

Studies that consider the selection of motor drives are an important source of information for design criteria. Motor selection criteria include efficiency, cost, size, power density, reliability, torque quality, and number of poles (which affects the frequency and speed requirements). Control and sensor requirements include the number of sensors, cost, and robustness. Power electronics requirements include efficiency, size, reliability, and cost. For example, design criteria for an EV drive [11], compressor [12], traction [13], and general high-performance variable frequency drives (VFDs) [14, 15], are available. Fundamental design "themes" for the whole drive can be noticed and they include the drive efficiency, reliability, cost, and size.

Induction machine and power electronics efficiencies set the overall drive efficiency and cooling requirements. Machine losses and their physical concentrations are analyzed in [16], and design considerations in induction machines are shown in [17]. Loss minimization and analysis techniques are elaborated upon in [18, 19], and a literature review of loss minimization in

[1] Much of the material in this chapter relates to the work presented in [9], [18], [19], [171], and [182]. Thus, copyright notices are added on figures and tables presented in these references and shown here.

induction machines is presented in Section 2.2. Thermal management of losses affects drive reliability. An example of the interaction between power electronics and the machine is analyzed for different switching patterns in the inverter [20].

Drive reliability of the drive is a combination of the machine, power electronics, and control and sensing reliabilities. Comparison of different drives with reliability and other considerations is presented in [21]. Reliability-related examples include fault detection and diagnosis [22, 23], fault tolerant drives [24], and fault reduction or prevention, e.g., voltage transient reduction in cable-connected drives [25-27]. A literature review on reliability of induction motor drives is presented in Section 2.3. Control, sensing, and estimation design issues are also widely discussed throughout the literature as they affect the reliability, operation, and load support. Examples include the design of robust controllers in motor drives [28], state and parameter estimation [29, 30], and stability analysis of the controller [31].

Cost is always a decisive factor. Two major cost categories are component cost and energy cost. While energy cost is related to energy consumption and thus losses, component costs depend on their physics, ratings, and other manufacturing characteristics. In general, components with higher power ratings, complex manufacturing processes, and higher efficiency cost more. While minimum cost is always desired, some applications that require special power electronics devices, machine material, thermal management, or protection and redundancy, sacrifice the cost factor for better efficiency, reliability, and performance. The size and weight of any drive are usually products of the allowed thermal and power limits. For example, cooling a 250 kW inverter with a large blower requires significantly more volume than a liquid-cooled cold plate or heat sink. In an experimental laboratory environment, the inverter volume and thermal management are not a major issue, but in an EV, the volume is very limited.

Therefore, as in any design process, design tradeoffs always arise. The importance of efficiency, reliability, cost, and size are variable from one application to another, but the ultimate goal of a better design is to increase the efficiency and reliability, and reduce the cost and size. From an electrical design perspective, efficiency and reliability enhancements can be thoroughly addressed while keeping in mind that the cost and size do not increase.

2.2 Loss Minimization in Machines

2.2.1 Overview

Loss minimization techniques minimize P_{in} or P_{loss} in a machine. For a given output power (P_o), $P_{in} = P_o + P_{loss}$ and therefore at any instant of time, minimizing P_{loss} is equivalent to minimizing P_{in} at that instant. From an energy perspective, the energy in a machine has an extra storage term,

$$E_{in} = E_o + E_{loss} + E_{stored}, \tag{1}$$

where E_{in}, E_o, E_{loss}, and E_{stored} are the input, output, lost, and stored energies, respectively. LMTs must address only loss. They have been applied to several machines including induction machines, permanent magnet synchronous machines (PMSMs), e.g. [32], and switched reluctance machines, e.g. [33]. As induction machines dominate industrial, residential, and transportation applications, the focus here is on LMTs for them. LMTs have not been widely commercialized, and those augmented into commercial drives could be replaced with more advanced methods. The choice of the LMT is related to the application and drive capabilities where applications require a different LMT convergence speed, parameter sensitivity, and convergence error. For example, a simple water pump running at a constant flow can be preset to operate at a minimum loss for that load, but vehicles that run dynamic urban cycles with abrupt

braking and acceleration require more advanced and dynamic LMTs. The choices of the drive and controller also affect the choice of an LMT where controllers have different inputs that could be used as loss-minimization control variables.

Induction machine applications can be steady-state or dynamic depending on the load variability (ρ), defined as

$$\rho = k_L \frac{\partial T_L}{\partial t}, \tag{2}$$

where k_L is a constant, T_L is the load torque, and t is time. Dynamic applications such as electric vehicle drives have large ρ, while steady-state applications such as cooling fans have small ρ. Convergence time requirements of LMTs are highly affected by ρ— when ρ is large, the LMT must converge quickly to provide energy savings. When ρ is small, the response time of the LMT is not a major issue as it will have enough time to converge. Also, LMTs could depend on machine parameters and converge to a sub-optimal operating point due to errors in the parameter estimates. In a dynamic application, these errors could be less important as any energy savings achieved with fast convergence are useful; but, in steady-state applications, sub-optimal operation accumulates significant energy losses. Examples of dynamic applications include HEVs, electric ship propulsion [34], aircraft launchers and electric cranes which require short bursts of large amounts of energy. Examples of steady-state or low-variability applications include fans, steady-flow pumps, and even air conditioning pumps with slight load variations due to minor temperature changes.

Two major LMT categories exist: offline and online (or real-time) [18, 19]. Offline techniques include designing the motor for lower losses. Such designs address loss minimization from a structural perspective using electromagnetic field theory to set the shapes of the rotor and

stator in addition to the wiring distribution, material, and overall size. Another offline approach is setting the controller operating point at the minimum power loss for the rated or most frequent load. For example, in a field-oriented control (FOC) or vector drive, the machine flux is set to an "optimal" value based on expected operating conditions. Another method is a factory-defined mapping that defines desired flux as a predetermined function of load. In general, offline techniques cannot adjust losses while the drive is running. Exceptions include preset look-up tables that update the control variable based on a pre-defined loss model while checking if the load is supported. Optimal operating points are stored in the controller memory for a specific machine, e.g. [8] where ω_{sl} is the control variable that is adjusted for every load. A similar look-up table is also used in [35] where the optimal V/f ratio is selected based on motor parameters and dynamic equations, but these parameters are static and might be inaccurate or vary. Thus, offline LMTs are usually inaccurate and cannot set the drive to operate at the exact minimum-loss point. More details about offline LMTs and power loss analysis using electromagnetic simulations are available in [19].

Real-time LMTs utilize use information about operation and machine parameter estimates to minimize losses continuously while the drive is running, as shown in Fig. 2. In induction machines, the control variable could be the flux, voltage, current, slip frequency, or combinations. The three categories of online LMTs are [18, 19] model-based, physics-based, and hybrids that combine these. Model-based LMTs depend on motor parameters and power-loss models. Physics-based LMTs utilize feedback and search for the minimum-loss operating point. Hybrid LMTs use both motor parameters and feedback. From this classification, LMTs can be compared based on convergence speed to the minimum loss, sensitivity to motor parameter errors, and accuracy in tracking the minimum power point.

LMT categories are summarized in Fig. 3. For example, reference [36] divides these methods into “methods based on [an] induction motor loss model” and “methods based on search controllers of [the] minimum [power loss].” Reference [37] categorizes LMTs as “simple state control” such as power factor control, “model-based control,” and “search control.” The classifications in [36, 37] are similar to model- and physics-based LMTs but ignore hybrid methods. Hybrid LMTs were first identified as an independent category in [18], and more related elaborate discussions are available here and in [19].

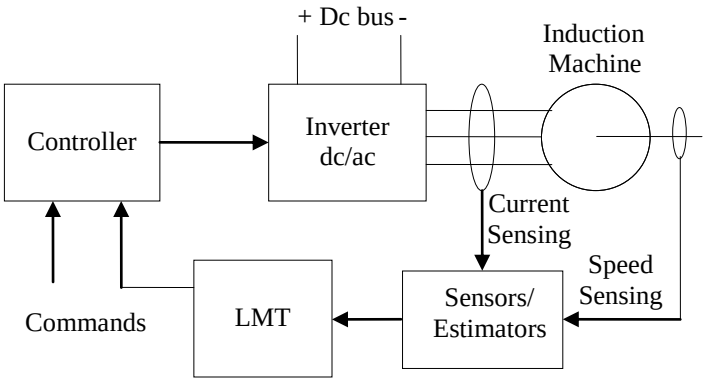

Fig. 2. Induction motor drive with an LMT

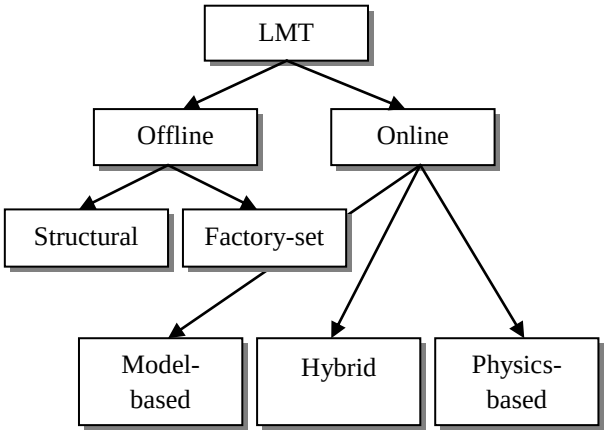

Fig. 3. LMT categories ©2010 IEEE

2.2.2 Commercial Energy-Saving Techniques

Most commercial induction motor drives are applied to fans and pumps. In variable pump applications, affinity laws show that P_{in} is proportional to the cube of rotational speed; therefore at low loads or speeds, P_{in} can be significantly reduced from the rated value while maintaining the load. Using a motor drive, machine currents, voltages, and frequency can be controlled. Whether the drive is open- or closed-loop, reducing the flux can reduce P_{in} or P_{loss}. An example of P_{in} vs. the d-axis rotor flux (λ_{dr}) is shown in Fig. 4 for a 1.5 hp induction machine at a single torque-speed operating point.

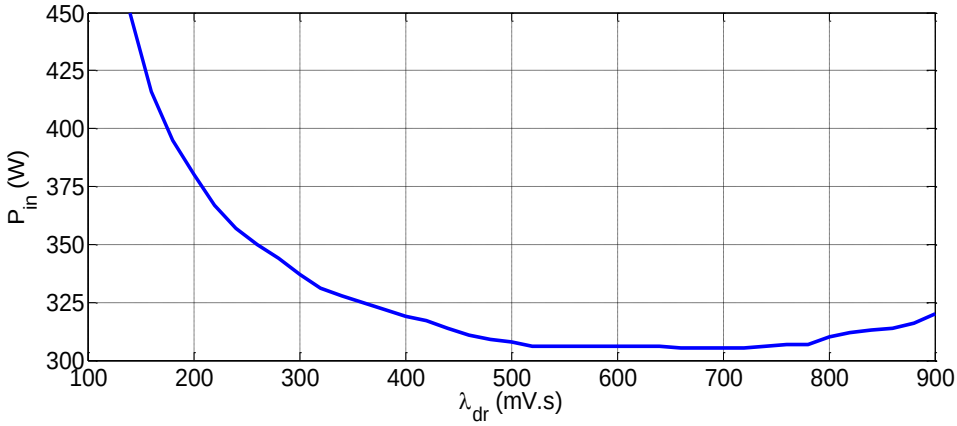

Fig. 4. P_{in} vs. λ_{dr} for a 1.5 hp induction machine at 2 N·m and 1000 rpm ©2010 IEEE

Flux reduction is a well-known method to save energy in induction motor drives. It can be applied in both open- and closed-loop drives — in open-loop or volts per hertz (V/f) drives, the V/f ratio approximates the magnetizing flux in the machine and can be reduced, while in close-loop (FOC or vector) drives, the flux command can be reduced. In this section, elaboration is given on commercial open-loop drives, and similar procedures are applied to closed-loop drives.

In an open-loop drive, the frequency sets the machine reference speed and is maintained at a desired reference value. Flux reduction to save energy can thus be achieved by reducing the

voltage. But at low voltages, flux reduction may cause the loss of load support, and the machine would stall. Therefore, in commercial drives such as [38], the load is always checked through estimators. This control can be summarized as shown in Fig. 5.

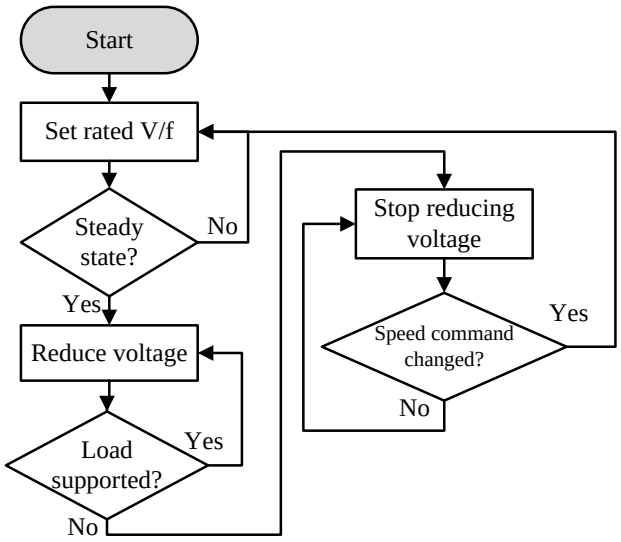

Fig. 5. Flow chart of voltage-control energy-saving method

Temperature feedback is used in heating, ventilation, and air conditioning (HVAC) to reduce the flux while maintaining temperature. An example is the adaptive energy optimization (AEO) by Danfoss which adjusts the pump speed to maintain the temperature within a desired band [39]. Another commercial energy-saving voltage control is available in Siemens drives where the voltage is reduced, thus reducing the current until the current starts to increase [40]. Several Yaskawa drives, e.g., E7, have two energy-saving modes: a manual tuning and automatic search. According to [41], the factory setting or "energy saving coefficient" can be manually set depending on the drive capacity. Further adjustment can be achieved with manual tuning. Another option is to use the automatic search, which slightly adjusts the machine voltage from the factory setting and avoids stalling the machine.

Since commercial energy-saving methods check for load support and reduce the flux iteratively, their response time is usually slow and could take minutes, especially when the drive updates its commands after waiting for steady state. Load estimation could introduce another drawback if it is machine-parameter dependent because any errors in the parameter estimates could cause load estimation error, which in turn could cause the system to stall with an under-estimated load. Approaches that monitor the speed for load information are parameter independent and therefore have no parameter sensitivity. If used, manual tuning of the energy-saving method is a drawback, especially under variable loads.

Sections 2.2.3 – 2.2.5 introduce the main characteristics and examples of model-based, physics-based, and hybrid LMTs, while Section 2.2.6 compares them based on the literature. Section 4.5 compares LMTs under the same operating conditions.

2.2.3 Model-Based Techniques

Model-based techniques utilize models of P_{loss} to estimate losses and then minimize them; thus, they depend on motor parameters. They can be defined as follows:

Definition 1: A *model-based LMT* depends on motor parameters and a power-loss or input power model to achieve minimum loss operation. It does not include closed-loop power measurement or estimation but might use other feedback [19].

There are two sources of error in motor parameter estimates: machine parameter tests have limited accuracy, and parameters can vary during operation due to physical effects such as temperature, saturation, etc. Errors in motor parameter estimates lead to sub-optimal operation. While several model-based LMTs use fixed parameter estimates, e.g. [4, 42-48], parameters can be updated online through look-up tables, e.g. [8], or through estimators, e.g. [49-51]. The model

of P_{loss} can be dependent on the stator resistance (R_s) [4], both R_s and the rotor resistance (R_r), or on all parameters including stator inductance (L_s), rotor inductance (L_r), magnetizing inductance (L_m), and core resistance (R_c) [47]. The magnetizing current is used as the control variable in [4], while the slip frequency (ω_{sl}) is used in [47] where simulations show tracking of the "theoretical" optimal ω_{sl} without comparison to nominal operating conditions. A similar approach to [47] where the steady-state motor model is used and ω_{sl} is the control variable is presented in [48]. But, in [48] the system is linearized around ω_{sl} and is independent of L_s. The magnetizing flux (λ_m) is used in [44] as the control variable where the model is dependent on R_s, R_r, and L_m. The LMT in [42] uses the stator current as the control variable and is dependent on R_s, R_r, L_m, and R_c. Sensitivity analyses in [42] show that variations in R_r are critical but lead to a 2% increase of the optimal power loss. The stator current is also used to minimize losses in [45, 46]. Another important control variable is the rotor flux (λ_r) and its direct-axis component λ_{dr}, e.g. [49, 52]. More details about the use of λ_{dr} and how that relates to Fig. 4 are shown in [53].

As mentioned earlier, look-up tables are static but machine parameters might vary during operation. Thus, some look-up tables that utilize online parameter estimates can be considered as model-based LMTs. For example, R_r and L_m are estimated in [49] to update a look-up table, and genetic algorithms are used in [51] to set the optimal V/f ratio (λ_m). Another way to update motor parameters is shown in [50] where physics-based parameter models are used (dependent on the load, temperature, etc.) to modify the stator current. Other model-based LMTs include those based on neural networks that use a P_{loss} model for the learning and correcting phases [54], and those based on optimal control theory [43] which have a model of the cost function.

Table 1 [18, 19] shows examples of P_{loss} models with their minimization variables (x) that are used in some model-based LMTs. In Table 1, k_1, k_2, k_3, k_4, and k_5, are defined in [47],

and k_e, k_h, k_{str} and k_{fw} are the eddy current, hysteresis, stray, and friction and windage loss coefficients, respectively; ω_r, ω_s (or ω_e) are the rotor and stator frequencies, respectively; R_{qls} is the q-axis core resistance, L_d is the d-axis self-inductance, T_e is the electromechanical torque, i and V are currents and voltages, respectively; subscripts q, d, s, and r, stand for q-axis, d-axis, stator, and rotor variables, respectively; and n_p is the number of poles.

Table 1. Some power loss functions and their relative minimization variables

P_{loss}	x
$\left(R_s+\frac{R_{qls}R_r}{R_{qls}+R_r}\right)i_{qs}^2+\left(R_s+\frac{L_d^2}{R_{qls}+R_r}\omega_s^2\right)i_{ds}^2$ [42, 45, 50]	i_{ds}
$i_s^2R_s+i_r^2R_r+\frac{V_m{}^2}{R_c}$ [35, 51]	V_s/ω_s
$R_s(i_{qs}^2+i_{ds}^2)+R_c(i_{qs}-i_r)^2+R_ri_r^2$ [4]	i_{ds}
$T_e\left\{\begin{array}{l}\left[\frac{2}{n_p}\left(\frac{R_s}{R_r}\left(\frac{L_r}{L_m}\right)^2+1\right)+k_eR_r\frac{2}{n_p}\left(\frac{L_m}{L_r}\right)^2\right]\omega_{sl}+\left[\frac{2}{n_p}\left(\frac{R_s}{R_r}\left(\frac{L_r}{L_m}\right)^2+1\right)\left(\frac{R_r}{L_r}\right)^2+\frac{2}{n_p}\left(\frac{R_r}{L_r}\right)^2+k_hR_r\left(\frac{L_m}{L_r}\right)^2\omega_r+k_eR_r\frac{n_p}{2}\left(\frac{L_m}{L_r}\right)^2\omega_r^2\right]\frac{1}{\omega_{sl}}+\\ \frac{2}{n_p}k_hR_r\left(\frac{L_m}{L_r}\right)^2+\omega_rn_pk_eR_r\frac{2}{n_p}\left(\frac{L_m}{L_r}\right)^2-\frac{4R_r}{n_pL_r}\sqrt{1+\frac{1}{\omega_{sl}^2}\left(\left(\frac{R_r}{L_r}\right)^2-1\right)}\end{array}\right.$ [48]	ω_{sl}
$i_r^2\left(\left(1+\frac{2L_{lr}}{L_m}\right)R_s+R_r+k_{str}\omega_r^2\right)+\lambda_m^2\left(k_e\omega_r^2+k_h\omega_r+\frac{R_s}{L_m^2}\right)+k_{fw}\omega_r^2$ [44]	λ_m
$k_m\left(k_1\omega_{sl}^3+k_2\omega_{sl}^2+k_3\omega_{sl}+k_4+\frac{k_5}{\omega_{sl}}\right)$ [47]	ω_{sl}
$\frac{3}{2}\left(\left(R_s+\left(k_h\omega_s+k_e\omega_s^2\right)L_m^2\right)\lvert i_{ds}^2\rvert+\frac{R_s+R_r\frac{L_m^2}{L_r^2}+\left(k_h\omega_s+k_e\omega_s^2\right)\frac{L_{lr}^2L_m^2}{L_r^2}}{\left(\frac{3n_pL_m^2}{4L_r}\right)^2\lvert i_{ds}^2\rvert}T_e^2\right)+k_m\omega_r^2$ where $T_e=\frac{3n_pL_m}{4L_r}\lambda_ri_{qs}$ and $i_{ds}=\frac{\lambda_r}{L_m}$ [54]	λ_r

The loss models in Table 1 vary according to the losses they consider. For example, core losses are modeled as insensitive to frequency, i.e., resistive loss, in the first three rows. Eddy current and hysteresis losses, both being core losses, are split in the fourth row where k_e and k_h are dependent on the material and construction of the machine. The effect of the frequency on core losses is clear in the fifth row where k_e is multiplied by ω_r^2 and k_h is multiplied by ω_r, which is similar to the model shown in the seventh row. Stray, friction, and windage losses are also

considered in the fifth row. A more generic loss model that relates losses to ω_{sl} is shown in the sixth row where the constants k_1–k_5 are parameter dependent. Such a model is convenient in visualizing P_{loss} as a function of a single control variable.

Convergence times of model-based LMTs range from 300 ms to several seconds, as shown in [4, 8, 35, 42, 46, 48], and efficiency improvements up to 70 points are recorded. Convergence times and efficiency improvements are dependent on the inertia and load on a machine shaft. In summary, common characteristics among model-based LMTs are their dependence on motor parameters and ratings and possible sub-optimal operation due to errors in parameter knowledge.

2.2.4 Physics-Based Techniques

Physics-based LMTs are independent of motor parameters or P_{loss} models. A physics-based LMT drives the control input to reduce P_{in}, which is available from voltage and current measurements. As explained in Section 2.2.1, minimizing P_{in} is equivalent to minimizing P_{loss} for a given P_o, subject to storage aspects.

Definition 2: A *physics-based* LMT utilizes electromechanical or mathematical principles to drive the control input in the direction of minimum P_{in}, regardless of the motor ratings or parameters.

Some physics-based LMTs perturb a control variable and then assess whether or not P_{in} decreased. Commercial energy-saving methods follow similar perturb-and-observe (P&O) techniques, also common in maximum power point tracking (MPPT) of photovoltaic (PV) arrays. Control variables similar to those utilized in model-based LMTs can be used. The perturbed command could be the V/f ratio [55] as in commercial drives, λ_m [56], the dc link

voltage of the inverter [57], and λ_{dr} in an FOC drive [58]. Among the three LMTs discussed in [59], one is physics-based and is similar to commercial voltage control. In general, P&O algorithms check whether changes in P_{in} and in x are positive or negative and update x accordingly. No machine parameter estimates or models are required, and all operation is based on the machine physics and response to change in the control variable. A high-level P&O algorithm is shown in Fig. 6.

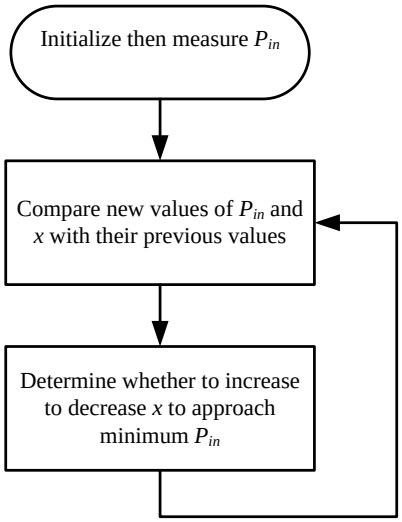

Fig. 6. Simplified flowchart of P&O

Several fuzzy logic controllers have been used as physics-based LMTs. Examples are shown in [60] where i_{ds} is used as the control variable. Membership functions are built based on derivative estimates $\Delta P_{in}/\Delta i_{ds}$ which determine the direction of i_{ds} towards minimum P_{in}. A neuro-fuzzy approach is also shown in [61] where the stator voltage is used as the control variable (further details about the training of the neural network and updating membership functions are available in [61]).

In general, convergence times of physics-based LMTs [55-60] are slower than model-based LMTs, and vary from a few seconds to several minutes for machine ratings between 1.5 and 10 hp. Their main advantage is independence of machine parameters or models.

2.2.5 Hybrid Techniques

Hybrid LMTs were first identified in [18, 19]. These LMTs have features from both model- and physics-based methods, thus the term "hybrid." Among several possible combinations of model- and physics-based characteristics, two main examples of hybrid techniques are: (i) applying P&O on a P_{loss} model, and (ii) using a parameter-dependent estimator with a physics-based LMT.

Definition 3: Hybrid LMTs require a motor or system model to search for the minimum P_{loss} or P_{in}, then use electromechanical principles and mathematical characteristics to achieve optimality.

Identifying hybrid techniques is not a straightforward process; each LMT is individually analyzed because hybrid LMTs can be easily confused with model- or physics-based LMTs. Also, the application context affects whether a method is hybrid or not. For example, if the control variable and cost function are measured independently of the drive model, RCC can be used as a physics-based method which relies on inherent ripple in measurements and drive physics to achieve the optimum. This is the case for RCC when used in loss minimization of dc machines where the control variable, in this case field current, and the input power can be measured. But, if parameter-dependent P_{loss} or P_{in} estimation is used as shown in [62], RCC still uses the drive physics to achieve optimal operation; the estimation of P_{loss} introduces model dependence and RCC becomes a hybrid LMT. A similar case is for RCC applications for induction machines where P_{in} is measured but λ_{dr} is estimated [53, 62]. In Chapter 3, RCC is

discussed in more detail, but is not the only hybrid LMT. Several techniques classified as model- or physics-based are actually hybrid, as in [7]. For example, [7] presents an LMT that estimates P_{in} from motor parameters then perturbs ω_{sl} to converge towards the minimum P_{in}. Other examples include [59] where the induction motor slip is evaluated from a model for minimum P_{in}, [63] where a search algorithm is also utilized with a dynamically-updated P_{loss} model, and [5] where fuzzy logic searches around a model-based minimum to correct the power factor.

2.2.6 Comparison of LMTs from Literature

A preliminary comparison of LMTs from the literature can be established. Even though the machines, drives, and loads vary from one reference to another, general characteristics can be drawn. Results are reported as reduction in P_{loss}, energy savings, efficiency improvement, stator voltage reduction, and others. Table 2 shows convergence times, machine ratings, and improvements introduced by different types of LMTs.

Table 2. Summary of LMT performance in literature ©2010 IEEE

Reference	Convergence time (s)	Improvement	Motor rating	Type
[4]	2.5	P_{loss} reduced by 70%	1/3 hp	Model-Based
[44]	5	Input voltage reduced from 220V to 85V	1 hp	Model-based
[46]	0.5	Efficiency improved by 50 points	1 hp	Model-based
[50]	Unspecified	Efficiency improved by 20 points	2.2 hp	Model-based
[51]	Unspecified	P_{loss} reduced by 75%	1.5 hp	Model-based
[35]	0.5 to 5	Efficiency improved by 12 points	1.5 hp	Model-based
[55]	5 min	Efficiency improved by 12 points	10 hp	Physics-based
[57]	Unspecified	Efficiency improved by 12 points	10 hp	Physics-based
[58]	7	Input Power reduced by 3.6%	7.5 hp	Physics-based
[60]	7	P_{loss} reduced by 50%	1.5 hp	Physics-based
[61]	0.5	Efficiency improved by 27 points	0.25 hp	Physics-based
[19]	0.5	P_{loss} reduced by 61%	1.5 hp	Hybrid

From the results and references shown Table 2, all LMTs lead to energy savings and efficiency improvement in one way or another. The amount of energy savings could be significantly affected by model dependence, and this is analyzed in more detail in Section 4.4.4 for a model-based LMT. Physics-based techniques are slower than model-based techniques due to the fact that most must wait to evaluate P_{in} in steady-state and update their control variable accordingly. An exception is shown in [61] where the machine power rating is very low and has less inertia compared to other machines, which allows the physics-based LMT to converge quickly. While P&O methods cause undesirable, persistent oscillations around the optimum, adaptive P&O algorithms, e.g. [64], can reduce the oscillation size exponentially. Therefore, physics-based techniques are mainly attractive because of machine parameter independence. Model-based LMTs converge quickly, depending on the time taken to calculate the control variable at the minimum P_{loss}. But, they are parameter dependent, might require tuning, and could cause sub-optimal operation due to parameter errors. Hybrid LMTs usually require fewer motor parameters than model-based LMTs and converge faster than physics-based LMTs. A potential drawback is implementation complexity. However, when using digital signal processors (DSPs), which are common in motor drives, this complexity is not limiting.

2.3 Ripple Correlation Control

2.3.1 Introduction and Background

Ripple correlation control is a real-time optimization method which was first patented in 1996 as a "self-excited power minimizer/maximizer for switching power converters and switching motor drive applications" [65]. It is clear from the patent title that motor drives are major RCC applications. RCC uses inherent ripple in power converters to achieve the optimum

of a time-dependent objective function $J(t)$. Whether $J(t)$ is concave (profit function) or convex (cost function), it should be unimodal, i.e., have a single optimality point. RCC maximization applications include PV MPPT and maximum power transfer from a source to a load through a power electronics converter. An obvious minimization application is RCC as an LMT [62, 66, 67]. In an induction machine, P_{in} is convex as shown in Fig. 4, but the curve is relatively flat near the minimum. The effect of this flatness on RCC and general LMT operation will be further discussed in Chapter 3. In the following discussion, cost function minimization is used to demonstrate the derivation of RCC control laws, which is a generalized scenario to minimize P_{in} or P_{loss} in an induction machine.

RCC shares common characteristics with two control methods available in the control systems literature: Extremum seeking (ES) control and vibrational control (VC). The discussion on RCC as ES is elaborated in Section 3.1. As defined in [68], VC is a *nonclassical control principle which proposes a utilization of zero-mean parametric excitation of a dynamical system for control purposes*. Thus, the characteristic common to both RCC and VC is the use of perturbations or excitations to enhance system operation. RCC uses inherent ripple in a system to achieve an optimum, but VC utilizes injected zero-mean sinusoidal vibrations to the plant parameters. For example, for a linear system $\dot{z} = \bar{A}z + \bar{B}uh\left(\frac{t}{\varepsilon}\right)$ where h is a periodic zero-mean function and ε is a small parameter, excitation is introduced to the input (u) through a multiplicative h, and the real plant can be modeled with perturbed parameters $\dot{z} = \left(\bar{A} + \tilde{A}\right)z + \bar{B}uh\left(\frac{t}{\varepsilon}\right)$ where perturbations are used to achieve stability [69]. Another example of VC is a nonlinear system $\dot{z} = g(z, u, \bar{d})$ where d is a plant parameter and excitations are

injected in $\bar{d}$ as $\bar{d} + \tilde{d}$. Several nonlinear system models are studied in [70] where VC is used to stabilize the system. In a stabilization problem using VC, the asymptotically stable solution ($\bar{z}_s$) is desired to reach the equilibrium point (z_{eq}) within a certain bound δ_{eq}: $\| \bar{z}_s - z_{eq} \| < \delta_{eq}$ [70]. One direct link that can be established between RCC and VC is that δ_{eq} can be minimized from an optimization perspective in both. As both RCC and VC utilize perturbations, the former to achieve an optimum and the latter to achieve stability, a stronger link should exist between both but needs deeper investigation that is beyond the scope of this dissertation.

2.3.2 RCC Basic Principles

Given the cost function $J(t)$ and the control variable $x(t)$, the optimal value of $J(t)$, $J^*(t)$ at $x^*(t)$, can be found by solving for $x^*(t)$ when $dJ(t)/dx(t) = 0$. This is illustrated in Fig. 7. For any initial condition $x_0 \in [x_{min}, x_{max}]$ set by the initial input u_0, the control input $u(t)$ is

$$u(t) = -k \frac{dJ(t)}{dx(t)}, \tag{3}$$

where k is a positive gain. To better understand equation (3), let $\dot{x}(t) = u(t)$ and thus the optimal $x(t)$, $x^*(t)$, can be found as $x^*(t) = -k \int_0^t \frac{dJ(\tau)}{dx(\tau)} d\tau$. Observing Fig. 7 at a certain instant t (thus t is dropped in the figure), when $x < x^*$, J decreases and $dJ/dx < 0$ which causes the integral to grow when scaled by $-k$ and therefore go toward the minimum. When $x > x^*$, J increases and $dJ/dx > 0$, the integral decreases when scaled by $-k$ and goes toward the minimum.

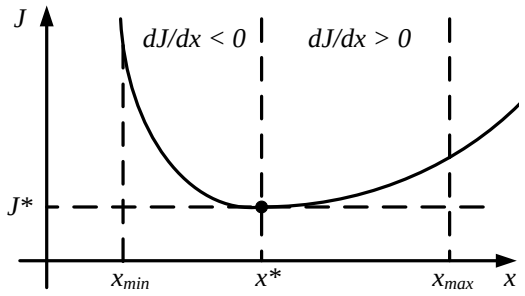

Fig. 7. Convex J with minimum J^* at x^*

In a dynamical system, $dJ(t)/dx(t)$ is not usually available for measurement ,thus using the chain rule, $x^*(t)$ can be written as

$$x^*(t) = -k\int_0^t \frac{dJ(\tau)}{d\tau}\frac{d\tau}{dx(\tau)}d\tau\,. \tag{4}$$

Since the sign of $d\tau/dx(\tau)$ and $d\tau/dx(\tau)$ is the same, replacing $d\tau/dx(\tau)$ by a function $q(\tau)$ that preserves the sign of $dx(\tau)/d\tau$ would still achieve the minimum. For the simplest form of $q(t) = dx(t)/dt$, equation (4) can be written as

$$x(t) = k'\int_0^t \frac{dJ(\tau)}{d\tau}\frac{dx(\tau)}{d\tau}d\tau = k'\int_0^t \dot{J}(\tau)\dot{x}(\tau)d\tau\,, \tag{5}$$

where k' is a constant gain. Note that equations (4) and (5) still preserve the minimum because for the simplest form of $q(t) = dx(t)/dt$, applying the chain rule again gives

$$x^*(t) = -k'\int_0^t \frac{dJ(\tau)}{dx(\tau)}\frac{dx(\tau)}{d\tau}\frac{dx(\tau)}{d\tau}d\tau = -k'\int_0^t \frac{dJ(\tau)}{dx(\tau)}\left(\frac{dx(\tau)}{d\tau}\right)^2 d\tau\,. \tag{6}$$

In equation (6), the original integrand from equation (3) is scaled by a positive term, and the minimum point $x^*(t)$ is preserved [71], given that $x(t)$ is persistently excited.

When ripple exists in $J(t)$ and $x(t)$, this ripple includes information about $dJ(t)/dt$ and $dx(t)/dt$. In general, ripple can be modeled as a Fourier series of sinusoidal signals where dc and higher frequencies are present. If $J(t)$ and $x(t)$ are high-pass filtered to eliminate dc components,

ripple can be used to extract derivative information of $J(t)$ and $x(t)$. For the ripple signals $\tilde{x}(t)$ and $\tilde{J}(t)$, RCC law can be written as

$$x^*(t) = -k'' \int_0^t \tilde{J}(\tau)\tilde{x}(\tau)d\tau \,, \tag{7}$$

where k'' is a constant gain.

Without loss of generality, let the ripple signals be sinusoidal and high-pass filtered. From Fig. 7, when the operating point is at the left of $x^*(t)$ and $dJ(t)/dx(t)$ is negative, the ripple signals $\tilde{x}(t)$ and $\tilde{J}(t)$ are out-of-phase by $\pi+2n\pi$ radians where n is an integer number and $\tilde{J}(t)\tilde{x}(t) \le 0$ for all t. When the operating point is at the right of $x^*(t)$ and $dJ(t)/dx(t)$ is negative, the ripple signals $\tilde{x}(t)$ and $\tilde{J}(t)$ are in-phase at $0 + 2n\pi$ radians and $\tilde{J}(t)\tilde{x}(t) \ge 0$ for all t. These phase relationships are illustrated in Figs. 8 and 9. At the optimum, the ripple signals are $\pi/2+n\,\pi$ radians out-of-phase.

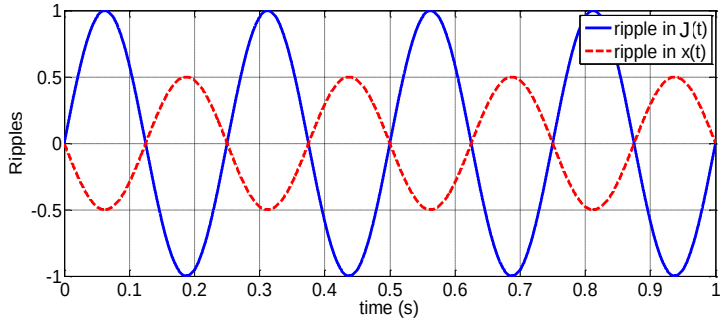

Fig. 8. Ripples in the objective function and control variable when $\tilde{J}(t)\tilde{x}(t) \le 0$

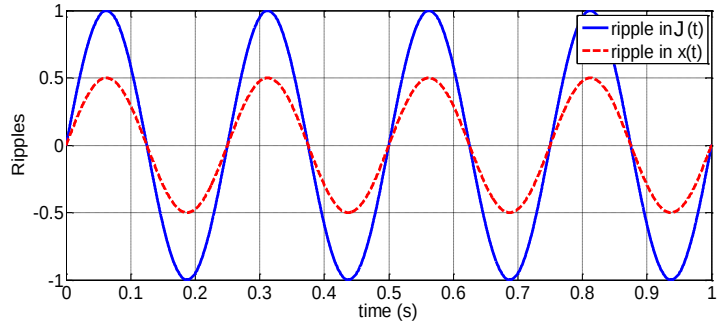

Fig. 9. Ripples in the objective function and control variable when $\tilde{J}(t)\tilde{x}(t) \ge 0$

A discrete version of RCC (DRCC) was presented in [72] for MPPT applications with dc-dc converters. The discrete x can be updated as

$$x^*(T) = x^*(0) + \frac{k_d w_+}{1-d}[J(d\,T) - J(0)], \tag{8}$$

where k_d is a constant gain, d is the duty cycle of the converter, T is the ripple period in J, and w_+ is the positive slope of the triangular ripple in x. As shown in equation (8), extracting two samples of J over T is sufficient to drive the system to the optimum [72]. A digital implementation of equation (7) was also presented in [73].

Applying RCC as an LMT for machines has been investigated in [53, 62, 66]. Dc, synchronous, and induction machines were used, and all research concluded that for induction machines, low frequency ripple should be used. Such ripple is not inherently present in an induction machine drive, so external perturbations were injected. In Chapter 3, useful frequencies are identified from a frequency domain analysis. Experimental results of RCC in induction machine applications have not yet been presented for reasons outlined in Chapter 3. Chapter 3 also elaborates on the reason behind the low ripple frequency requirement in induction machines from an energy storage perspective.

2.4 Reliability Modeling of Induction Motor Drives

Adding an LMT to the induction motor drive dynamically changes an input command. This change could affect the drive response under faults. For example, if any fault causes T_e to overshoot in an FOC drive while the drive is operating under flux weakening, the machine could stall because the flux is not able to support T_e. Reliability assessment of the drive under LMTs is therefore essential. In general, reliability modeling or assessment is valuable for any motor drive

application. Safety and reliability are major concerns, especially in transportation systems such as EVs [1, 2]. Drive failure in transportation, manufacturing, pumping, cooling, etc., could be catastrophic.

Common reliability models include fault trees developed by Bell Telephone Laboratories [74], series-parallel reliability block diagrams (RBDs), state diagrams and Markov models, etc. Failure mode and effect analysis (FMEA) is also a popular tool to evaluate system reliability. FMEA assesses the system response after every fault by comparing it to desired performance measures. In dynamic systems, Markov models are the most attractive because they capture the transition dynamics of a system from one state to another, with dependency only on the previous state. This simplifies studying the fault occurrence order, fault and repair effects, state-dependent failure rates, and fault coverage — the probability of system survival for a fault. One drawback of Markov models is that they assume fixed failure rates that do not consider the increased failure rate with component aging. Markov models can be expanded easily for complex and large systems. The detail can be at a component level, e.g., gate driver of one IGBT in an inverter; a sub-system level, e.g., short circuit in an inverter phase; or a system level, e.g., motor drive shut down. The analysis complexity significantly increases for more detailed models of large systems, and sub-system level analysis is usually used. The level of detail in any reliability analysis sets the analysis complexity, where more fault modes would cause exponential growth of the system states.

Significant work has been published on fault tolerance, e.g. [75], speed-sensorless control (for higher reliability), e.g. [76], and fault models and modes in motor drives [77], but comprehensive reliability modeling methods have not been discussed. Such methods are key to

assessing whether or not a design meets reliability and fault tolerance requirements for all possible operational conditions. Some examples are summarized in Table 3.

Table 3. Faults studied in literature

Reference	Faulty components or subsystems
[78]	Power electronics
[79]	Control
[80, 81]	Power supply
[82]	Motor
[83]	Sensors
[84]	Cooling
[85]	Motor and power supply
[86]	Control, power electronics, and motor
[87]	Transformer and line filters

To improve system reliability, redundancy in most of the components mentioned in Table 3 is common. Among the most common designs for redundancy are multiphase machines [88] and split-wound motors [89]. Reliability enhancement through control is achieved with fault-tolerant control algorithms [78, 90-92]. Other strategies for reliability enhancement include more reliable communication [93], preventive maintenance [94, 95], and component de-rating.

Fault detection is essential for appropriate drive operation and could be utilized to activate safe modes, emergency systems, or fault-isolation mechanisms. Several methods for fault detection are available [78, 96-103] and utilize frequency-domain analysis, e.g., a short-time Fourier transform [96], pattern recognition [101], or monitoring the drive operation such as current, voltage, temperature, etc.

Markov models are rarely found in the context of motor drive reliability. Models in [84, 104-106] are incomplete and do not include systematic procedures, e.g., performance evaluation, multi-fault levels, mathematical foundations, etc., to develop a reliability model of the drive. A high-level analysis of a power system that includes a machine is shown in [106] and the whole

drive is just a sub-system. Essential faults in machines and sensors are ignored in [104], and sensor faults in [105] even though they could cause catastrophic drive failures. Although most faults, including those in sensors, are addressed in [83], the focus is on control. No modeling procedure is presented. Fault coverage is missing in all motor drive "reliability literature." Also, in [83] only inverters as a series RBD are considered; no systematic procedure is considered in [107].

Even when the drive fails, it is desired to maintain the load. Safe-mode control that maintains such operation is uncommon in the literature. Such a safe mode controller is expected to have minimum dependence on feedback to avoid sensor faults, as shown in Fig. 10. The closest approach to switching to a safe mode is [108] where an induction motor drive switches between IFOC and DTC to improve transient and steady-state operation. Limitations of safe-mode control include the effects of faults common in both nominal and safe-mode controllers, e.g., loss of the controller power supply.

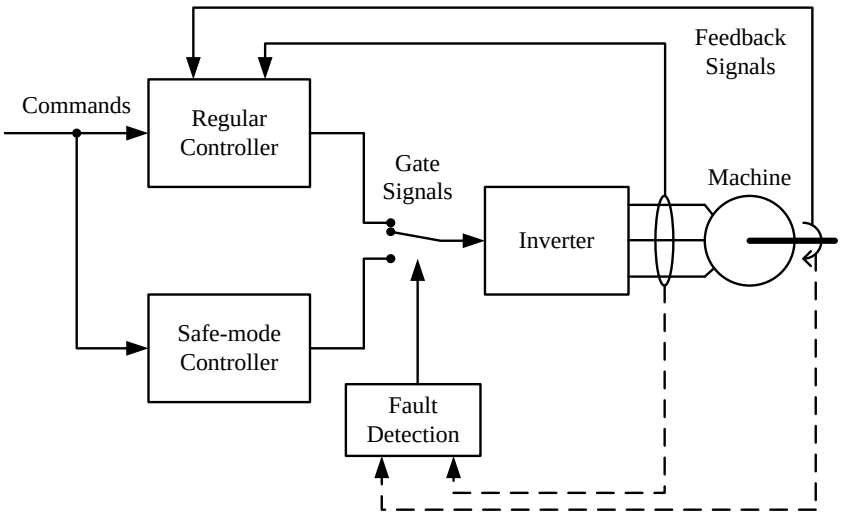

Fig. 10. Desired safe-mode scheme

Therefore, most available literature covers general physical faults, assumes certain system structures, e.g., series components, stresses fault-tolerant algorithms but not necessarily redundancy, and limits the reliability evaluation to specific components. Even though energy-saving methods or LMTs are seen as essential in current and future drive applications, their effect on system reliability is ignored. Also, having a back-up controller could be an attractive solution to several failures, but this has not been addressed.

2.5 Power Electronics Loss Estimation: Loss Minimization and Reliability Enhancement

In order to minimize the total losses in a drive system, power electronics losses should be addressed. An essential step in minimizing power electronics losses is loss estimation. Also, proper loss estimation in power electronics leads to better thermal designs including component sizing, placement, cooling and thermal management. Most common failures in motor drives are caused by power electronics faults, specifically related to problems with thermal management or conservative thermal designs. IGBT-diode pairs are among the most common devices in motor drives, and their market is continuously expanding due to their fast response, well-established gate drivers, and increasing allowable junction temperatures, e.g., SiC IGBTs. Thus, loss estimation in IGBT-diode pairs helps reduce power electronics faults and improve overall drive reliability.

Usually, power losses and thermal characteristics of the power electronics and thermal management components are directly related. Zero- or higher-order circuit-based thermal models are utilized to predict power electronics junction temperatures. Compared to an electric circuit, thermal circuits use dissipated power instead of current, thermal resistance instead of electric resistance, and temperatures instead of voltages as shown in the zero-order model in Fig. 11.

Designing thermal management is usually an iterative process. The first step is to determine the IGBT-diode pairs (or any power semiconductor devices) with suitable ratings for the application. From the device datasheet, the junction to case thermal resistance ($R_{j\text{-}c}$) and case to sink thermal resistance ($R_{c\text{-}s}$) are determined. The second and most fundamental step is to estimate power losses. While these are mainly dependent on electrical operation, e.g., switching and conduction, and electrical components, e.g., gate resistor, they may be affected by the junction temperature as will be explained later. After a preliminary power loss estimate is found, the third step is to use a preliminary thermal design with some sink-to-ambient thermal resistance ($R_{s\text{-}a}$). The temperatures at the junction (T_j), case (T_c), and sink (T_s) can be found for a certain ambient temperature (T_a). Alternatively, the design can start from a desired maximum T_j. In Fig. 11, P_Q, P_D, and P_T are the IGBT, diode, and total power losses, respectively; subscripts D and Q are for diode and IGBT quantities, respectively.

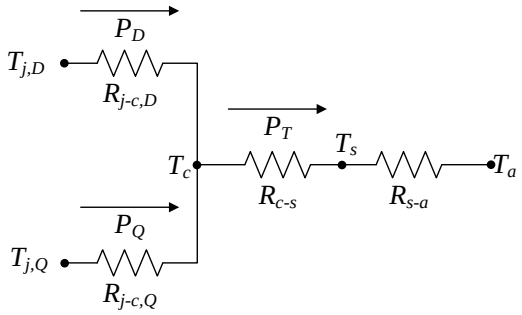

Fig. 11. Zero-order thermal model

The design then proceeds iteratively where other devices with different power losses or thermal resistances can be selected. Different heat sinks and cooling strategies with different equivalent $R_{s\text{-}a}$ can also be selected. The design and analysis could also proceed the other way around—if temperature measurements are available for a specific design, power losses can be estimated based on datasheet thermal resistance values [109-115]. Several design considerations

are presented in [116]. In these scenarios, power loss estimation can be used in active thermal control as in [117].

Assumptions of certain electrical characteristics in the power electronics converter or inverter could lead to estimation errors and sub-optimal thermal designs. Most published research in power loss estimation thus assumes a fixed switching frequency (f_{sw}) [110, 111, 114-116, 118-122]. Such an assumption is not applicable for estimating power losses under aperiodic switching, e.g., hysteresis. Also, power losses are significantly affected by the switching pattern in the semiconductor devices because these patterns affect the switching losses and conduction losses (through conduction time). Periodic switching, mainly pulse-width modulation (PWM), is the most common switching scheme in power electronics. In addition to fixed switching frequencies, such tools make major assumptions as an ideal ripple-free collector-emitter current (I_{ce}) [118, 119], linear energy functions with respect to current [120], datasheet energy values that approximate power losses at a certain I_{ce} [122], etc. In an inverter under fixed-f_{sw} operation, loss estimation uses variants of (9) – (12) [118] where the subscripts *cond*, *sw*, *on*, and *off* stand for conduction, switching, turn-on, and turn-off losses, respectively; I_{cep} is the peak collector current, m_a is the modulation depth, cosφ is the power factor, f_{sw} is the switching frequency, I_{rr} and t_{rr} are the diode reverse recovery current and time, respectively, V_{dc} is the inverter dc bus voltage, $V_{ce,sat}$ is the collector-emitter saturation voltage, and V_f is the diode forward voltage.

$$P_{Q,cond} = I_{cep} V_{ce,sat} \left(\frac{1}{8} + \frac{m_a}{3\pi} \cos\varphi \right) \tag{9}$$

$$P_{D,cond} = I_{cep} V_f \left(\frac{1}{8} - \frac{m_a}{3\pi} \cos\varphi \right) \tag{10}$$

$$P_{Q,sw} = \left(E_{Q,on} + E_{Q,off} \right) f_{sw} \frac{1}{\pi} \tag{11}$$

$$P_{D,sw} = \left(I_{rr} V_{dc} t_{rr} f_{sw} \right) \frac{1}{8} \tag{12}$$

Curve fitting of switching energies is a common practice in the literature. Points taken from datasheet energy-vs.-current curves are processed using curve-fitting methods as polynomial or logarithmic functions of the current, e.g. [115]. Curves given in datasheets are usually plotted under specific test conditions, mainly V_{dc}, $T_{j,Q}$ and/or $T_{j,D}$. The effects of the gate resistance (R_g) and gate voltage (V_g) of an IGBT are commonly considered as the choice of the gate drive, and soft or hard switching could also affect the energy curves. Even though energies can be accurately estimated by considering most discrepancies between the actual application and the datasheet test conditions, effects of different factors differ from one IGBT-diode module to another. Thus, although specific detailed models would be accurate for one module, the model has to be adjusted for all other modules.

The simplest form considered is shown in (13) where the effect of V_{dc} is assumed to be linear with the base dc voltage (V_{base}) used in the tests. In equation (13), E_{sw} can be the IGBT turn-on, turn-off, or diode turn-off energy, and E_{sw}^{ds} is the switching energy given in the datasheet.

$$E_{sw} = E_{sw}^{ds} \left(\frac{V_{dc}}{V_{base}} \right) . \tag{13}$$

Equation (13) might not accurately estimate the switching energies for specific operating conditions, but it is commonly used in commercial software, e.g., Melcosim from Mitsubishi. It can be applied to any IGBT-diode module without the need to tune any gains or factors as there are no unknowns. Another way to model the effects of the current (I), V_{dc}, and T_j is presented in

[123] and shown in equation (14) where υ, σ, μ, and κ are constants chosen for the best curve fit and T_{base} is the device junction temperature under the datasheet test.

$$E_{sw} = \upsilon I^{\sigma} \left(\frac{V_{dc}}{V_{base}} \right)^{\kappa} \left(\frac{T_j}{T_{base}} \right)^{\mu} . \tag{14}$$

More effects are considered in [124] where R_g and V_g are also considered, as shown in equation (15), where R_{base} and $V_{g,base}$ are the datasheet test gate resistor and voltage, respectively; ζ and ς are constants chosen in a similar manner as μ and κ.

$$E_{sw} = \upsilon I^{\sigma} \left(\frac{V_{dc}}{V_{base}} \right)^{\kappa} \left(\frac{T_j}{T_{base}} \right)^{\mu} \left(\frac{R_g}{R_{base}} \right)^{\varsigma} \left(\frac{V_g}{V_{g,base}} \right)^{\zeta} . \tag{15}$$

A combination of temperature measurements and curve fitting is shown in [124] to determine curve-fitting coefficients.

Model-based estimation methods rely on the IGBT-diode parasitic model where all parasitic capacitance and resistance is estimated, e.g. [125]. Such methods tend to be computationally expensive, especially with detailed models. When ideal switch models are used, most of the power loss information is lost and inaccuracies occur. For example, the method presented in [126] uses ideal switch models but suffers from measurement offsets which are corrected manually.

Loss estimation under aperiodic switching is presented in some examples, but without calorimetry. A model-based method is shown in [127] where both electrical and thermal characteristics are modeled. The method in [127] is model-dependent. Two methods that use information about the switching and conduction of the IGBT and diode are presented in [128, 129]. Both use simple curve fitting and the detection of switching and conduction states. In [129], only simulations under PWM switching are provided and therefore the experimental

accuracy of the method is not validated for periodic and aperiodic switching. The method in [128] is also used under fixed f_{sw} and the estimation error is acceptable and less than 15%. Reference [130] uses curve fitting of switching energies to improve the computational efficiency as compared to model-based methods. Loss measurement is not elaborated upon even though estimated and measured losses are compared. The tool in [130] requires significant signal conditioning to obtain meaningful results, has a small step size and a long simulation time, depends on rise and fall times, and lacks incomplete comparisons with available software common in the industry.

In summary, literature lacks loss-estimation techniques that are model-independent, fast, accurate, require no or minor signal-conditioning, operate on any switching scheme, and are experimentally validated to have all of these advantages. The tool proposed in Chapter 6 has all of these characteristics and is able to estimate losses under periodic and aperiodic switching with three measurements: load current, IGBT switching pulse, and V_{dc}.

CHAPTER 3

RIPPLE CORRELATION CONTROL AS AN EXTREMUM-SEEKING CONTROL AND A LOSS-MINIMIZATION TECHNIQUE

3.1 Ripple Correlation Control as an Extremum Seeking Control

Extremum seeking control has been researched since the early 20th century [131], and significantly developed in the 1950s and 1960s, e.g. [132, 133]. One of the frequently used ideas behind ES is the injection of sinusoidal perturbations into a dynamical system to achieve an extremum operating point. Several applications of ES have been introduced in the literature including current maximization in a railway application [131], MPPT of a photovoltaic (PV) array [134], MPPT of a wind energy conversion system [135], optimization of automotive power trains [136], antilock braking systems [137], and axial flow compressors [138]. When ES is applied to renewable energy systems, mainly PV and wind, in addition to automotive applications, a significant overlap with other real-time optimization (RTO) techniques is found. Although these techniques dynamically optimize a cost or profit function, they have not been directly associated with ES.

Ripple correlation control is an RTO technique that utilizes inherent ripple in a dynamic system to achieve the optimum [65, 139]. Because RCC can be a fast (with high ripple frequencies) and accurate (due to integral control) LMT, and has been shown to have problems operating at high frequencies in induction machines, there is more interest in detailed analyses of RCC as an LMT [53, 62, 66]. It is useful to relate RCC to available ES theory to analyze its stability and establish a link between the RCC and ES literature that could be helpful to address RCC problems. The main common characteristic is the use of perturbations to estimate the function gradient and achieve optimality. The major difference is the perturbation source. In the

following analysis and discussion, *optimum* and *extremum* are used interchangeably, and the objective function is assumed to be unimodal where the local extremum is global.

3.1.1 Historic Overview of ES

Most researchers involved with ES agree that the work by Leblanc in 1922 [131] is the first attempt to utilize perturbations in extremum seeking. In [131], the current in an electric railway feeder is maximized using varying self-inductance of a coil at 20 kHz perturbations. Extensive ES research followed in the 1950s, mainly in the Russian literature, which is summarized along with some American literature [140] on ES in [141]. ES techniques in [132, 141-143] are distinguished from the rest by the use of stepping regulators, which use discrete steps towards the extremum. The classification in [140] is summarized in [141] and is restated here: The first group includes controllers that use a static characteristic slope, found using direct differentiation, continuous test signals, or output sampling. The second group includes peak-holding regulators that use the error between the extremum and the actual operating point to maintain extremum seeking. Discussions in [132] focus on the perturbation- or oscillation-based ES where systems are classified by having external or self-oscillations. A third category addressed in [132] includes non-perturbation-based ES where systems have preset nonlinear follow-up characteristics.

Morosanov [141] developed a more comprehensive overview that classifies ES algorithms based on the search method. A block diagram that summarizes a basic ES system is presented in [141] and shown in Fig. 12. It will be shown later that this diagram is not only the basis of all ES, but also RCC. Note that again, $x(t)$ is the control variable and $J(t)$ is the output and objective function. It is important to mention that the ES system shown in Fig. 12 is

considered simplified. While a "plant" usually holds the dynamics from the input $Z(t)$ [or $u(t)$], to the output $J(t)$ [or $y(t)$], ES literature shows a simple mapping between $x(t)$ and $J(t)$, in addition to the effector (E) which is usually an integrator as will be discussed later. In most real systems, the mapping is not as simple as shown in Fig. 12, and might be a complex problem especially if it is an inverse model of a complex system.

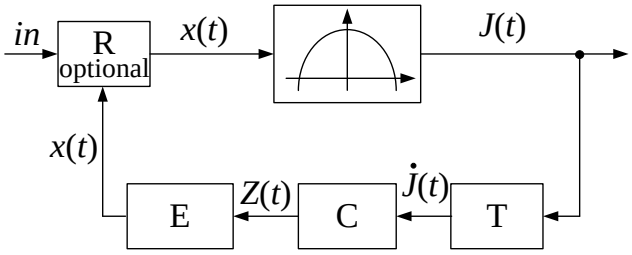

Fig. 12. Basic ES system [141]

$\dot{J}(t)$ could be generated using different methods with the extremum transducer "T." The sign and value of the derivative include information about the error between the operating point and the extremum, and whether it is converging towards the extremum or not. This information is accompanied with the change of the control variable $x(t)$ to determine the next value of $x(t)$. According to [140, 141], there are three main methods to estimate $\dot{J}(t)$:

1. Direct differentiation.
2. Accessary test sinusoidal modulation with phase detection.
3. Approximate differentiation (first-order discrete derivatives).

While direct differentiation might be a simple approach with either analog or digital circuits, small transitions in y could be significantly amplified in $\dot{J}(t)$. Also, approximate differentiation introduces truncation errors. External perturbations are the main basis of modern ES [144], and more details follow in the next section.

The controller "C" uses information from $\dot{J}(t)$ and $\dot{x}(t)$ (not shown) to determine the search direction towards the optimum. Four main situations exist in a convex (concave) cost (profit) function where $\dot{J}(t)$ and $\dot{x}(t)$ could be $\leq$ or ≥ 0, independently. The signs of derivatives are used to find the desired search direction, as shown in (16) [141], where χ is a constant gain that is > 0 for maximization and < 0 for minimization,

$$Z(t) = \chi \frac{\text{sign}(\dot{J}(t))}{\text{sign}(\dot{x}(t))}, \tag{16}$$

and $\text{sign}(x) = \begin{cases} +1, \text{ if } x > 0 \\ 0, \text{ if } x = 0 \\ -1, \text{ if } x < 0 \end{cases}$.

The effector "E" is usually an integrator that accumulates the desired change in the control variable $x(t)$. For example, in a maximization case, if $\dot{J}(t) > 0$ and $\dot{x}(t) > 0$, the operating point is on the left side of the profit function, $Z(t) > 0$, and the integrator will further increment $x(t)$. Once the operating point passes the maximum, $\dot{J}(t) < 0$ and $\dot{x}(t) > 0$, and $Z(t) < 0$, so the integrator will decrement $x(t)$ back towards the maximum. This integration is shown in (17) where t_o is the initial time:

$$x(t) = \int_{t_o}^{t} Z(t) = \chi \int_{t_o}^{t} \frac{\text{sign}(\dot{J}(\tau))}{\text{sign}(\dot{x}(\tau))} d\tau . \tag{17}$$

The regulator "R" is optional. It regulates the input to the plant and passes $x(t)$ to that input. Note that in (17), the controller will diverge when $\text{sign}(\dot{x}(t)) = 0$, and therefore the integrand can be changed to

$$x(t) = \chi \int_{t_o}^{t} \text{sign}(\dot{J}(\tau))\text{sign}(\dot{x}(\tau)) d\tau , \tag{18}$$

where $\text{sign}(\dot{x}(t))=0$ is no longer a problem, or simply,

$$x(t) = \chi \int_{t_o}^{t} \text{sign}(\dot{J}(\tau)\dot{x}(\tau))d\tau \tag{19}$$

as shown in [145].

Another major review of ES from 1980 is available in [146] where both static and dynamic systems are overviewed, and ES is categorized into four groups:

1. Perturbation methods: aim at setting $\dot{J}(t) = 0$. These methods use test (external) perturbations.
2. Switching methods: change the input in steps until reaching the extremum area. These methods are similar to perturb and observe (P&O) algorithms that decide on the next step in $x(t)$ based on the change in $x(t)$ and the approximate differentiation or difference in $J(t)$. An example of MPPT is given for a satellite solar cell.
3. Self-driving systems: rely on information from the derivatives of $J(t)$ and $x(t)$ to find the extremum. Even though no details are given on the method of finding $\dot{J}(t)$, it is mentioned that a filter should be used to extract the derivatives. These systems are very similar to RCC, especially when the control law proposed is modified to be

$$z(t) = \text{sign}(\dot{x}(t)) = \text{sign}(\hat{\dot{J}}(t)\hat{\dot{x}}(t)) \tag{20}$$

   where $\hat{\dot{J}}(t)$ and $\hat{\dot{x}}(t)$ represent the filtered signals. Integrating (20) yields the desired input. Note that division is avoided in (20).
4. Model-oriented methods: use model information for finding the extremum. The model could either be updated before or in parallel with the ES.

While ES in MPPT applications can be categorized into these four categories, RCC needs careful consideration due to its similarity with two or more of the above categories.

3.1.2 Modern Extremum-Seeking Control

External perturbations are the basis of modern ES in the works of Krstić, e.g. [144], Nesić, e.g. [147], and others such as [148]. Reference [149] is dedicated to introducing ES for RTO applications. ES is used to find an unknown extremum of a dynamic system in both continuous and discrete times, and ES stability is analyzed. Half of [149] is dedicated to applications including bioreactors, formation flight, combustion in stabilities, etc. Several papers by Krstić outline the theory of ES with external sinusoidal perturbations.

Extremum seeking of a continuous-time system with external perturbations is shown in Fig. 13. The main idea in this system is to inject an external perturbation, $x_p(t) = \alpha_p \sin(\omega t)$, to the system input where ω is the perturbation frequency and α_p is the perturbation amplitude. The perturbation is used to estimate the gradient of J (J_p), as the perturbation effect will propagate to J.

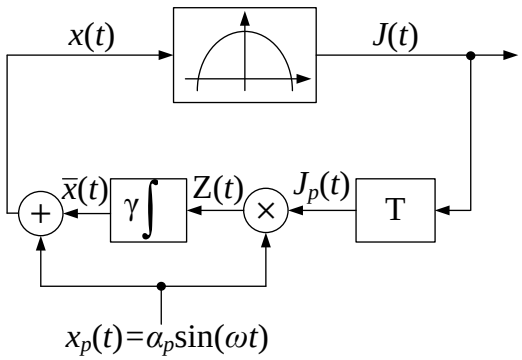

Fig. 13. Modern ES based on external perturbations

Thus, J would have a certain offset with some perturbation due to the additive perturbation at the input. "T" is usually a high-pass filter that attenuates the offset in $J_p(t)$, however, the perturbation and higher order harmonics remain. As in equation (19), the derivative x is multiplied or "correlated" with that of J, but when this is put in the perspective of Fig. 13, $x_p(t)$ and $J_p(t)$ are correlated as $\xi = x_p(t)\, J_p(t)$, where $x_p(t)$ demodulates $J_p(t)$. Because the perturbations and derivatives are sinusoids, they maintain their relative phase shift. The effect of higher order harmonics produced by demodulation is negligible after integration. In Fig. 13, the input has an offset $\bar{x}(t)$ and the additive perturbation $x_p(t)$. Integration increases or decreases the control signal in the direction of the extremum, and the gain γ affects the convergence rate and scaling of ξ. Perturbation or persistent excitation is always added to the input to maintain tracking. Otherwise, $x_p(t)= 0$, and the system will not be able to dynamically track the extremum because the integrator will not update from its last value.

A simple mathematical derivation of the ES of Fig. 13 is shown in [149] and here for convenience. The main assumption is that $J(t) = J^*(t) + \frac{1}{2}\frac{d^2J(t)}{dx(t)^2}\left(x(t) - x^*(t)\right)^2$, which is a reasonable assumption around the extremum. Note that $\frac{d^2J(t)}{dx(t)^2} > 0$ for minimization, and $\frac{d^2J(t)}{dx(t)^2} < 0$ for maximization problems. The following derivation shows that the system will converge by having the error $x_e(t) \rightarrow 0$ or $\bar{x}(t) \rightarrow x^*(t)$.

$$x_e(t) = x^*(t) - \bar{x}(t)$$

$$x(t) = \bar{x}(t) + \alpha_p \sin(\omega t)$$

$$\Rightarrow x(t) - x^*(t) = \alpha_p \sin(\omega t) - x_e(t)$$

Substituting $x(t)$-$x^*(t)$ in $J(t)$,

$$J(t) = J^*(t) + \frac{1}{2}\frac{d^2J(t)}{dx(t)^2}\left(x_e(t) - \alpha_p \sin(\omega t)\right)^2.$$

Expanding $J(t)$ and passing it though the high-pass filter (T),

$$J_p(t) \approx \frac{1}{2}\frac{d^2J(t)}{dx(t)^2}x_e(t)^2 - \alpha_p \frac{d^2J(t)}{dx(t)^2}x_e(t)\sin(\omega t) + \frac{\alpha_p^2}{4}\frac{d^2J(t)}{dx(t)^2}\cos(2\omega t),$$

$$\xi(t) \approx \frac{\alpha_p}{2}\frac{d^2J(t)}{dx(t)^2}x_e(t)^2\sin(\omega t) - \alpha_p^2\frac{d^2J(t)}{dx(t)^2}x_e(t)\sin^2(\omega t) + \frac{\alpha_p^3}{4}\frac{d^2J(t)}{dx(t)^2}\cos(2\omega t)\sin(\omega t).$$

For a constant $x^*(t) = x^*$, $\dot{x}_e(t) = -\dot{\bar{x}}(t)$ since $\dot{x}^*(t) = 0$. Using trigonometric identities and integrating,

$$x_e(t) = -\bar{x}(t) \approx \frac{\gamma}{s}\left(\begin{array}{l} -\frac{\alpha_p^2}{2}\frac{d^2J(t)}{dx(t)^2}x_e(t)^2 + \frac{\alpha_p^2}{2}\frac{d^2J(t)}{dx(t)^2}x_e(t)\cos(2\omega t) \\ +\frac{\alpha_p^3}{8}\frac{d^2J(t)}{dx(t)^2}\left(\sin(\omega t) - \sin(3\omega t)\right) + \frac{\alpha_p}{2}\frac{d^2J(t)}{dx(t)^2}x_e(t)^2\sin(\omega t) \end{array}\right).$$

As the integration of sinusoids has negligible effects on $\bar{x}(t)$, and $x_e(t)^2$ is negligible,

$$x_e(t) \approx -\frac{\gamma}{s}\left(\frac{\alpha_p^2}{2}\frac{d^2J(t)}{dx(t)^2}x_e(t)\right).$$

Then, $\dot{x}_e(t) \approx -\frac{\gamma\alpha_p^2}{2}\frac{d^2J(t)}{dx(t)^2}x_e(t)$.

For $x_e(t) \to 0$, $\gamma\alpha_p^2\frac{d^2J(t)}{dx(t)^2}$ must be > 0. In a maximum-seeking problem, $\frac{d^2J(t)}{dx(t)^2} < 0$ and γ is chosen to be < 0, while in a minimum-seeking problem, $\frac{d^2J(t)}{dx(t)^2} > 0$ and γ is chosen to be > 0.

Therefore with the appropriate choice of γ, $x_e(t) \to 0$ and $\bar{x}(t) \to x^*(t)$. System stability proofs using both the static and singular perturbation system models are extensively studied in [144].

A discrete version of this system is shown in [150], where the plant is split into three blocks: two input and output blocks that are assumed to be exponentially stable linear functions. Between them are the plant dynamics lumped in a nonlinear function. Stability of the discrete-time system is studied using two-time-scale averaging theory. Only continuous-time ES and RCC are addressed here. Discrete-time versions of both controllers exist, and the analysis presented here can be applied. Other discrete ES algorithms include least-square estimation, parabola approximation, and ellipse approximation as shown in [135] where the objective function is assumed to be quadratic around the optimum.

An important design factor in ES is the frequency ω which affects stability and convergence [151]. The choice of ω in a static system does not affect convergence, and can be arbitrarily large. But for dynamic systems, an upper bound on ω is chosen. In [151], stability conditions include "small-enough" α_p and ω. The physical interpretation of this choice is not clear, but larger ω lead to faster convergence times as shown in simulation in [151]. The ES convergence rate is shown to be dependent on four factors: gain γ, frequency ω, amplitude α_p, and power of the perturbation signal power P_p. A function β is defined as $\beta=\gamma\alpha^2\omega P_p$, where β sets the upper bound convergence rate. Note that in [151], square and triangular perturbations are also studied and show that square perturbations result in the fastest convergence rate. This result implies that *sign* functions of J and x or their derivatives, where the *sign* function results in a square wave, would lead to faster convergence of the ES.

3.1.3 RCC from an ES Perspective

Both RCC and ES have been well established as real-time optimization methods, with two major similarities. The first is that both utilize perturbations to achieve optimality, and the

second is that they both assume objective functions with a single global extremum. The latter might pose a limitation on real-time optimization methods, especially if the objective function could have local extrema, e.g., PV power curve under partial shading. Some other real-time optimization methods address the global extremum seeking or optimization in the presence of local extrama. Examples include the work presented in [152] where a two-stage method is used with the first stage being a brute-force search; modified search methods such as the one shown in [153]; variable perturbation or dither where the search space of the ES method is extended and shrunk based on the variable step size set by the frequency of the dither, e.g., [151]; and others. Other than having a brute-force search or a brute-force-assisted search, there is no method that can guarantee accurate convergence to a global extremum in the presence of local extrema. This problem remains as an open and active research topic. Thus, objective functions with a single extremum are assumed in the following analysis.

There are several formulations of equation (5) that can be directly related to ES shown in equation (19). Even when equation (7) is used rather than equation (5), equations (7) and (19) give similar results. Since ripple sign at any instant is what determines the gradient d$J(t)$/d$x(t)$ sign, (7) can be written as (10) where σ_k is a positive gain,

$$x^*(t) = \sigma_k \int_0^t \text{sign}(\tilde{J}(\tau)\tilde{x}(\tau))d\tau \,. \tag{21}$$

But, sign(a)sign(b)=sign(ab). Therefore, (21) can be written as

$$x^*(t) = \sigma_k \int_0^t \text{sign}(\tilde{J}(\tau))\text{sign}(\tilde{x}(\tau))d\tau \,. \tag{22}$$

A basic principle in RCC is that ripples are used to estimate the derivatives of x and J. For the simple case of x and J having a dc offset with sinusoidal ripple, the derivatives and the

ripple are both sinusoidal and maintain their relative phase relationship. Triangular and exponential ripple waveforms are also common in power electronics converters. Exponential ripple and its derivative are both exponential and, again, the ripple and derivative have similar characteristics. Triangular ripple can be written as a Fourier series of sinusoids, and thus the derivative and ripple hold similar information except that the derivative is a square wave. This is not straightforward; therefore, two examples are shown in Fig. 14.

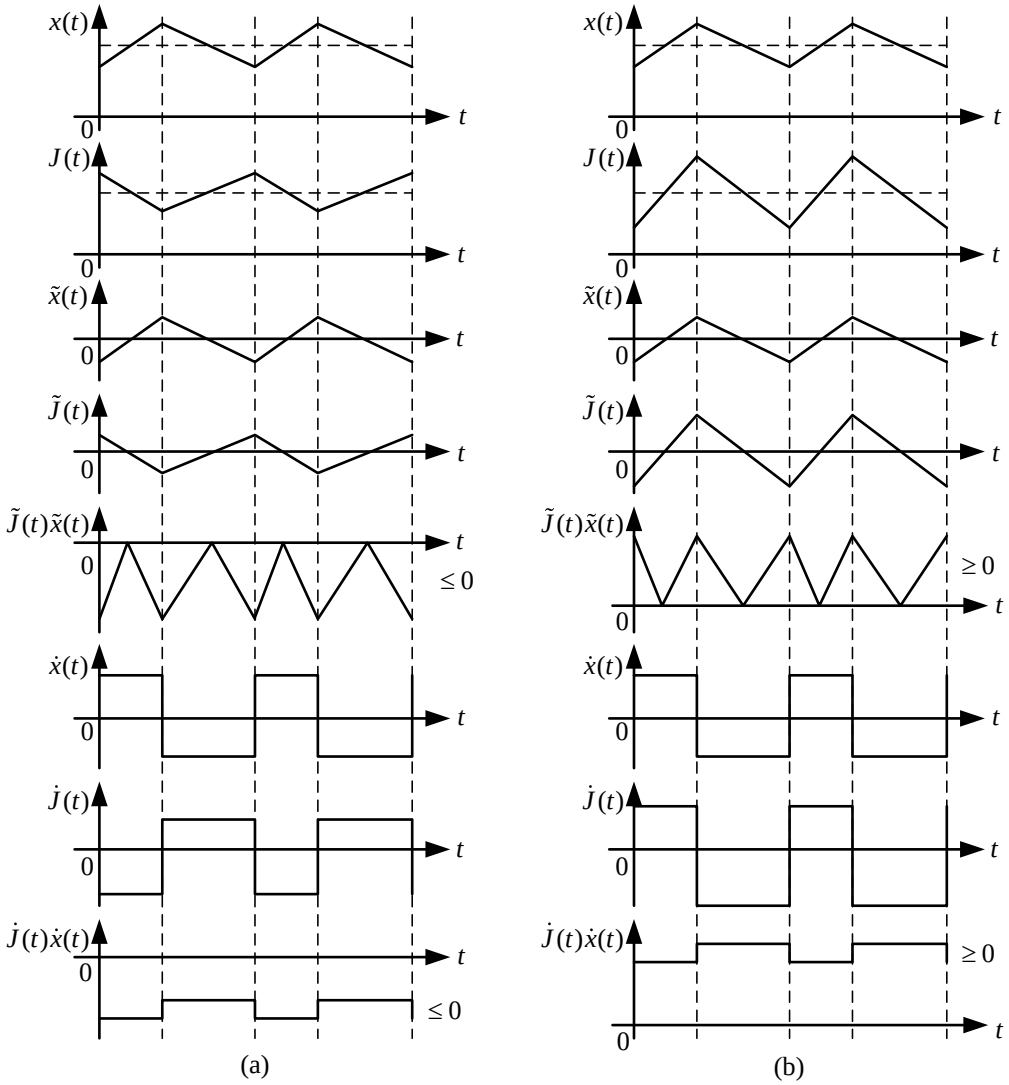

Fig. 14. Triangular ripple and the derivatives of *x* and *y* maintain the same sign for $\text{sign}(\tilde{y}(t)\tilde{x}(t))$ and $\text{sign}(\dot{y}(t)\dot{x}(t))$ when *x* and *y* are (a) out-of-phase by π and (b) in-phase

It is clear from Fig. 14 that the sign of $\tilde{J}(t)\tilde{x}(t)$ and $\dot{J}(t)\dot{x}(t)$ is always the same. Therefore, (21) can be modified to be (23) where δ is a gain.

$$x^*(t) = \delta \int_0^t \text{sign}(\dot{J}(\tau))\text{sign}(\dot{x}(\tau))d\tau \,. \tag{23}$$

Note that the form of (23) is exactly the same as that of (18) for $t_o = 0$. This proves that RCC is ES, and the only difference is the estimation of $\dot{x}(t)$ and. Ripple information is used in RCC, while derivative estimation, direct derivation, or modulation and demodulation are used in ES.

3.1.4 Stability of RCC and ES

Stability analysis of any RCC or ES law, e.g., (3), (18), (19), (23), etc., can be used as RCC and ES where shown to be equivalent. The main RCC law shown in (3) is used for stability analysis. Equation (24) shows this law.

$$x^*(t) = \sigma_s \int_0^t \frac{dJ(\tau)}{dx(\tau)} d\tau \,. \tag{24}$$

Again, a maximization problem is considered, and the proof is similar to that presented in [134] for ES except that the sign of the integrand is used in [134]. For Lyapunov stability analysis, a differential form of (24) is desired; therefore, (24) is written as

$$\frac{dx(t)}{dt} = \sigma_s \frac{dJ(\tau)}{dx(\tau)} \,. \tag{25}$$

Dropping *, t, and τ for simplicity, (25) is written as

$$\dot{x} = \sigma_s \frac{dJ}{dx} \,. \tag{26}$$

A Lyapunov energy-like function $V(t)$ is defined as

$$V(t) = \frac{1}{2}\left(\frac{dJ}{dx}\right)^2, \tag{27}$$

and the derivative of $V(t)$ is thus

$$\dot{V}(t) = \frac{d^2J}{dx^2}\frac{dJ}{dx}\frac{dx}{dt} = \sigma_s \frac{d^2J}{dx^2}\frac{dJ}{dx}\frac{dJ}{dx} = \sigma_s \frac{d^2J}{dx^2}\left(\frac{dJ}{dx}\right)^2 \tag{28}$$

If a maximization problem of a concave objective function is considered, then $\sigma_s>0$, $\frac{d^2J}{dx^2} \leq 0$, and $\dot{V}(t) \leq 0$. Note that in a minimization application $\sigma_s<0$ and $\frac{d^2J}{dx^2} \geq 0$, so $\dot{V}(t) \leq 0$; therefore, $\dot{V}(t) \leq 0$. According to Lyapunov's second theorem on stability, as $V(t) \geq 0$ and $V(t) = 0$ iff $t = 0$, i.e., $dJ/dx = 0$ at the initial time, and $\dot{V}(t) \leq 0$, the system shown in (24) is stable in the sense of Lyapunov. This proves the stability of RCC and ES.

3.2 Ripple Correlation Control as a Loss Minimization Technique

In induction motor applications, λ_{dr} can be used as the control variable to minimize P_{in} or P_{loss}. This choice is based on [52, 53] in addition to simulation and experimental results shown in [19]. Among these results is the one shown in Fig. 4 where the minimum region is relatively flat but P_{in} is still convex. Therefore, λ_{dr} can be used as the control variable. However, other conditions apply for RCC.

One design issue in RCC is to make the ripple amplitude large enough to avoid a small signal-to-noise ratio (SNR), but small enough not to introduce significant oscillations or instability (similar stability discussion for ES and conditions on α_p are shown in [151]). This choice is a general concern at higher frequencies that overlap with the noise spectrum, but power

electronics converters have substantial ripple magnitudes compared to noise. The choice of the ripple frequency is a key aspect of RCC. While in ES literature the frequency ω is chosen to be "small enough" for the dynamic system transients to settle, the choice of ω in RCC literature has been more systematic. In both RCC and ES, ω determines the convergence rate to the optimum. This is clear in RCC — if ω is high, its period is small and less time is needed to arrive at the optimum. But, the question is, how high can ω be? When the real J is known in an ideal scenario, there are no upper limits on ω. But, in real systems, J is either measured or estimated as $\hat{J}(t)$. Measurements have offsets and noise, in addition to calibration errors. Also, when measurements are not available, estimates have estimation errors. Therefore, conversion to $\hat{J}^*(t)$ in the vicinity of $J^*(t)$ is expected. The error introduced by $\hat{J}^*(t)$ affects the frequency choice, especially when the error is large. In real applications, such as MPPT of PV panels and loss minimization in machines, a major source of error between $\hat{J}(t)$ and $J(t)$ is the stored energy not usually accounted for in J when J is P_{in}. This effect can be explained in the following sections.

Example:

The investigation of RCC application to minimize power losses in induction machines has been researched and analyzed in [53, 62, 66]. A major problem is that it requires very low ripple frequencies which are not inherently available in the machine drive. Reference [53] finds the frequency response of the cost function relative to a control variable. The required ripple is only available when running at an extremely low speed, close to stall, where the electrical frequency is close to zero.

A system utilizing RCC with an induction machine under FOC is shown in Fig. 15. The cost function used is P_{loss}, and the control variable is λ_{dr} [53]. Again, maintaining constant P_o, minimizing P_{loss} is equivalent to minimizing P_{in} since $P_{loss} = P_{in} - P_{o.}$

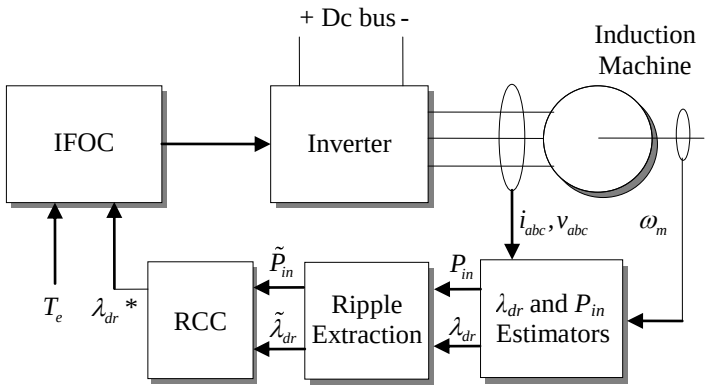

Fig. 15. Typical application of RCC to an induction machine

The transfer function of any perturbations in input power P_{in} owing to changes in flux λ_{dr} is given by

$$\frac{dP_{in}}{d\lambda_{dr}} = \frac{-3L_m}{2D^2}[s(\lambda_{ds}D) + 2\lambda_{dr}L_m R_s - 2(L_{lr} + L_m)R_s\lambda_{ds} - D\omega_e\lambda_{qs}], \tag{29}$$

which is derived from P_{in} under FOC for balanced three-phase conditions as shown in Appendix A, but without core losses. Note that D is a constant gain also defined in Appendix A. The flux λ_{dr} can be varied and the frequency response or Bode plots of input power from (29) can be generated. At the optimal λ_{dr} (λ_{dr}*), the phase of (29) is expected to be at $\pi/2 + n\pi$ radians where n is an integer. Since this is a dynamic application, λ_{dr}* changes in real time because the motor is never in steady state under variable loads and disturbances. But, linearization at a certain operating point is essential to show that the minimum P_{in} exists. Note that substituting for the variables in (29) for an operating point is shown in Appendix A. In this example, an operating point is selected at 2 N·m for a fan load. The resulting convex P_{in} curve is shown in Fig. 16 and

shows the minimum around 300 mV·s. This curve is different from that in Fig. 4 because this approximation is based on an idealized steady-state model of the drive under IFOC without core losses, while Fig. 4 is extracted from simulations of the nonlinear drive model including core losses. A Bode plot of (29) for different values of λ_{dr} is shown in Fig. 17.

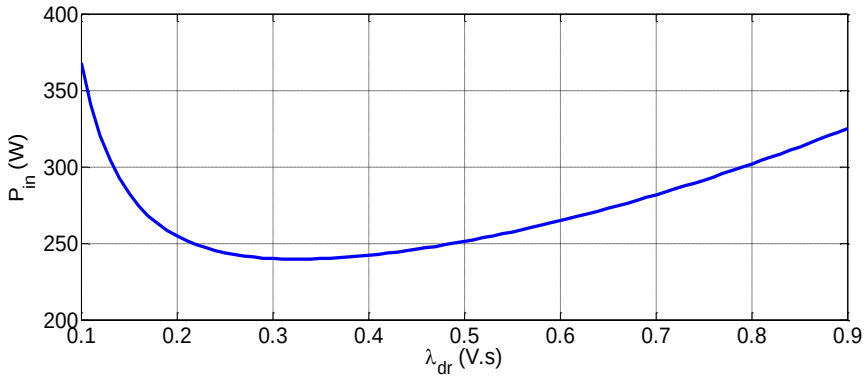

Fig. 16. Convex plot of P_{in} using the steady-state model of P_{in} used in (29)

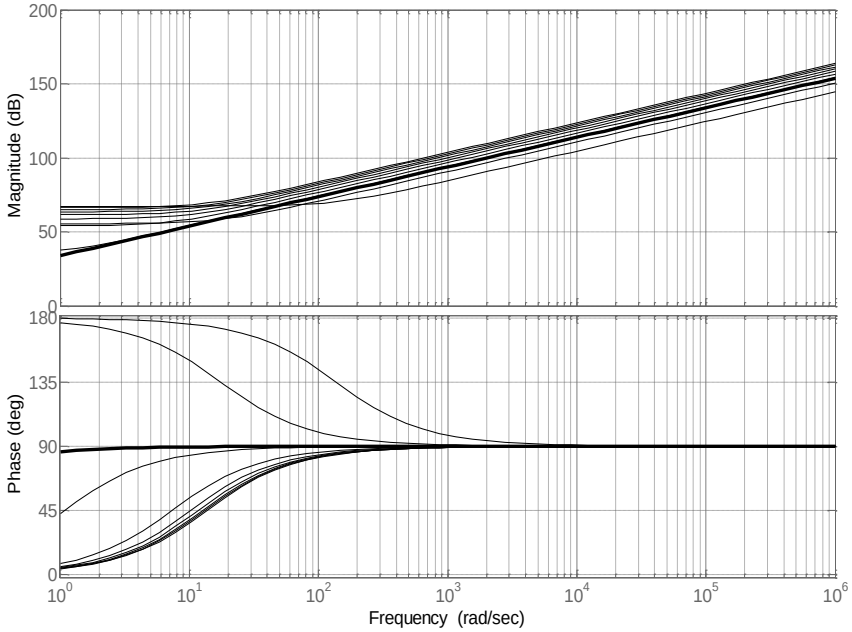

Fig. 17. Bode plots of (29) for 100 < λ_{dr} < 900 mV·s in steps of 100 mV·s, the black line shows the Bode plot at the minimum P_{in}

The phase at the minimum power point is $\pi/2$ radians or 90^{o} and it corresponds to $\lambda_{dr}\approx$300 mV·s. It is clear from Fig. 17 that for the steady-state model there is a single global minimum.

But, the frequency at which this minimum can be identified unambiguously is less than 100 rad/sec or 16 Hz.

3.3 Compensator for Higher Frequency Operation

The limited frequency range for applying RCC, as shown in Fig. 17, is attributable to energy storage in the induction machine.[2] A similar problem was investigated in [71] for RCC in a photovoltaic application. In that case, the storage medium is the photovoltaic panel output capacitance, while in the induction motor case, it is a combination of the leakage and magnetizing inductances.

It is necessary to design compensation for the stored energy to extend the operating frequency range. Given any inductor L carrying a time-varying current $i_{inductor}(t)$ with a voltage drop $v_{inductor}(t)$, the energy stored is $E_{inductor}(t) = \frac{1}{2}Li_{inductor}(t)^2$. As (29) is derived from power rather than energy in the frequency domain, a frequency-domain power expression would account for the energy storage problem. The power in the inductor is given by

$$P_{inductor}(t) = \frac{dE_{inductor}(t)}{dt} = v_{inductor}(t)i_{inductor}(t) = L\frac{di_{inductor}(t)}{dt}i_{inductor}(t). \qquad (30)$$

For an initial current $i_{inductor}(0) = 0$ at $t = 0$, the Laplace transformation is $P_{inductor}(s)=s(\frac{1}{2}LI_{inductor}(s)^2)$ where $I_{inductor}(s)$ is the inductor current in the Laplace domain.

The induction machine *dq0* model is shown in Fig. 18 [154] where L_{lr} and L_{ls} are the rotor and stator leakage inductances, respectively. The total inductor power can be written as

$$P_{ind} = s\left[\frac{1}{2}L_m\left(i_{qs}^2 + i_{qr}^2\right) + \frac{1}{2}L_m\left(i_{ds}^2 + i_{dr}^2\right) + \frac{1}{2}L_{ls}\left(i_{qs}^2 + i_{ds}^2\right) + \frac{1}{2}L_{lr}\left(i_{qr}^2 + i_{dr}^2\right)\right]. \qquad (31)$$

[2] The compensator design presented in this chapter is submitted as an invention disclosure at the University of Illinois number TF10092.

The reason $\left(i_{qs}^2 + i_{qr}^2\right)$ and $\left(i_{ds}^2 + i_{dr}^2\right)$ are used in (31) rather than $\left(i_{qs} + i_{qr}\right)^2$ and $\left(i_{ds} + i_{dr}\right)^2$ is that, physically, the rotor and stator currents do not combine in L_m in either *d* or *q* circuits as might be interpreted from Fig.18. Therefore the cross terms $2i_{qs}i_{qr}$ and $2i_{ds}i_{dr}$ should not be considered. The compensated input power is thus

$$P_{comp,all} = P_{in} - P_{ind}, \tag{32}$$

and

$$\frac{dP_{comp,all}}{d\lambda_{dr}} = \frac{-3}{2D^2}[s(A\lambda_{dr} + B\lambda_{ds}) + 2\lambda_{dr}L_m R_s - 2(L_{lr} + L_m)R_s\lambda_{ds} - DL_m\omega_e\lambda_{qs}], \tag{33}$$

where

$$A = -\left(L_{ls} + L_m\right)\left(L_{lr}\left(L_{ls} + L_m\right) + L_m\left(L_{ls} + 2L_m\right)\right)$$

and

$$B = \left(L_m\right)\left(L_{lr}\left(L_{ls} + L_m\right) + L_m\left(L_{ls} + 2L_m\right)\right).$$

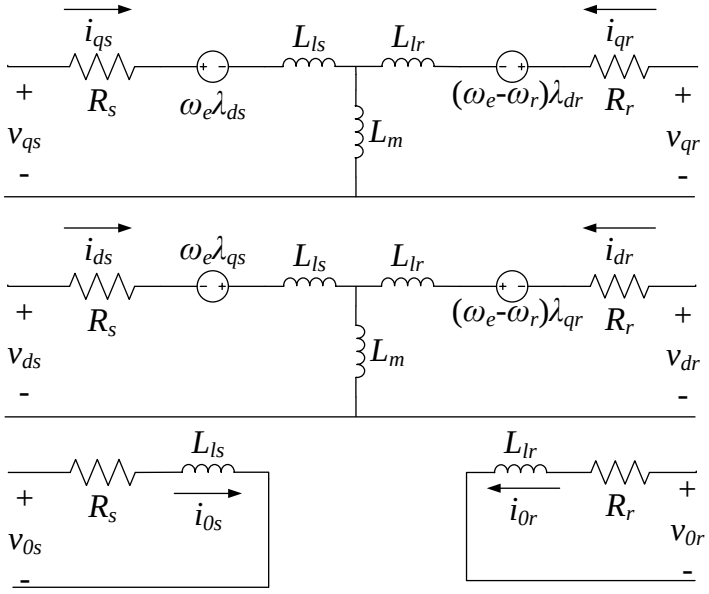

Fig. 18. Induction machine equivalent circuit model

Bode plots of $\frac{dP_{comp,all}}{d\lambda_{dr}}$ are shown in Fig. 19. As expected, with ideal compensation and knowledge of L_m, L_{ls}, and L_{lr}, the frequency range of the compensated transfer function goes to ∞. Phase shifts of 180^o and 0 (or 360^o) below and above the optimum, respectively, are clear. Thus, the optimal λ_{dr} did not change, but the frequency range has been extended.

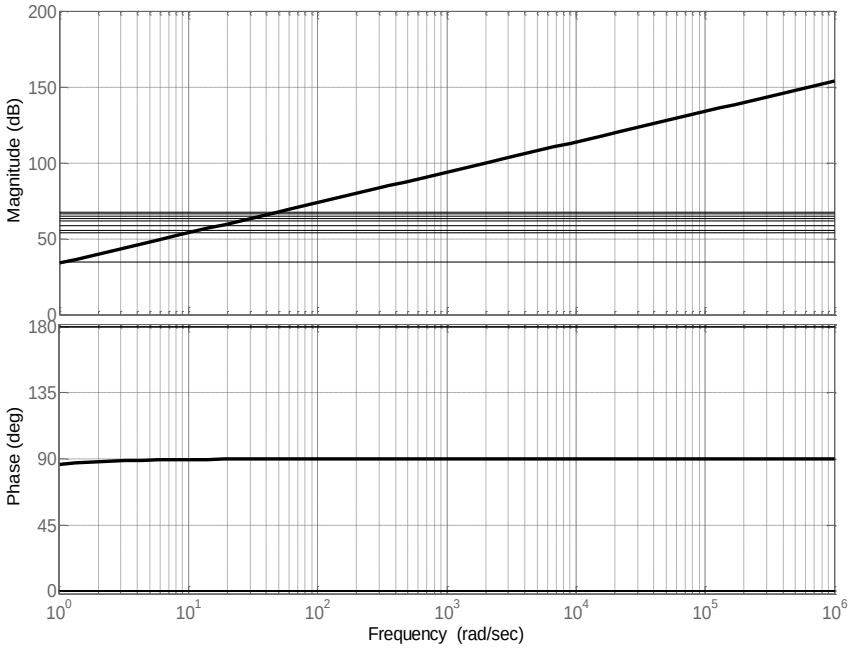

Fig. 19. Ideal compensation showing all points above, below, and at the minimum

This compensation procedure is just a mathematical exercise. Real-life compensation for leakage inductances is a hard task, especially because these inductances are in the range of 1–5% of L_m and are difficult to measure. Therefore, a simpler but non-ideal compensation method with less dependence on motor parameters is desired, representing a potential future implementation. As most of the stored energy is attributed to L_m, which can be approximated from simple motor tests, an effective compensated input power is considered as

$$P_{comp,m} = P_{in} - P_m \text{ where } P_m = s\left[\frac{1}{2}L_m\left(i_{qs}^2 + i_{qr}^2\right) + \frac{1}{2}L_m\left(i_{ds}^2 + i_{dr}^2\right)\right], \quad (34)$$

$$\frac{dP_{comp,m}}{d\lambda_{dr}} = \frac{-3L_m}{2D^2}[sL_m(\Upsilon\lambda_{dr} + \Xi\lambda_{ds}) + L_m(2\lambda_{dr}L_mR_s - 2(L_{lr} + L_m)R_s\lambda_{ds} - DL_m\omega_e\lambda_{qs})], \quad (35)$$

where

$$\Upsilon = -\left(L_{ls}^2 + 2L_m\left(L_{ls} + L_m\right)\right)$$

and

$$\Xi = -\left(L_{ls}L_{lr} + 2L_m^2\right).$$

The Bode plots of $\frac{dP_{comp,m}}{d\lambda_{dr}}$ in Fig. 20 show that the minimum can be identified up to about 3000 rad/sec or 477 Hz. This covers the 120 Hz ripple in single-phase power sources and the 360 Hz from three-phase bridge rectifiers inherent in induction motor drives.

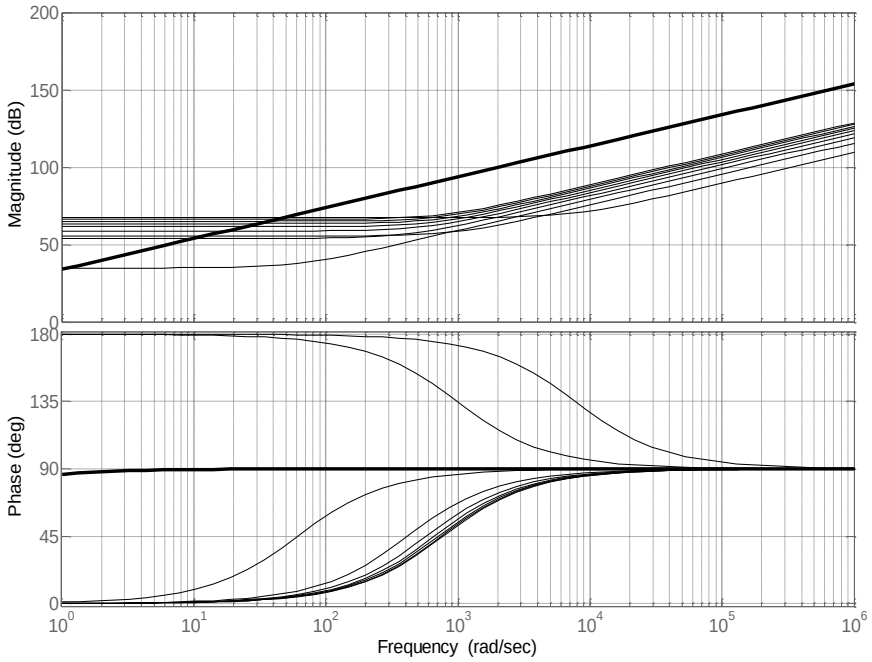

Fig. 20. Bode plots of (21) for 100 < λ_{dr} < 900 mV·s in steps of 100 mV·s

Estimates of leakage inductances and more accurate data about L_m can improve this range, and in principle reach switching frequencies in power electronics converters feeding

induction machines. The optimal value of λ_{dr} does not change, but the ripple frequency range over which RCC is useful has been extended. It is especially important to extend the frequency range to at least 360 Hz to permit rectifier ripple. If it can be extended to 10 kHz or more, then output inverter ripple can be employed for RCC.

3.4 Time-Domain Simulations

Time-domain simulations give a better understanding of the proposed compensator in a real application. An example showing the effect of compensator phase correction between λ_{dr} and P_{in} is shown here. The 1.5 hp motor parameters used are shown in Appendix A. Substituting these parameters in (29), (33), and (35) results in steady-state transfer functions of P_{in}, $P_{comp,all}$, and $P_{comp,m}$, respectively. The results are tabulated in Table 4 where the function is notated $\Theta s + \Omega$.

Table 4. Transfer function parameters for three different cases

System	Θ	Ω
No Compensation	-33.92	2312
Ideal Compensation	0	1541
L_m Compensation	-0.4002	1541

The three systems were simulated, where the input to the transfer function is λ_{dr} + sinusoidal ripple, and the output is P_{in} + ripple. The load condition is maintained at T_e=2N·m. To illustrate, λ_{dr}=500 mV·s, which is above the minimum for the steady-state system. Ideally, the ripples in λ_{dr} and P_{in} should be in phase at any frequency. A 360 Hz, rectifier ripple frequency is used to demonstrate the compensator capabilities. The results in Fig. 2 show that when the system is uncompensated, the phase shift between λ_{dr} and P_{in} is 90^o. This means that RCC would confuse this sub-optimal point with the real minimum. Under ideal compensation, the phase shift is exactly 0^o, which is expected, and allows RCC to track the optimum at any frequency. Usually,

the leakage inductances are not well known, so a compensator considering only L_m was simulated as shown in the bottom plot in Fig. 21. Even though the phase shift under this partial compensation is not exactly zero, it is significantly less than 90^o, and RCC will not confuse it with the optimum.

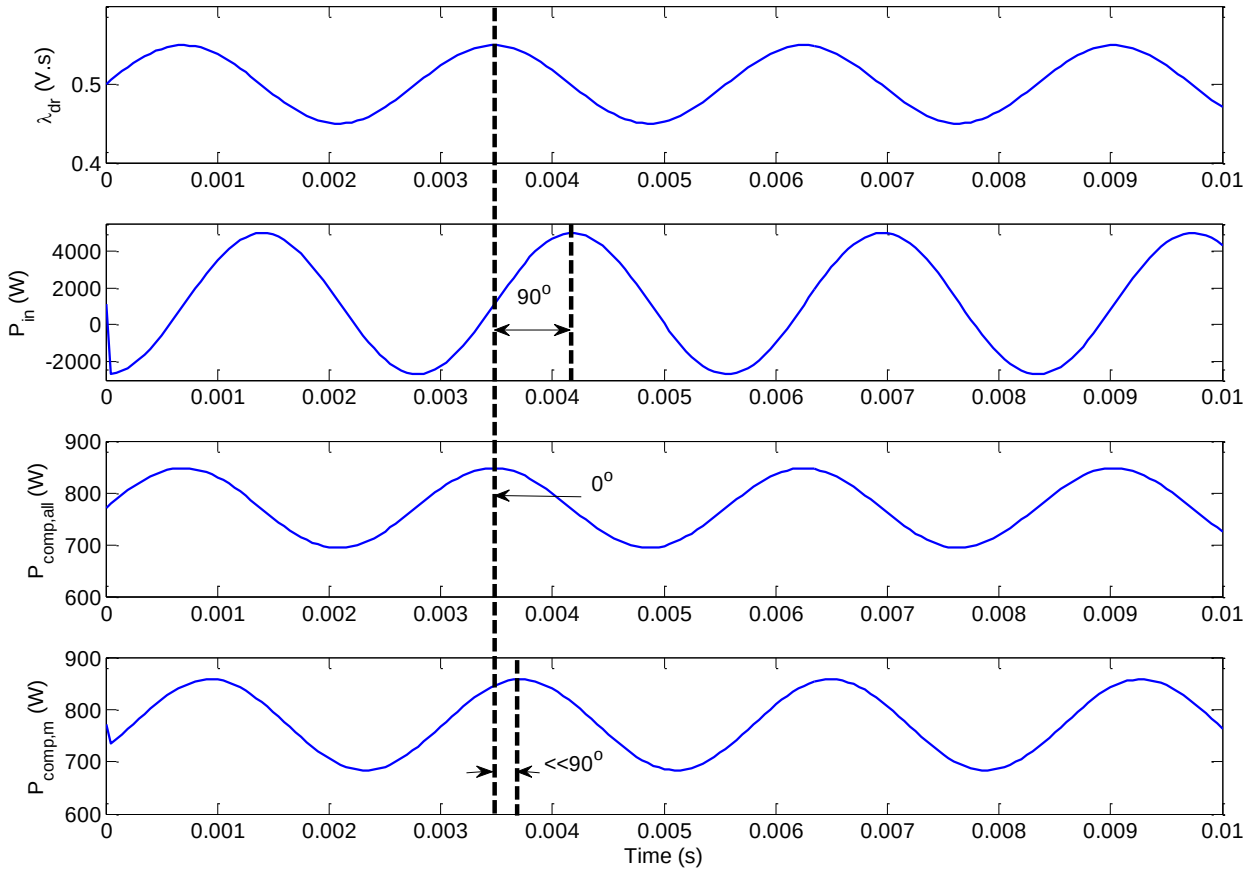

Fig. 21. Time-domain simulations of the uncompensated, ideally compensated, and partially compensated system

CHAPTER 4

LOSS MINIMIZATION TECHNIQUES: APPLICATIONS, COMPARISON, AND ENERGY SAVINGS

4.1 Energy-Saving Potential

Energy savings in a motor drive can be achieved using LMTs reviewed in Section 2.2 and RCC discussed in Chapter 3.[3] Savings vary depending on the convergence accuracy and speed to the minimum P_{in} or P_{loss}. Any LMT is expected to give useful savings in a constant steady-state application. For dynamic loads, fast methods are needed. In this section, the LMT is treated as a black box and the minimum power point is assumed to be known for any load. An illustrative example is used to show the amount of energy saved in a common application—an induction machine in a pump. Energy saved can be calculated by finding the total electrical energy consumed by the machine under nominal operating conditions compared to optimal operating conditions. Hereafter, λ_{dr} is used as the control variable for reasons outlined in Chapters 2 and 3, and P_{in} is the cost function.

Using simulations, experiments, or analytical calculations, P_{in} is found for different loads. The load determines P_o and the efficiency (η) is found as $\eta=P_o/P_{in}$. The efficiency curve shown in Fig. 1 can then be plotted. P_{in} is expected to decrease under an LMT, especially for light loads, and η would increase to become the optimal efficiency (η^*). Here, η^* was found from IFOC simulations employing the 1.5 hp machine under different values of λ_{dr}. The minimum was found for loads stepped from 0 to 100% in 10% increments. LMTs converge to the vicinity of η^*. The resulting η^* is shown in Fig. 22 for different loads. It is clear that at lighter loads, efficiency improvement, loss minimization, and energy savings are significant.

[3] Most of the results presented in this chapter have been published in [18], [19], and [155].

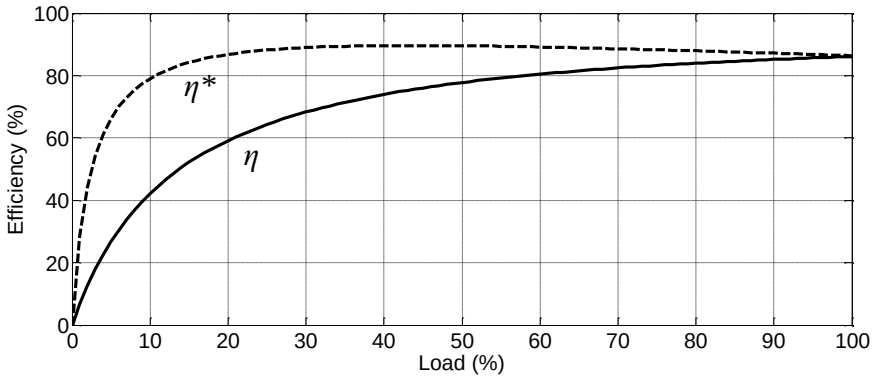

Fig. 22. Nominal (solid line) and optimal (dashed line) efficiencies

Typical pump load profiles, e.g. [155], are used to find the total output energy for a time period. Mapping a load profile to efficiency in Fig. 22 gives the expected efficiency over a time period. A similar load profile to the one shown in [155] is used here. This is typical for a heating, ventilating, and air conditioning (HVAC) pump where the machine frequently operates below rated conditions. The total time interval is 5000 hours and the power has a Gaussian distribution as shown in Fig. 23.

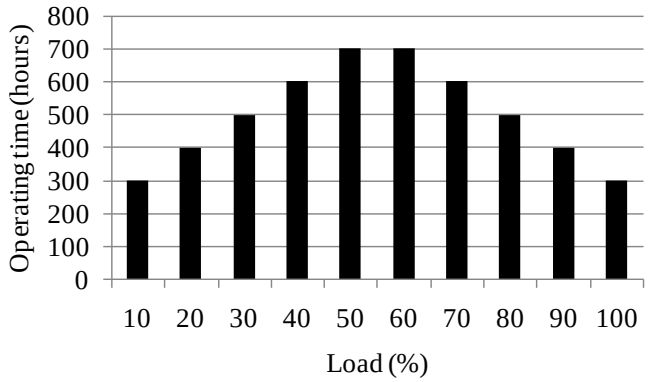

Fig. 23. Load profile for the 1.5 hp induction machine in a pump application

Efficiency points can be extracted for every load under both nominal and optimal operation, then P_{in} is determined as $P_{in} = P_o/\eta$ and P_o is calculated as the load percentage of 1.5 hp or 1119 W. Results are shown in Table 5, and Table 6 shows the total E_{in} and average efficiency for both scenarios. Note that the average efficiency is found as a weighted average based on the histogram of Fig. 23.

Table 5. Efficiency, P_{in}, and E_{in} for nominal and optimal operation (with * superscript)

Load (%)	Time (h)	η (%)	P_{in} (W)	E_{in} (MWh)	η^* (%)	P_{in}^* (W)	E_{in}^* (MWh)
10	300	42.14	266	0.0797	79.05	142	0.0425
20	400	59.16	378	0.151	86.77	258	0.103
30	500	68.29	492	0.246	88.99	377	0.189
40	600	73.94	605	0.363	89.61	499	0.299
50	700	77.74	720	0.5038	89.55	625	0.437
60	700	80.45	835	0.5842	89.17	753	0.527
70	600	82.45	950	0.5700	88.59	884	0.531
80	500	83.97	1066	0.5330	87.91	1018	0.509
90	400	85.16	1183	0.4730	87.16	1155	0.462
100	300	86.1	1300	0.3899	96.37	1161	0.348

Table 6. Total energy and average efficiency from Table 5

Operation	Total E_{in} and E_{in}^* (MWh)	Average η and η^* (%)
Nominal	3.894	70.2
Optimal	3.448	82.8

It is clear from Tables 5 and 6 that overall efficiency improves under optimal operation as expected. Improvements are achieved at low loads where η increases by around 38 points at 10% load. The average increase in η is 12.6% which is also significant. If induction machines are 50% of the global electric load and operate under energy-saving control, global generation can be reduced by 6.27%. Energy savings are also significant where E_{in} dropped by 11.46% from 3.894 MWh to 3.448 MWh for a 5000 h period. The total energy saved for this period is thus 446 kWh or 11.45%. The energy savings are substantial for a large number of pumps run. For example, optimal operation of one million pumps saves 446 GWh of energy. At 10 ¢/kWh, the value of these savings is $44.6 million over a period of 5000 h or 208 days.

The above example shows that if P_{in}^* is achieved, significant energy savings will result and could lead to a reduction in the global energy consumption, generation, and greenhouse gas emissions. In the following sections, P_{in}^* is found using LMTs, but special consideration should

be taken when applying the LMT, including maintaining load support as shown in Section 4.2. Examples that demonstrate the characteristics of LMTs and their energy-saving potential are shown in Sections 4.3 and 4.4.

4.2 Constrained Optimization and the Effect on the Load

It is important to consider the load before applying any LMT to an induction machine. An important observation can be made from induction machine theory: torque is directly related to current and flux. If the flux is set to be weak to achieve energy savings, the optimal flux could be less than the flux needed to support the load torque, and the machine will stall. This was verified in the laboratory and shown in Fig. 24. When the minimum flux linkage ($\lambda_{dr,min}$) is greater than λ_{dr}* and the LMT converges to λ_{dr}*, the machine will not be able to maintain the load torque. Another observation is that the region that includes P_{in}* is relatively flat as shown in Fig. 4, even in the saturation region. While the maximum flux linkage ($\lambda_{dr,max}$) is determined by the machine saturation limits, an LMT can converge to a λ_{dr} that is higher than rated if saturation is not included in a model-based LMT or in simulation models. But, when $\lambda_{dr,max}$ is not considered, the desired outcome is to find out if the LMT achieves P_{in}* regardless of λ_{dr} in the flat region. However, in experiments, $\lambda_{dr,max}$ is an important constraint to avoid saturation. It can be determined from the machine rated flux or flux linkage.

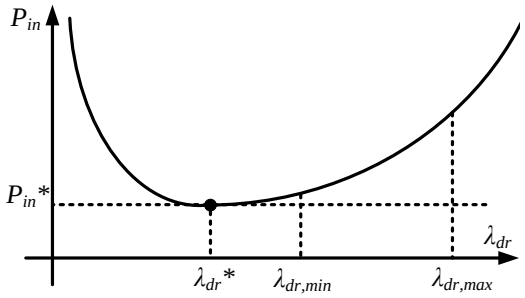

Fig. 24. Situation when λ_{dr} is less than $\lambda_{dr,min}$

To determine the allowed $\lambda_{dr,min}$ for a certain load, λ_{dr} must be formulated as a function of T_e and other states, and its lower bound is $\lambda_{dr,min}$. In an IFOC drive, the limit is found to be

$$\lambda_{dr} \geq \frac{4\gamma_{\lambda} T_e}{3 n_p L_m L_{ls} i_{rated}} \tag{36}$$

where γ_{λ} is a gain and i_{rated} is the rated current in the *dq0* frame. Equation (36) is derived in Appendix B. When $\lambda_{dr}^* < \lambda_{dr,min}$, several solutions exist to mitigate this problem. One is to use a static high value of $\lambda_{dr,min}$ which would prevent λ_{dr}^* from going below $\lambda_{dr,min}$. This solution has a drawback when $\lambda_{dr}^* << \lambda_{dr,min}$ because sub-optimal operation will result when setting $\lambda_{dr}^* = \lambda_{dr,min}$. Another solution is to augment the load into the cost function of P_{in} or P_{loss}. But this has to be custom designed for every LMT or cost function model. The solution discussed below is to dynamically shift P_{in} or P_{loss} with respect to λ_{dr} such that λ_{dr}^* is moved to $\lambda_{dr,s}^*$ where $\lambda_{dr,s}^* > \lambda_{dr,min}$. In Fig. 25 the shift is $\Delta_{\lambda} > |\lambda_{dr}^* - \lambda_{dr,min}|$ and the shifted P_{in} is $P_{in,s}$.

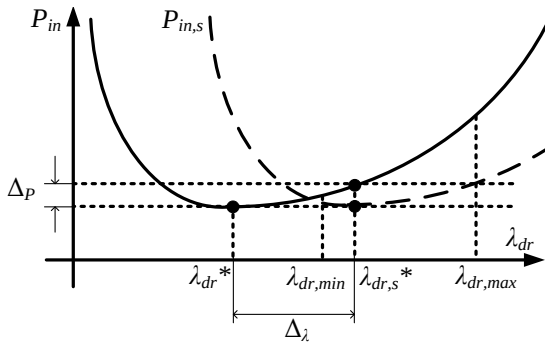

Fig. 25. Shifting P_{in} satisfies $\lambda_{dr,s}^* > \lambda_{dr,min}$ but introduces ΔP_s

Note that this shift would introduce sub-optimal operation in power, quantified as Δ_P, where $\Delta_P \approx 0$W is desired. The upper limit $\Delta_{\lambda} < |\lambda_{dr}^* - \lambda_{dr,max}|$ satisfies the saturation limit but could introduce higher ΔP_s than desired; thus, Δ_{λ} is set to be $\Delta_{\lambda} = |\lambda_{dr}^* - \lambda_{dr,min} + \varepsilon_{\lambda}|$ where ε_{λ} is a small positive value. The shifted P_{in} curve ($P_{in,s}$) can be found for a certain Δ_{λ}. The first step is to formulate P_{in} in terms of λ_{dr} and Δ_{λ}. This can be achieved by using IFOC equations [154]. The curve shift derivation is shown in Appendix B, and $P_{in,s}$ is

$$P_{in,s} = P_{in} + \phi T_e^2 \Gamma + \Lambda, \tag{37}$$

where Γ and Λ are defined in Appendix B. A simpler form of $P_{in,s}$ is desired because equation (37) depends on knowledge of load, motor parameters, and λ_{dr}. For this purpose, two approximations of (37) are studied. The first ($P_{in,s1}$) sets $\Gamma = 1/\lambda_{dr}^2$ and Λ=0, and the second ($P_{in,s2}$) sets Γ=1 and Λ=0. Both are independent of Δ_λ but still depend on T_e. The second approximation is also independent of λ_{dr}. This is an advantage when $P_{in,s}$ is found dynamically without estimating λ_{dr}. For Δ_λ=0.1V·s, $P_{in,}$ $P_{in,s}$, $P_{in,s1}$, and $P_{in,s2}$ are shown in Figs. 26 and 27 for T_e=2 and 4N·m, respectively. Zoomed-in versions are shown in Figs. 28 and 29.

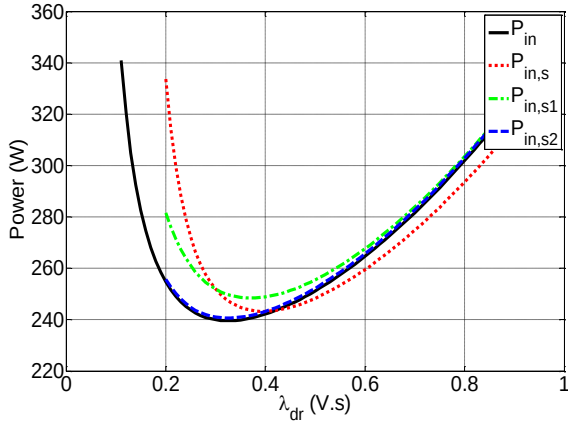

Fig. 26. Shifted and original P_{in} for T_e=2N·m

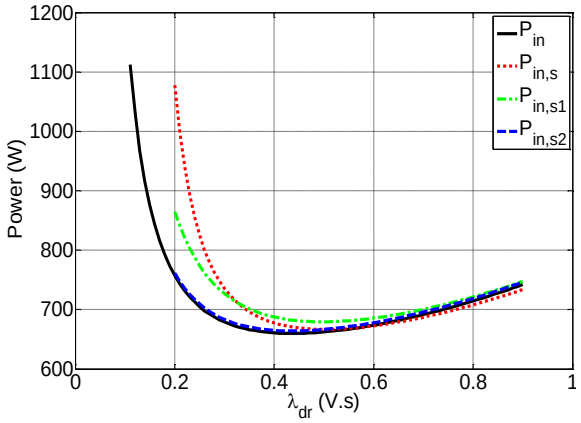

Fig. 27. Shifted and original P_{in} for T_e=4N·m

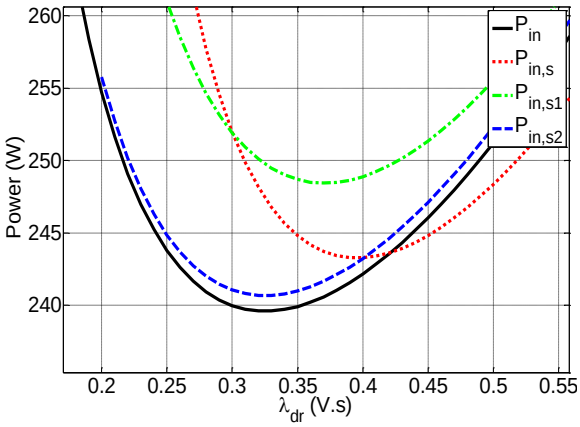

Fig. 28. Zoom in for T_e=2N·m

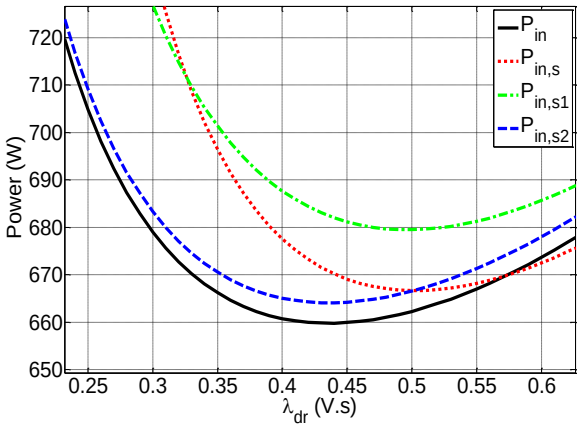

Fig. 29. Zoom in for T_e=4N·m

Figs. 26–29 show that $P_{in,s}$ is shifted by 0.1V·s as expected with minimal Δ_P. Even though the second approximation has minimal $\Delta_P \approx 0$, it does not lead to any significant horizontal shift in P_{in} when the desired Δ_λ is 0.1V·s. The first approximation is still useful to introduce the horizontal shift and introduces smaller Δ_P than that in $P_{in,s}$. Note that Δ_P is defined on $P_{in,s}$ as shown in Fig. 25; thus, the vertical shift of $P_{in,s1}$ does not affect Δ_P. These results suggest that $P_{in,s}$ or its approximation, $P_{in,s1}$, can solve the problem of having $\lambda_{dr}^* < \lambda_{dr,min}$ by introducing the horizontal shift.

4.3 Hybrid Vehicle Motor Drive Application

4.3.1 Model-Based LMT in an HEV Application

The energy-saving potential was studied in a static sense for a pump application in Section 4.1. Energy savings were shown to be significant, but could vary for dynamic applications. HEVs and EVs are important and promising applications of induction motor drives. They have highly variable loads (large ρ) with abrupt braking and acceleration, especially in urban areas. Energy storage in a vehicle is limited to the battery capacity. Combining high load variability with limited battery capacity leads to significant energy bursts in and out of the batteries. Because LMTs reduce the power requirement in an HEV or EV, less energy is drawn from the battery pack. This helps reduce the battery cycling bursts and pack size but poses challenges—the LMT must be faster than the vehicle dynamics in order to achieve meaningful savings, and $\lambda_{dr,min}$ and $\lambda_{dr,max}$ should be selected to avoid any catastrophic stall. The second challenge can be solved using the approach derived in Section 4.2 using an LMT that considers the load. The first challenge requires revisiting the review in Section 2.2.6 where model-based LMTs are expected to be the most suitable for HEV and EV applications. Literature reports that

model-based LMTs are significantly faster than the physics-based LMTs, in general. Hybrid LMTs are also slower than model-based LMTs but can still perform well. Convergence error to the true minimum that could result due to parameter errors in model-based LMTs is of little concern; energy savings with a very fast response time are desired.

A model-based LMT that uses λ_{dr} as the control variable in an IFOC induction motor drive is shown in [52] and in equation (38) (the derivation of (38) is shown in [52]). Equation (38) is suitable for HEV and EV applications because T_e is augmented in the P_{loss} model, which solves the second challenge mentioned above.

$$P_{loss} = \frac{R_s}{L_m^2}\lambda_{dr}^2 + \left(\frac{R_s L_r^2}{L_m^2} + R_r\right)\frac{T_e^2}{\lambda_{dr}^2}. \tag{38}$$

By solving $\partial P_{loss}/\partial \lambda_{dr}=0$, the value of λ_{dr}* can then be found to be

$$\lambda_{dr}^* = \sqrt[4]{\left(L_r^2 + \frac{L_m^2 R_r}{R_s}\right)T_e^2}. \tag{39}$$

To demonstrate the energy-saving potential in an HEV, the induction machine efficiency is evaluated under nominal and optimal flux found using (39). Two methods are used: The first uses the HEV simulator which is described in Section 4.3.2. In these simulations, the HEV is run under different drive cycles for the nominal flux. P_{in}, P_{out} (T_e and the mechanical speed ω_m) are recorded for every simulation sample, then the optimal P_{loss} (P_{loss}*) is found analytically to find P_{in}*= P_{out}+ P_{loss}*. The second uses an experimental setup where the LMT is dynamically applied over a simple driving cycle and P_{in} and P_{in}* are compared.

4.3.2 HEV Simulator

The HEV model used is based on [3] which was experimentally validated with a real HEV and discussed in more detail in [156]. The model includes fuel cell and battery energy storage systems in addition to an IFOC induction motor drive and a traction system. The IFOC block diagram is shown in Fig. 30 where the superscript *c* denotes a command quantity, i_{abc} are the three-phase stator currents, and θ_s is the electrical angle. The induction motor power rating is 10 hp and its parameters are given in Appendix A. The drive model is based on [154] and the battery model was experimentally validated in [157]. The energy storage system sets the inverter V_{dc} which is managed based on the load requirement (energy is stored and dispatched according to the load status). The traction system is based on basic torque equations [158] and an automatic transmission gearbox. The load torques are aerodynamic drag, rolling resistance, inertia, and hill-climbing torques. A high-level block diagram of the simulator is shown in Fig. 31 where P_{load} is the power required by the load.

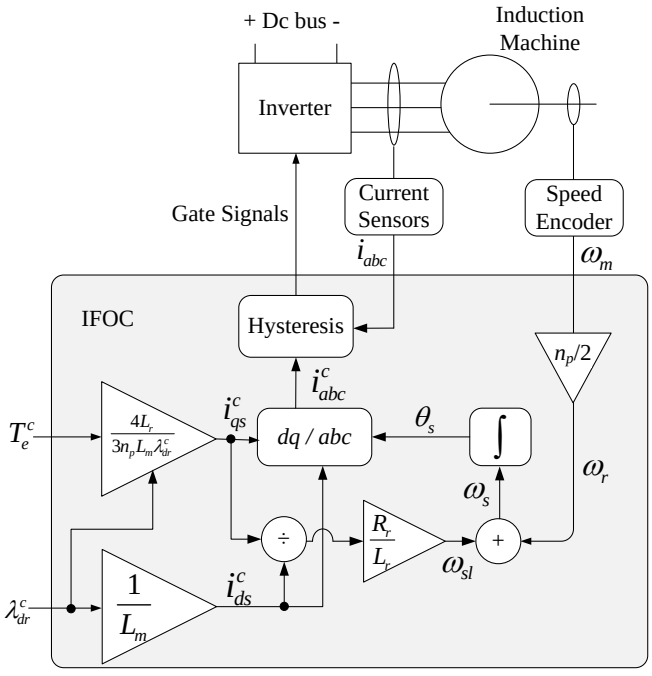

Fig. 30. Block diagram of the motor drive ©2010 IEEE

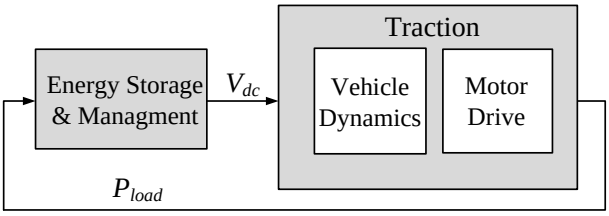

Fig. 31. High-level block diagram of the HEV simulator ©2010 IEEE

The simulator runs in real time and therefore drive cycle simulations do not involve long simulation times. This is achieved by using an XPC target connected to a host computer running MATLAB®. The communication between the target and host computers is established over a TCP/IP network for large data files, or over serial RS-232 for small data files. Simulations are compiled from Simulink onto the target computer which runs them in real-time at a certain sampling rate (as low as 11μs in this case) and then sends the results to the host computer.

The driving cycle or schedule loaded to the simulator contains the desired linear speed profile of the HEV. Interpolated acceleration is mapped to T_e^c using the gearbox and traction equations and the command is sent to the drive model. The drive utilizes the energy storage system for V_{dc}. For vehicle acceleration, the T_e^c is positive, and for deceleration or braking it is negative.

4.3.3 Evaluation of Energy Savings

Efficiency maps are often used to estimate machine efficiency for different torque-speed operating points. They produce a static map which can be mapped to a load profile [159]. Their main drawback is ignoring the machine transient response even though transients include significant energy flow. The HEV and EV literature has focused on these maps, and vehicle dynamics are not usually considered. This leads to inaccuracies when evaluating machine

efficiency. An example of an efficiency map is shown in Fig. 32 and is available along with other maps in [160].

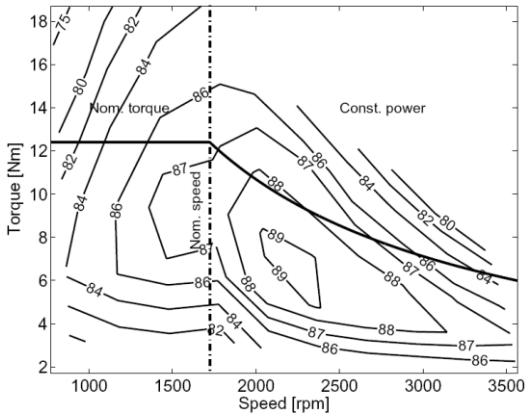

Fig. 32. Efficiency map of an induction machine for high-voltage wye arrangement at 100% flux level [160]

Comparison of HEV machine efficiency under nominal and optimal operation is shown in [161] where the comparison is based on the dynamic evaluation of P_{in} and P_o. This evaluation helps find the overall *energy efficiency* (α) defined as the ratio of total E_o over the total E_{in} where total energies are evaluated for a complete driving cycle. Also, E_{in} can be translated to a dollar value and savings when compared to E_{in}*. Another comparative evaluation is based on the *dynamic efficiency* (η_j) which is the ratio of the instantaneous P_o over P_{in} for an instant j. Note that P_{in} and P_o can change form: P_{in} is electrical and P_o is mechanical for motor operation, while P_o is electrical and P_{in} is mechanical for generator operation (regeneration). It is expected that under an LMT, both α and the average η_j ($\bar{\eta}$) would increase to α* and the average η_j* ($\bar{\eta}$*).

4.3.4 Results and Remarks[4]

Published driving schedules were used to evaluate α, α*, $\bar{\eta}$, and $\bar{\eta}$*. Urban schedules include dynamic acceleration and braking while highway schedules are less variable. The

[4] Comparisons of an induction machine and a PMSM of similar ratings in the HEV simulator are shown in [153]. Results show that the induction machine under loss minimization control could have a comparable efficiency to the PMSM.

schedules, shown in Table 7, are available on the Environmental Protection Agency (EPA) website [162] and include those from the United Nations Economic Commission for Europe (UN/ECE).

Table 7. Driving schedules from [162] ©2010IEEE

Driving Schedule	Source	Time (s)
Urban Dynamometer Driving Schedule (UDDS)	EPA	1364
Highway Fuel Economy Driving Schedule (HWYFET)	EPA	765
New York City Cycle (NYCC)	EPA	598
Elementary Urban Cycle (EUC)	UN/ECE	195
Extra-Urban Driving Cycle (EUDC)	UN/ECE	400

The driving schedules were all run under nominal and optimal flux from equation (39). Sample results are shown in Figs. 33 and 34 for one highway schedule (HWYFET) and another urban schedule (EUC). Results of other schedules show, like these, that η^* forms an envelope around η and overall energy savings can be achieved under efficiency improvement. Note that in Figs. 33 and 34, neither η nor η^* reaches 100%, but at some transient points P_{in} and P_o nearly match as the drive makes the dynamic transition between motoring and braking.

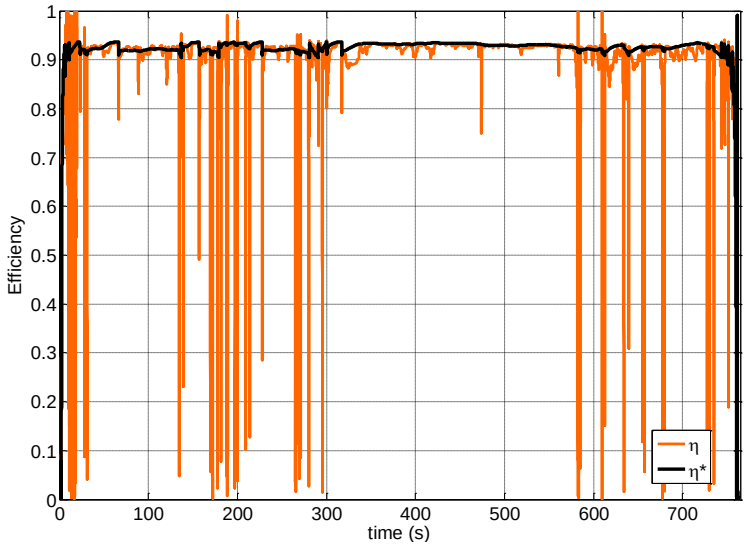

Fig. 33. Induction machine efficiency under rated and optimal flux for HWFET ©2010 IEEE

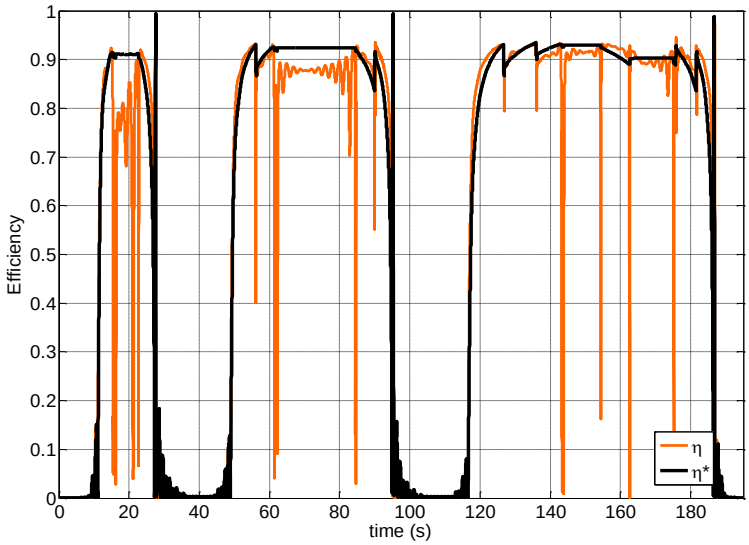

Fig. 34. Induction machine efficiency under rated and optimal flux for EUC ©2010IEEE

A numerical comparison of $\bar{\eta}$ and $\bar{\eta}^*$ for all five driving schedules is shown in Table 8. As expected, $\bar{\eta}^*$ is higher than $\bar{\eta}$ for all schedules, with an average improvement of two points. While these savings are not large, they impact battery sizing and overall efficiency. Some values of $\bar{\eta}$ and $\bar{\eta}^*$ are low, because when the HEV stops, $\bar{\eta}$ and $\bar{\eta}^*$ are both zero. If the stall points are excluded from any schedule, $\bar{\eta}$ and $\bar{\eta}^*$ will be significantly higher; their average is about 90%.

Table 8. $\bar{\eta}$ and $\bar{\eta}^*$ for five driving schedules ©2010 IEEE

Driving Schedule	$\bar{\eta}$ (%)	$\bar{\eta}^*$ (%)
UDDS	69.61	72.76
HWYFET	89.71	91.67
NYCC	49.39	51.91
EUC	59.21	60.24
EUDC	82.05	83.50

Another numerical comparison is for α and α^*. E_{in}, E_{in}^*, and E_o are found from the simulation results similar to those in Figs. 33 and 34. E_o is the same under nominal and optimal operation. If the data sampling rate is 1 s, the sum of P_{in} multiplied by the schedule time with appropriate h/s conversion (K) would be E_{in}. However, the number of samples (N_s) is

significantly higher due to the small step size (S_s) of 11 μs/sample, so the following equation can be used to find E_{in}, E_{in}*, and E_o where E_{in} is shown as an example:

$$E_{in} = \sum_{j=1}^{N_s} P_{in,j} \times S_s \times K \,. \tag{40}$$

In equation (40), the units are W·samples for $\sum_{j=1}^{N_s} P_{in,j}$, s/sample for S_s, and h/s for K to give E_{in} in Wh. The total energy results of all five schedules are shown in Table 9, and the resulting energy efficiencies (both α and α*) are shown in Fig. 35. It is clear in Table 9 that E_{in}*<E_{in} as expected. Therefore, the total energy drawn from the storage medium is less under an LMT. Having E_{in}*<E_{in} directly translates to α*<α as shown in Fig. 35. The average improvement in α is 4.22 points, which is significant especially with limited energy storage.

Table 9. Input and output energies for different drive cycles under rated and optimal flux ©2010 IEEE

Driving Schedule	E_{in} (KWh)	E_{in}* (KWh)	E_o (KWh)
UDDS	0.9620	0.9083	0.7253
HWYFET	1.6462	1.6067	1.4632
NYCC	0.1778	0.1458	0.0871
EUC	0.0653	0.0647	0.0489
EUDC	0.7110	0.6870	0.6170

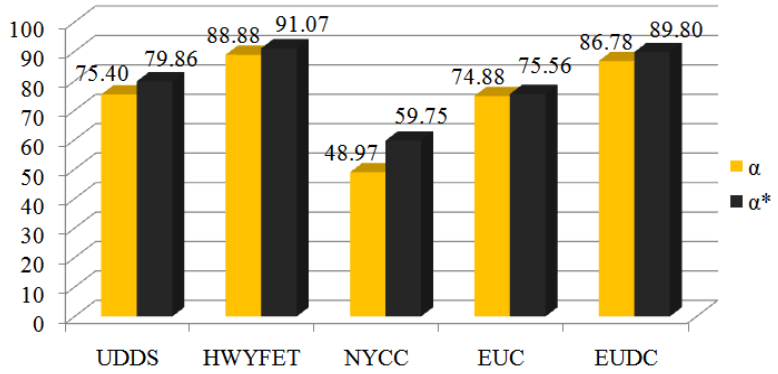

Fig. 35. Nominal and optimal energy efficiencies for five drive cycles ©2010 IEEE

A simplified driving schedule was tested to validate the energy savings experimentally and show the efficiency improvement under dynamic LMT based on (39). The setup of the induction motor drive under IFOC is described in Appendix C [163]. The driving schedule used

is shown in Fig. 36 and involves acceleration, deceleration, braking, and steady speed with torque steps— resembling hill climbing. This sample schedule serves the intended goal of demonstrating energy savings for various dynamic operations common in an HEV. It can be applied in two-quadrant dynamometers which are widely available and less expensive than four-quadrant dynamometers. Experimental results of P_{in} and P_o and their averages, for both nominal and optimal flux operation are shown in Figs. 37 and 38, respectively.

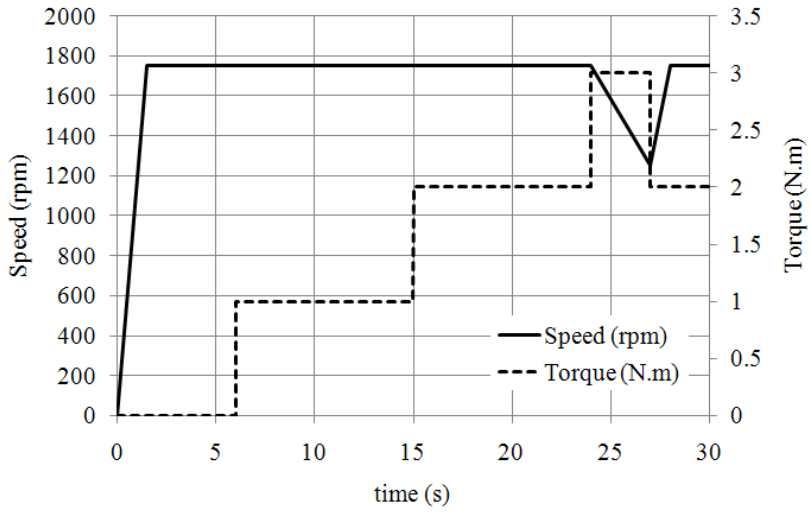

Fig. 36. Short driving schedule used in experiments ©2010 IEEE

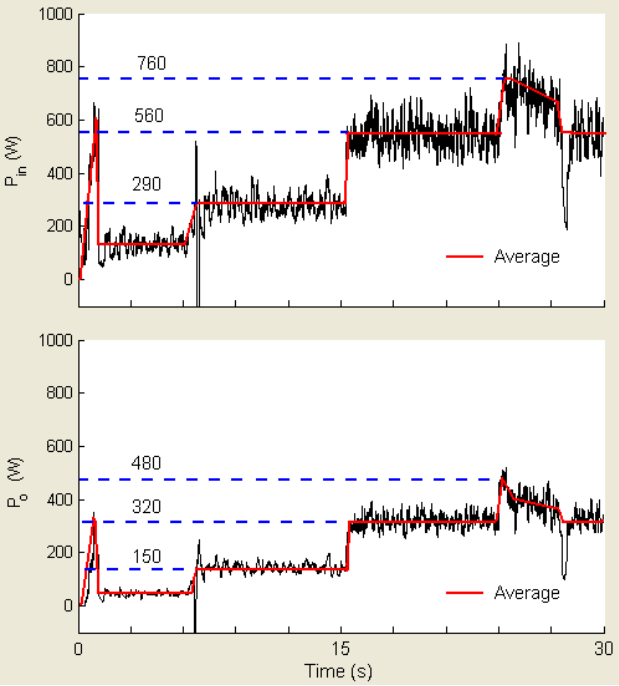

Fig. 37. Experimental results for P_{in} and P_o under nominal operation ©2010 IEEE

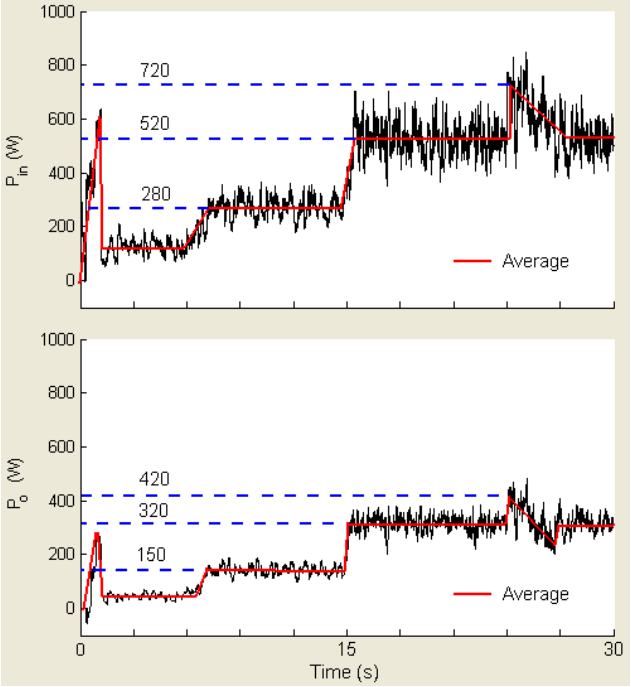

Fig. 38. Experimental results for P_{in}* and P_o under optimal operation ©2010 IEEE

Figure 38 shows that, as expected, P_{in}* is generally less than P_{in} for different operating conditions. This leads to having E_{in}*<E_{in}, α*<α, and $\bar{\eta} < \bar{\eta}^*$. These results are shown in Table 10. The energy and dynamic efficiency numbers shown in Table 10 are relatively low due to the light load operation. Note that in Fig. 36 the maximum torque applied is 3N·m while the rated torque is 6.1N·m. The motor has lower efficiencies at light loads compared to the rated load, as shown in Fig. 1. As shown in Table 10, the average dynamic efficiency improves by 2.66 points, and the energy efficiency improves by 3.4 points. These results are similar to the HEV results shown in Table 8 and Fig. 35, but the energy savings in an HEV are greater because the percentage savings are from a larger E_{in} or P_{in} due to the larger HEV motor.

Table 10. Numerical results from the experimental driving schedule ©2010 IEEE

$\bar{\eta}$ (%)	$\bar{\eta}^*$ (%)	E_{in} (Wh)	E_{in}* (Wh)	E_{out} (Wh)	α (%)	α* (%)
54.69	57.35	3.42	3.23	1.94	56.7	60.1

4.4 Propulsion Application

4.4.1 Propulsion Load and Loss Minimization

Electric ship propulsion is an application of large electric machines. The first machines used were dc with power limited to 10,000 hp. They suffer from high repair and maintenance requirements [164]. Newer propulsion systems use ac machines, specifically induction machines. Their power range goes up to 33,000 hp or 20–25 MW [164, 165]. With high power ratings, any loss minimization would be significant. For example, 5% energy savings in a 20 MW machine could be enough to power most auxiliary loads, such as lights on board a ship. Multiphase induction motors are usually used in electric ships because of their high torque density, high efficiency, low torque pulsations, flexibility of power conditioning, and fault tolerance [166-168]. A three-phase machine is used here for laboratory testing.

A propulsion load is studied to compare LMTs in real time. This load is usually used to model fans and propellers where, according to the propeller law, the power required by the propeller (P_{prop}) is a cubic function of the velocity (V_{prop}) of the propelled body. Given a constant, k_{prop},

$$P_{prop} = k_{prop} V_{prop}^3 . \tag{41}$$

Here, P_{prop} is the machine power and is the product of T_e and ω_m, where ω_m and V_{prop} are linearly related [169]. Thus, T_L=T_e in steady state, is a quadratic function of ω_m,

$$T_L = k_{load} \omega_m^2 . \tag{42}$$

The constant k_{load} can be calculated from machine ratings. For example, for the 1.5 hp machine used in the following simulations and experiments, the rated ω_m is 1750 rpm or 183.26 rad/s, and

the rated torque is 6.1 N·m. Setting T_L=6.1 N·m and ω_m=183.26 rad/s, and solving (42) yields k_{load} =1.816×10^{-4} N·m/(rad/s)^2.

All three real-time or online LMT categories are tested with the propulsion load, shown in equation (42), using the same simulation and experimental setup. This provides common ground for comparing LMTs [18], necessary because of the multiplicity of machine ratings, loads, and controllers used to demonstrate LMT operation in various publications. The simulations use IFOC and the induction machine model from [154]. The experimental setup is described in Appendix C. All LMTs use λ_{dr} as the control variable for reasons described earlier. The model-based LMT is based on equations (38) and (39), where P_{loss} is the cost function. It uses an estimate of T_e and some motor parameters to set λ_{dr}*. The physics-based LMT is a simple P&O described in Fig. 6 where P_{in} is the cost function. It samples P_{in} and λ_{dr} every 1 s after system transients settle. The hybrid LMT is RCC with P_{in} as the cost function. Due to the high-frequency problem when applying RCC to induction machines, a slow low-amplitude perturbation at 4 Hz is injected to λ_{dr} for RCC simulations. This makes RCC similar to modern ES as shown in Fig. 13 where the perturbation is

$$x_p(t) = \tilde{\lambda}_{dr}(t) = 20\sin(8\pi t)\,\text{mV·s}$$

compared to the rated flux of 500 mV·s.

4.4.2 Simulation Results

Simulation results for the three LMTs are shown in Figs. 39–41 for T_L=2 N·m and ω_m=ω_{rm}=1000 rpm. LMTs are expected to converge to between 600 and 800 mV·s, as shown in Fig. 4. The initial λ_{dr} command is 200 mV·s which is significantly lower than the rated λ_{dr} at 500

mV·s. This low initial condition is outside the flat minimum-P_{in} region and clearly shows the transient response of the LMT.

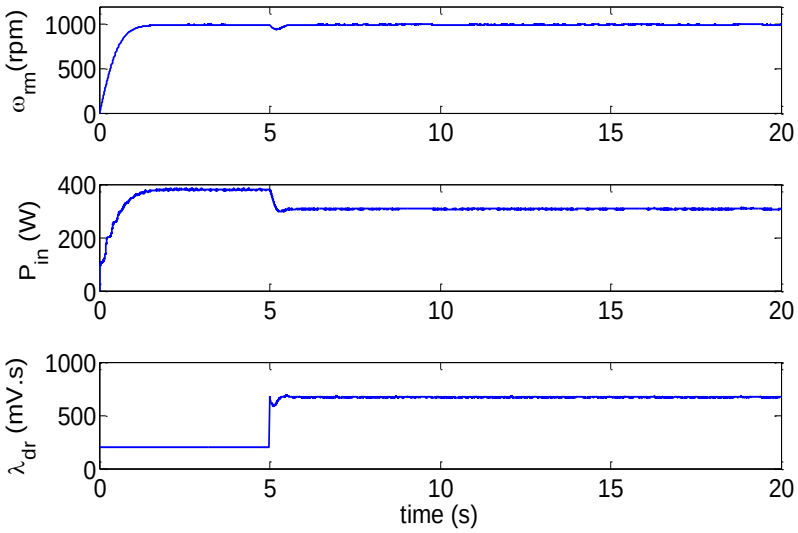

Fig. 39. Simulation results for model-based LMT ©2010 IEEE

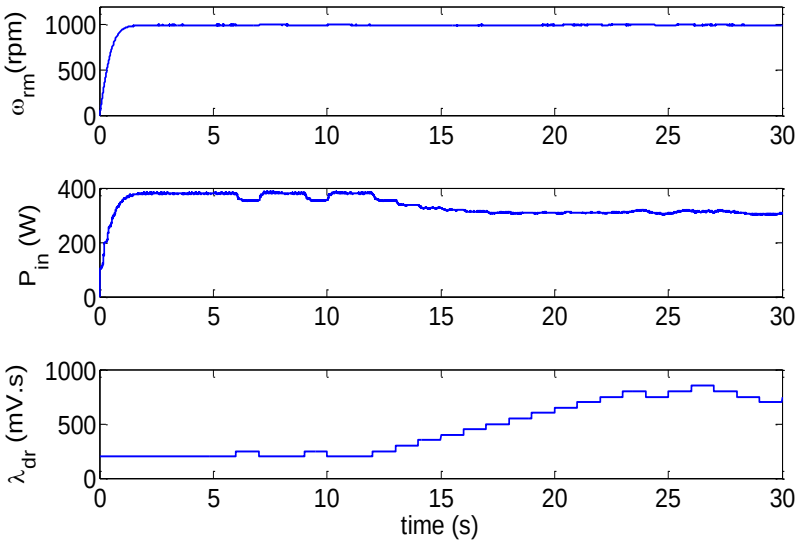

Fig. 40. Simulation results for physics-based LMT ©2010 IEEE

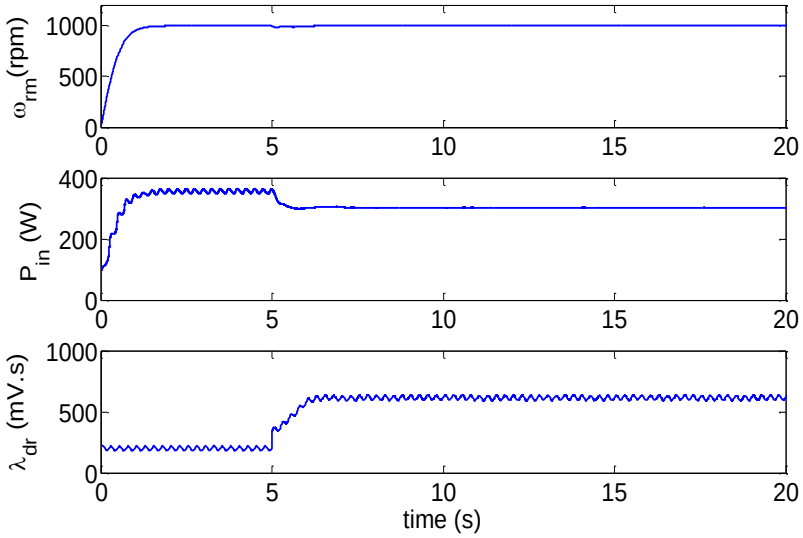

Fig. 41. Simulation results for hybrid LMT (RCC) ©2010 IEEE

All three LMTs converge to λ_{dr}* near 680 mV·s, as expected. In general, λ_{dr}* would be less than the rated λ_{dr} for a real machine, but in these simulations, saturation is not considered and therefore higher flux is not penalized. The model-based LMT shows convergence within 250 ms, fast enough to track sub-second load changes. Sensitivity to machine parameter errors is studied later. The physics-based LMT converges slowly to the vicinity of λ_{dr}*, then oscillates. These oscillations are significant, since the minimum region is relatively flat. The hybrid LMT shows fast convergence and low oscillations when compared to the physics-based LMT. The oscillation amplitude depends on that of the injected perturbation or inherent ripple. The hybrid LMT depends on fewer parameters and has lower parameter sensitivity compared to the model-based LMT. These results show that with accurate machine parameter knowledge, model-based LMTs perform well. When no parameter knowledge is assumed, physics-based LMTs should be used despite their slow convergence. Applications that have low load variability, or small ρ, and long runtimes can use physics-based LMTs, as the minimum P_{in} does not change significantly and slow convergence time is not an issue. Physics-based LMTs with small step sizes have lower-amplitude oscillations at the cost of slower convergence times. Adaptive physics-based

LMTs, such as the adaptive P&O algorithm presented in [64], can reduce convergence time and oscillations but are still outperformed by model-based and hybrid LMTs.

4.4.3 Experimental Results

Experimental results for the model- and physics-based LMTs are shown in Figs. 42 and 43, respectively, for the same operating condition described in Section 4.4.2. Channel 1 is ω_m in rpm, Channel 2 is P_{in} in W, and Channel 3 is the λ_{dr} command in mV·s. The load is applied at t=9 s, and the LMT is engaged at t=16 s. These results are similar to those shown in Figs. 39 and 40. The main difference is that the LMTs converge at or near 470 mV·s<500 mV·s, as expected. The convex plot of the LMTs with measurement error bounds in Fig. 44 shows the expected minimum. In Fig. 42, the model-based LMT responds quickly, similar to a step command due to the fast calculation of λ_{dr}* on the DSP. Figure 43 shows that the physics-based LMT has slower convergence time and requires several seconds to reach the minimum-P_{in} region of the minimum P_{in}. Both figures show that the load is well maintained at a speed of 1000 rpm when the torque is set through an external loop at 2 N·m.

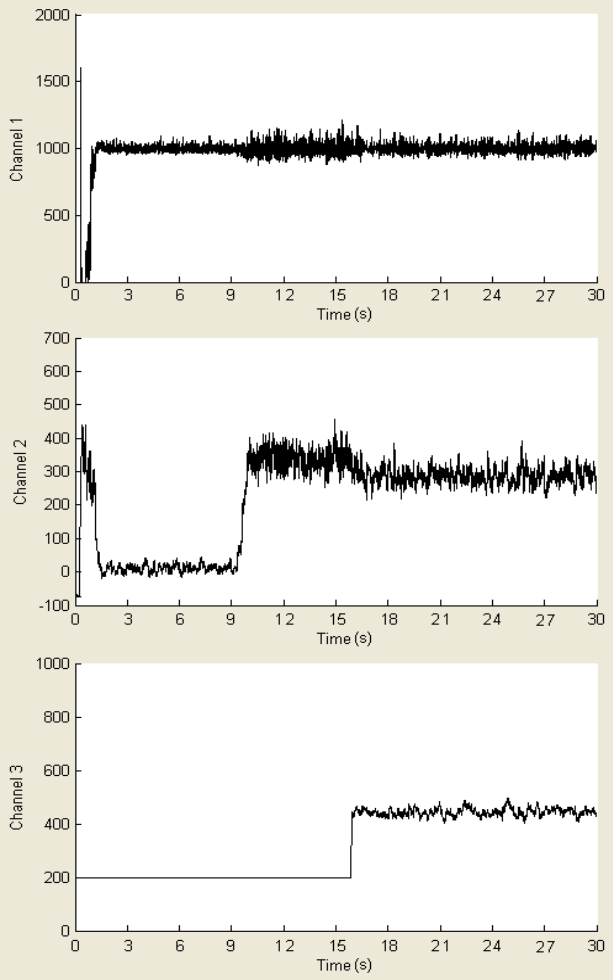

Fig. 42. Experimental results for model-based LMT Channel-1: ω_m (rpm), Channel-2: P_{in} (W), and Channel-3: λ_{dr} command (mV·s) ©2010 IEEE

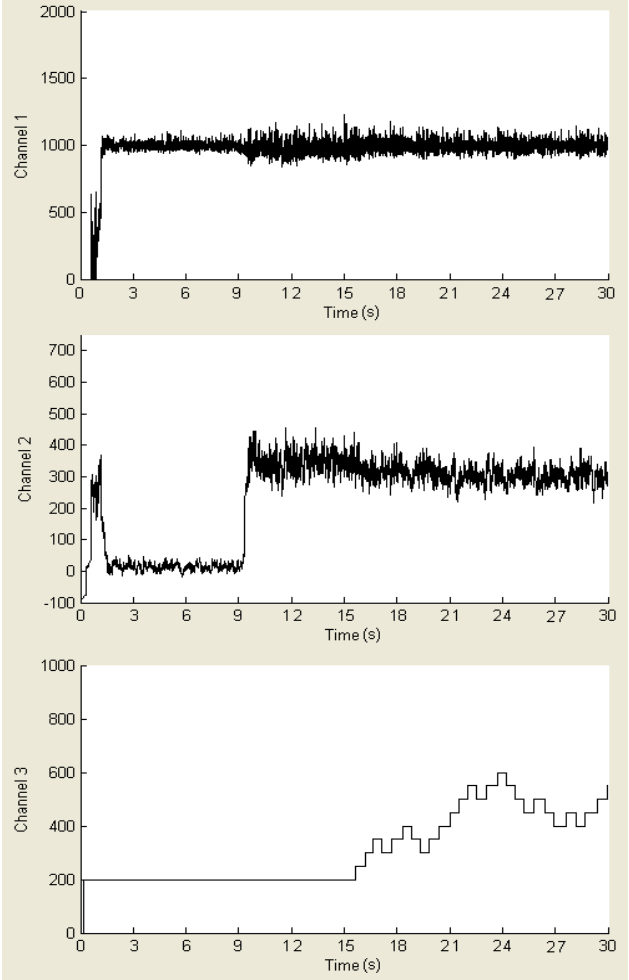

Fig. 43. Experimental results for physics-based LMT Channel-1: ω_m (rpm), Channel-2: P_{in} (W), and Channel-3: λ_{dr} command (mV·s) ©2010 IEEE

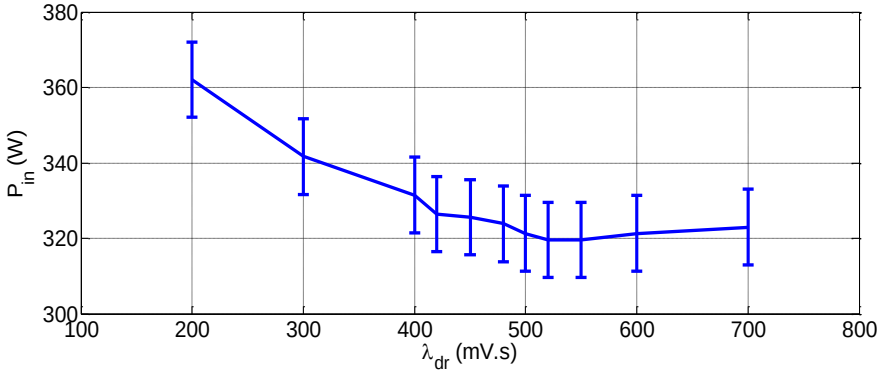

Fig. 44. Experimental results for convex plot of P_{in} vs λ_{dr} with measurement error bars ©2010 IEEE

Results in Figs. 39 and 42, and Figs. 40 and 43 match each other and the performance predictions. Minor discrepancies between experimental and simulation results are due to motor parameter errors and the fact that saturation is not modeled in simulations. Table 11 summarizes the simulation and experimental results. The hybrid LMT (RCC) was not experimentally tested due to challenges with the signal amplitude. Low amplitudes have low SNR in the available setup, while high amplitudes introduce significant audible oscillations in the speed. Also, high amplitudes span most of the minimum-P_{in} region which makes identifying P_{in}* a complex task.

Table 11. Summary of results from simulations and experiments for propulsion load

	P_{in} (W)	P_{in}* (W)	λ_{dr}* (mV·s)	Model-based LMT convergence time (s)	Physics-based LMT convergence time (s)	Hybrid LMT convergence time (s)
Simulations	380	315	620	<1	≈15	≈2
Experiments	345	315	470	<1	≈9	N/A

4.4.4 Sensitivity Analysis

Physics-based LMTs are insensitive to errors or inaccuracies in machine parameters depending instead on accurate measurements during the loss minimization process. Parameter sensitivity remains a concern for model-based and hybrid LMTs despite their superior performance. The model-based LMT based on (38) and (39) is used here for parameter sensitivity analysis. This analysis is performed by evaluating the difference between P_{loss}* and P_{loss} under parameter errors (P'_{loss}). The flatness of P_{in} or P_{loss} around the minimum, as shown in Fig. 4 and Fig. 44, is expected to result in low sensitivity for parameter inaccuracies, except in extreme cases.

Let P_{loss} be a function (ϑ) of Ψ parameters, $r_1 \ldots r_\Psi$, in addition to λ_{dr} where

$$P_{loss} = \vartheta(\lambda_{dr}, r_1, ..., r_\Psi) . \tag{43}$$

Inaccuracy or error in parameter r_i (Δr_i) results in a drift from the optimal λ_{dr}* to a non-optimal λ'_{dr} where P'_{loss} is

$$P'_{loss} = \vartheta(\lambda'_{dr}, r_1, ..., r_i + \Delta r_i, ...r_\Psi). \quad (44)$$

In (38), Ψ=4 where r_1=R_s, r_2=R_r, r_3=L_r, and r_4=L_m. Table 12 shows variations in P_{loss} due to variations in r_1–r_4. The second column in Table 12 is calculated as (P_{loss}-P'_{loss})/P_{loss}.

Table 12. Sensitivity of P_{loss} to variation in motor parameters ©2010 IEEE

Parameter error from nominal	P_{loss} increase from nominal
+20% R_s	16.84%
+50% R_s	44.99%
+30% R_r	4.57%
+50% R_r	7.51%
+20% L_r	14.14%
+50% L_r	36.39%
-10% L_m	19.74%
-50% L_m	250.11%

In induction machines, R_r is hard to estimate because it can vary with temperature, saturation, and other operating conditions. It is clear in Table 12 that even 50% errors in the R_r estimate lead to less than an 8% increase in P_{loss} where the model-based LMT would converge. Other parameters are usually well known and more stable, especially R_s and L_m. L_r=L_m+L_{lr}, L_s=L_m+L_{ls}, and L_{ls}, L_{lr}<<L_m; thus, estimates of L_r and L_s are well known. Even so, inaccuracies of 10 or 20% in these parameters do not cause more than a 20% increase in P_{loss}. This sensitivity analysis suggests that the parameter-inaccuracy concern in the model-based LMT presented here might be acceptable given the wide minimum range. Hybrid LMTs have less parameter dependence on machine parameters and are expected to have lower sensitivity. Note that different model-based LMTs have different parameter sensitivities and the numbers shown in Table 12 cannot be generalized.

4.5 Comparisons and Remarks

Based on the comparison from the literature review presented in Sections 2.2.6, 4.1, 4.3 and 4.4, energy savings in induction machines are possible and achievable. In the pump example in Section 4.1, 12% energy savings were shown for a typical HVAC pump. Loss minimization in the HEV was shown to be significant with efficiency improvement on the order of 2–4 points. Loss minimization in the 1.5 hp machine was also shown to be significant on the same order. A long-term target would be to apply LMTs of any kind in all future motor drives where any efficiency improvement and loss minimization would have substantial positive effects on the global environment, electricity generation, and cost.

The literature review in Section 2.2 concluded with comparisons of different LMTs, based on different drives. Section 4.4 showed dynamic real-time loss minimization of the three online LMTs—model-based, physics-based, and hybrid. An important aspect in Sections 4.3 and 4.4 is that LMTs were compared in a common environment on the same platform. A summary of the presented results is shown in Table 13.

Table 13. Summary comparing real-time LMTs ©2010 IEEE

LMT	Parameter Sensitivity	Fast Convergence	Convergence to the Optimum	Oscillations	Example
Model-based	High	Yes	Not Guaranteed	No	$\partial P_{loss}(x)/\partial x=0$
Physics-based	None	Not Guaranteed	No	Small or Large	P&O
Hybrid	Medium	Yes	Not Guaranteed	Small	RCC

CHAPTER 5

RELIABILITY MODELING OF INDUCTION MOTOR DRIVE SYSTEMS

5.1 Drive System Operational Considerations for Reliability Assessment

Most LMTs can be added to any induction motor drive with no or minor modification.[5] This can be achieved by programming the LMT algorithm into the control processor or adding a simple analog circuit, e.g., the RCC circuit in the MPPT application shown in [71]. The control variable utilized by the LMT is usually a control input to the motor drive, such as V/f, λ_{dr}, ω_{sl}, etc., and this could affect the drive operation in different ways. Examples were given in Sections 1.1 and 2.2.2 where flux reduction under high torques could significantly alter the drive system operation. In the presence of faults, this altered operation could be catastrophic, especially in applications involving critical safety considerations. Therefore, it is important to study, model, and analyze drive system reliability under LMTs. There exists no systematic procedure to undergo this analysis whether the drive system utilizes an LMT or not. This chapter presents a systematic procedure to find an overall expected MTTF of the drive system under an LMT using Markov reliability models, and proposes a safe-mode backup scheme.

While the modeling procedure is essential, it is important to emphasize the concepts of system *survival* and *failure*. In general a system survives when it is still able to maintain its desired function and fails otherwise. The application usually sets the desired function and therefore any reliability model should be modified accordingly. Therefore, a drive system does not necessarily fail when an essential subsystem completely malfunctions; it could fail while the system is still running but unsatisfactorily. An example best describes the effect of the application or load on the concepts of survival and failure where the same fault could lead to

[5] Much of the results presented in this chapter have been published in [171] or submitted for publication in [9].

system failure in one case but not the other. For example, an EV is desired to maintain the speed and torque within a limited bound around the command to prevent catastrophic acceleration and deceleration. An HEV electrical system should be maintained within tight current and voltage limits to prevent electric hazards. On the other hand, speed and torque bounds are loose for applications such as HVAC and irrigation, but extremes such as loss of cold air or irrigation are undesired. In these two scenarios, the impact of the faults could be different and will affect the overall reliability. If a fault causes the system to run at 50% of the desired speed, an HEV could abruptly decelerate and cause accidents while the pump would still run but at lower capacity. Thus, the load, environment, safety, and other operational considerations should be addressed when modeling the reliability of a drive system. Therefore, the resulting model will differ from one application to the next, and the criteria for survival and failure should be carefully considered.

5.2 Reliability Theory Preliminaries

Markov modeling is used here to evaluate the reliability function and MTTF of an IFOC induction motor drive system. To establish a Markov model, the system response is evaluated under different faults and the system states are determined. The effect of LMTs is addressed by varying λ_{dr}. This variation is studied as fault coverage—the probability of system survival given a fault. In the system presented here, this probability is determined for a sweep over a λ_{dr} range. Before building the Markov model for this specific drive system, preliminaries of reliability evaluation are presented.

5.2.1 Example of a Markov Model and State Diagram

Given a stochastic system, the Markov property can be defined as the dependence of the current state on the previous state. For a random variable X, this can be expressed as $\Pr\{X_t=K_m \mid X_{t-1}=K_{m-1}, X_{t-2}=K_{m-2},\ldots, X_0=K_o\} = \Pr\{X_t=K_m \mid X_{t-1}=K_{m-1}\}$, where X_i is the random variable for time instant i, and Ks are different values of X [74]. A Markov process satisfies a Markov property. In reliability modeling, Markov processes are used to model the system transition from one state to another due to fault occurrence or recovery where only the current state affects the transition to a future state. A Markov process can thus be modeled as a state diagram with failure and recovery rates between states. An example is shown in Fig. 45 where λ_1, λ_2 are failure rates and μ_1, μ_2 are recovery rates.

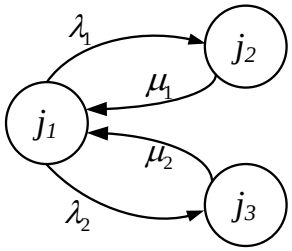

Fig. 45. Example of a state diagram

The state-transition matrix $\mathbf{\Phi}$ can be constructed given a state diagram. For the diagram shown in Fig. 45, $\mathbf{\Phi}$ can be written as

$$\mathbf{\Phi}=\begin{bmatrix} -\lambda_1-\lambda_2 & \lambda_1 & \lambda_2 \\ \mu_1 & -\mu_1 & 0 \\ \mu_2 & 0 & -\mu_2 \end{bmatrix}.$$

Finding the state-transition matrix is a fundamental step in Markov reliability modeling and is essential for the evaluation of the reliability function and MTTF, as will be seen in Section 5.2.3.

5.2.2 Important Reliability Concepts

The reliability or survivor function $R(t)$, MTTF, and fault coverage are three important reliability measures. $R(t)$ is the probability that a component or system is still functional at time t [74]. This can be modeled as $R(t)=\Pr\{X_T > t\}$ where X_T is a random variable that represents the system time to failure. When $R(t)$ is found, the MTTF is defined as

$$\text{MTTF} = \int_0^\infty R(\tau)d\tau \,. \tag{45}$$

The exponential form $R(t)=e^{-\lambda t}$ is a widely used form of $R(t)$, where λ is a fixed failure rate. This means that as the component or system ages, $R(t) \to 0$. Markov reliability models usually use this exponential $R(t)$, as it simplifies building the state-transition matrix and reliability modeling and analysis. This leads to a simple MTTF=$1/\lambda$. Components of series-parallel combinations do not necessarily have an overall equivalent exponential distribution. More detail about such systems is available in [74].

Fault coverage addresses the system ability to maintain desired operation after a fault occurs. The uncertainty of whether the system will survive or fail can be modeled as the probability of survival after a fault: C = Pr {system recovers | fault occurs} [170]. This concept augments different system fault responses into the system reliability model. An example is shown in Fig. 46. The fault coverage C means that the system will transition from state j_1 to state j_2 for C% of the cases when a fault occurs, and for (1-C)% from state j_1 to state j_3, where $0 \le C \le 1$. Fault coverage is usually studied by assessing system response to a fault under different operating conditions. This can be achieved by varying the system inputs over a range and checking the effect of the fault for every input.

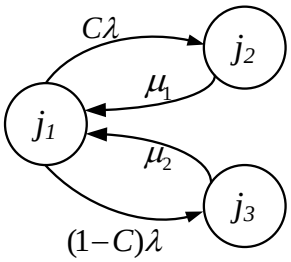

Fig. 46. Example of a state diagram ©2010 IEEE

5.2.3 Transition Probability

The transition probabilities from one state to another must be found in order to determine $R(t)$. They are based on the state diagram which identifies the states and their interconnection. P_{ij} is the transition probability from state i to state j and is time dependent; e.g., the probability of transitioning from the initial state to a failure state increases with time. An example of transition probabilities is shown in Fig. 47 where a transition to the right is shown but arrows going both ways are possible.

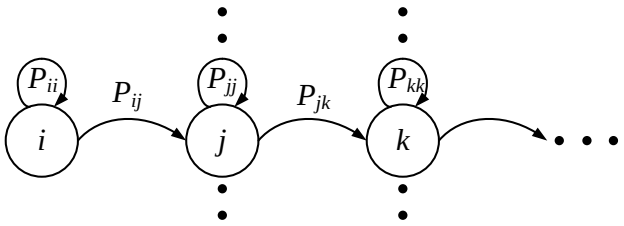

Fig. 47. Markov process ©2010 IEEE

Transitions between different states can then be modeled as a probability matrix **P** which is usually sparse because not all states are interconnected. For M+1 states, **P** can be written as

$$\mathbf{P}(t)=\begin{bmatrix} P_{00}(t) & P_{01}(t) & . & . & . & P_{0M}(t) \\ P_{10}(t) & P_{11}(t) & . & . & . & P_{1M}(t) \\ . & . & . & & & . \\ . & . & & . & & . \\ . & . & & & . & . \\ P_{M0}(t) & P_{M1}(t) & . & . & . & P_{MM}(t) \end{bmatrix}.$$

Different transition probabilities can also be denoted as a row vector to simplify the notation. For K_p states, every state is given a number and the **P** would be

$$\mathbf{P}(t)=\begin{bmatrix} P_0(t) & P_1(t) & . & . & . & P_{K_p}(t) \end{bmatrix}.$$

In a state transition diagram or Markov model, there are *absorbing* nodes and *non-absorbing* nodes. The latter are usually states where the system fails and can no longer function appropriately. If recovery is possible, as shown in Fig. 45, absorbing nodes change to non-absorbing.

5.2.4 Chapman-Kolmogorov Equations

Chapman-Kolmogorov equations describe the probability dynamics in a Markov model or state diagram. The probability rate of change is dependent on **Φ** where the probability dynamics are given by

$$\dot{\mathbf{P}}^T(t)=\frac{d\mathbf{P}^T(t)}{dt}=\mathbf{\Phi}^T\mathbf{P}^T(t) \tag{46}$$

whose derivation is given in [74]. The solution of (46) is straightforward but might require a computational tool for large **Φ**. This solution is given by

$$\mathbf{P}^T(t)=e^{\mathbf{\Phi}^T t}\mathbf{P}^T(0). \tag{47}$$

The initial condition $\mathbf{P}^T(0)$ is a zero vector except for the first element corresponding to the initial state $P_0(0)=1$. Once the probabilities are found, system reliability at any time t can be found as

$$R(t)=\sum_{i=0}^{K} P_i(t) \ , \tag{48}$$

where $P_i(t)$ is the element of index i in $\mathbf{P}$. Thus, finding $\mathbf{\Phi}$ and $\mathbf{P}$ is fundamental to evaluate $R(t)$ and the MTTF.

5.3 Modeling Procedure

The reliability modeling procedure can be summarized as follows:

1. Identify, model, and assess the failure rates of possible faults.
2. Set desired system performance requirements.
3. Inject faults and assess system performance.
4. Identify system states and build Markov model or state diagram.
5. Assign failure and recovery rates to all branches in the diagram.
6. Build state-transition matrix and eliminate rows and columns of absorbing states.
7. Solve (47) to find the probabilities.
8. Solve (48) to find $R(t)$.
9. Solve (45) to find the MTTF.

5.3.1 Fault Modes, Models, and Failure Rates

The major components of the drive system under study, shown in Fig. 30, are the machine, power electronic inverter, current sensors, and speed encoder. The IFOC control algorithm is embedded on a reliable DSP that does not involve high power or mechanical

movement—it is considered fault-free physically. Short connections are used with circuit breaker protection and are also assumed to be fault-free. Components in the drive system have different fault modes and failure rates. The system-level fault modeling approach is convenient for rapid fault impact assessment and reliability evaluation [171] compared to detailed low-level models. Fault modes are usually identified from experience and published literature. For example, current sensors usually have interface circuitry for DSP compatibility by applying proper gains, but if a wrong gain is introduced, it could be considered as a high-level fault.

Faults can be lumped into three main categories: machine, power electronics, and sensors (including current sensors and speed encoders). Each category has basic fault modes identified in the literature [171] and explained here. Among the most common induction machine faults are phase-to-phase faults and broken rotor bar faults [172]. The former are caused by insulation damage between windings of two or more phases due to higher currents or overheating caused by a supply surge or other system faults. The latter are mainly a result of stresses. Power electronics faults include an open circuit (OC) in a phase, and a short circuit (SC) between inverter switch and ground or the dc bus [84, 96, 173]. These faults are usually caused by current or voltage overshoots or overloaded operation of the inverter semiconductors. Under high levels or overshoots in currents or voltages, the junction temperature of the switch or diode exceeds the maximum allowable limits which are usually 150 ^{o}C for silicon devices, and 150–200 ^{o}C or more for SiC and newer technologies. Appropriate thermal management designs, discussed in Chapter 6, are therefore essential for fault prevention in semiconductors such as IGBT-diode pairs in motor drive systems. Sensor faults usually disturb the sensor output by causing improper bias, gain, noise, or total omission of the signal [174]. These faults could physically occur in the sensors, e.g., broken current sensor, or in the interface circuit between the sensor and controller.

All faults studied here and in [9, 171] are shown with their acronyms in Table 14. Circuit-level machine protection, power electronics drivers and protection, and sensor interface circuitry are not explicitly addressed but their effects can be modeled similarly. As faults in each inverter phase or current sensor would lead to similar effects in the system response, it is sufficient to study those in one phase. Note that redundancy is not considered in Fig. 30.

Table 14. Fault modes in the drive system under study ©2010 IEEE

	Speed encoder	Current sensor	Inverter switch	Machine
Fault Types	Omission (SEO)	Omission (CSO)	OC	Phase-to-phase fault (PP)
	Gain (SEG)	Gain (CSG)	SC to ground (SCG)	Broken rotor bar (BR)
	Constant (SEC)	Bias (CSB)	SC to dc bus (SCDC)	
		Constant (CSC)		

Faults have two different models—signal and circuit-based. Signal models are used for sensor faults where the sensor signal is altered by gain, bias, omission, or constant value. This model is used in [9, 171, 174] and is flexible for time-domain simulations and experiments. The signal fault model used here is shown in Fig. 48. While the gain and bias are straightforward, omission is modeled as a zero signal. This is logical for digital encoders and ground short circuits of current sensor interface circuitry. Other faults, e.g., a short circuit of the sensor output to a dc voltage, can be modeled as constant. In that case, the sensor is stuck at a value which is modeled as a saturation port whose upper and lower bounds are the constant value, as shown in Fig. 48.

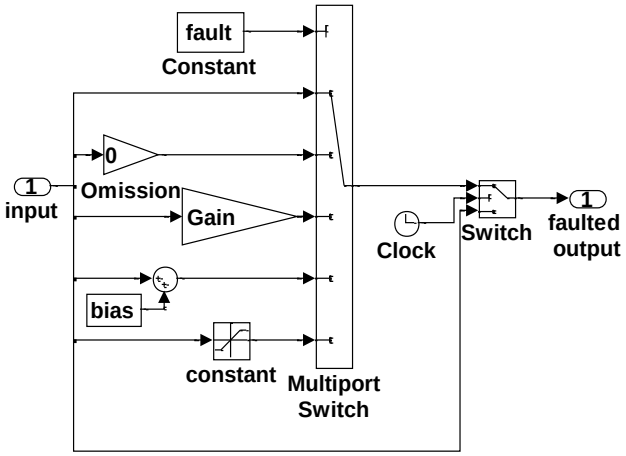

Fig. 48. Signal fault model ©2010 IEEE

The actual sensor signal and different faults can be selected, one at a time, using the multiport switch. The gain, bias, and constant values are set using a mask of the subsystem containing the fault model in Simulink. For simulation, the time at which the fault occurs can be selected using a switch at the output. Simulation time in the clock block is used as the reference, but in experiments, the clock is replaced by a command button linked to the experimental GUI. Circuit-based fault models are used for power electronics and machine faults where they are based on physical characteristics and dynamic changes in electrical quantities such as voltages, currents, resistance. Contrary to signal fault models, simulation and experimental faults could differ. For example, an OC is modeled as an actual switch that is open on the main phase, but could cause a singularity in the simulation model solution and therefore should be avoided; possible solutions include adding a large snubber resistor across the open-circuit switch, or keeping both inverter switches open in that phase. Among the machine and power electronics faults, the BR fault is the most challenging to model. The equivalent R_r should be increased under the BR fault even if the induction machine rotor is squirrel cage. Thus, a wound-rotor machine model is used with shorted windings and equivalent R_r; when the BR fault occurs, the value of R_r is changed. Table 15 shows circuit-based fault models in simulations. Most

experimental electrical faults are challenging or dangerous to mimic as they are either irreversible or catastrophic; thus simulations are used for these (except for the OC fault) after validating the overall simulation model.

Table 15. Simulation circuit-based fault models for machine and power electronics

Fault	Simulation Model
OC	Both switches of that phase are open.
SCG	Switch is turned on between the motor phase and ground.
SCDC	Switch is turned on between the motor phase and dc bus.
PP	Switch is turned on between two motor phases.
BR	Rotor resistance increases.

Every fault has a failure rate which is usually estimated from standards or literature. Numerical failure rate values give only an idea of expected system reliability and MTTF. This reliability approximation could have positive aspects; e.g., failure rates in [175] are generally considered pessimistic and the resulting MTTF from using these numbers leads to conservative designs. Failure rate sources include the military handbook [175] and IEEE Standard 500 which is obsolete but includes useful information [176]. A better reliability modeling practice is to formulate $\mathbf{\Phi}$, $\mathbf{P}$, and $R(t)$ symbolically and then use numerical failure rate values for assessment. The failure rates of the faults shown in Table 14 are extracted from [85, 106, 175-177], and shown in Table 16.

Table 16. Failure rates extracted from the literature for the faults shown in Table 14 ©2010 IEEE

Failure rate	Failures/hour	Failure rate	Failures/hour
λ_{SEO}	7.4×10^{-7}	λ_{CSC}	1×10^{-7}
λ_{SEG}	1.9×10^{-7}	λ_{OC}	5×10^{-7}
λ_{SEC}	1.9×10^{-7}	λ_{SCG}	5×10^{-7}
λ_{CSO}	1×10^{-7}	λ_{SCDC}	5×10^{-7}
λ_{CSG}	1×10^{-7}	λ_{PP}	3.2×10^{-6}
λ_{CSB}	1×10^{-7}	λ_{BR}	3.2×10^{-6}

5.3.2 Performance Requirements and Fault Impact Assessment

Desired performance should be defined based on important or critical system measures in order to assess the system status after every fault. Performance can vary for the same system, e.g., motor drive, based on the application. Among the most common performance notions is that the system is performing its function, e.g., cooling, pumping, or manufacturing. The desired performance presented in [9, 171] is based on an HEV or EV avoiding any collision after 250 ms from the fault occurrence while maintaining speed within a desired range and currents within tolerance limits. The fault impact on system performance is assessed to check whether or not it meets the desired performance requirements. It is hard to visualize performance requirements and the concepts of failure and survival for more than two or three requirements. So, let there be two performance requirements, pm_1 and pm_2. The desired limits are bounded by A_1 in Fig. 49. Nominal operating conditions are within A_1. If the system performance is bounded by A_2 after a fault, then it survived the fault as shown in Fig. 49 (a); otherwise, it failed as in Fig. 49 (b). Note that the requirements may be modeled with ellipsoids [178]. Performance measures and requirements for driving conveyors are presented in [179].

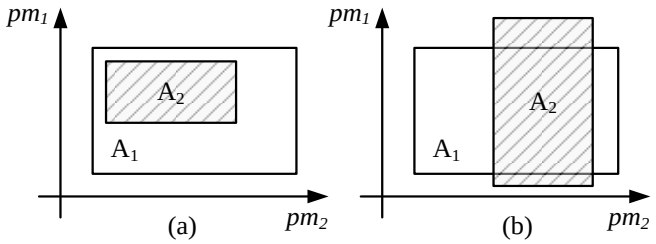

Fig. 49. (a) System survival, (b) system failure ©2010 IEEE

In the motor drive application studied here, the performance bounds are set for speed, current, and settling time of both. It is important to maintain the speed within a desired range and avoid dangerous acceleration or deceleration after a fault. Thus, it is desired to bound the speed around

the speed command. Over-currents or long-duration current overshoots could also cause a safety hazard and jeopardize system operation. They could cause the inverter, connectors, and other subsystems to overheat and fail. Over-voltages also cause over-currents, so the over-current performance requirement addresses both. While speed and current can overshoot after a fault, the system can return to an acceptable state within a settling time, defined as the time needed for a signal to recover within performance bounds. An example performance diagram is shown in Fig. 50 for a dc signal such as speed measurement. For ac signals such as currents, the current peak should return to the desired bounds within a certain settling time. The performance requirements used for the motor drive system under study are shown in Table 17 and reflect typical desired conditions.

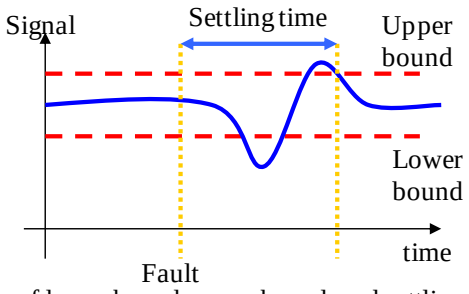

Fig. 50. Example of lower bound, upper bound, and settling time of a signal

Table 17. Performance bounds for the motor drive under study ©2010 IEEE

Speed	Command speed ± 50 rpm
Current	-10 A ≤ Peak ≤ 10 A
Settling time	≤ 250 ms

5.3.3 Building a Markov Model

Once the performance requirements and faults are defined, a Markov model is built after fault injection and system performance assessment. The Markov model is a state diagram that reflects the system state after every fault. Recovery is not considered here but could be easily added to the model. In systems with no recovery, failure is permanent and the failure state is

absorbing. System survival after each fault is modeled as a separate state because the response differs for various faults. Once a fault is injected, another fault could occur and could be related to the first or independent. An example of dependent faults is an OC in an inverter phase which could cause over-current in the other two phases. Then a PP fault would occur in the machine. Two cascaded faults in the same component or subsystem are not considered, as this probability is low. Fault coverage is added to the Markov model, as shown in Fig. 46. Under an LMT applied to an IFOC induction motor drive, the control variable λ_{dr} is varied over a range, and system states are determined for all faults and fault-cascading combinations. Several discrete steps of λ_{dr} are used in the fault coverage study. Having a large number of steps requires longer simulation times to finalize the reliability model. The total number of system states grows exponentially with a large number of faulty components and faults per component. This requires significant computational effort and simulation time.

5.4 Drive System Reliability under Loss Minimization

5.4.1 Model Validation

The drive simulation model was developed in Simulink using SimPowerSystems blocks as shown in Fig. 51 to apply the faults described in Section 5.3.1. The purpose is to avoid catastrophic failures in the experimental setup and create a simple fault injection and impact assessment scheme. Severe faults could cause the experimental setup to fail or stall due to protection circuitry; either will impact the reliability analysis flow and results.

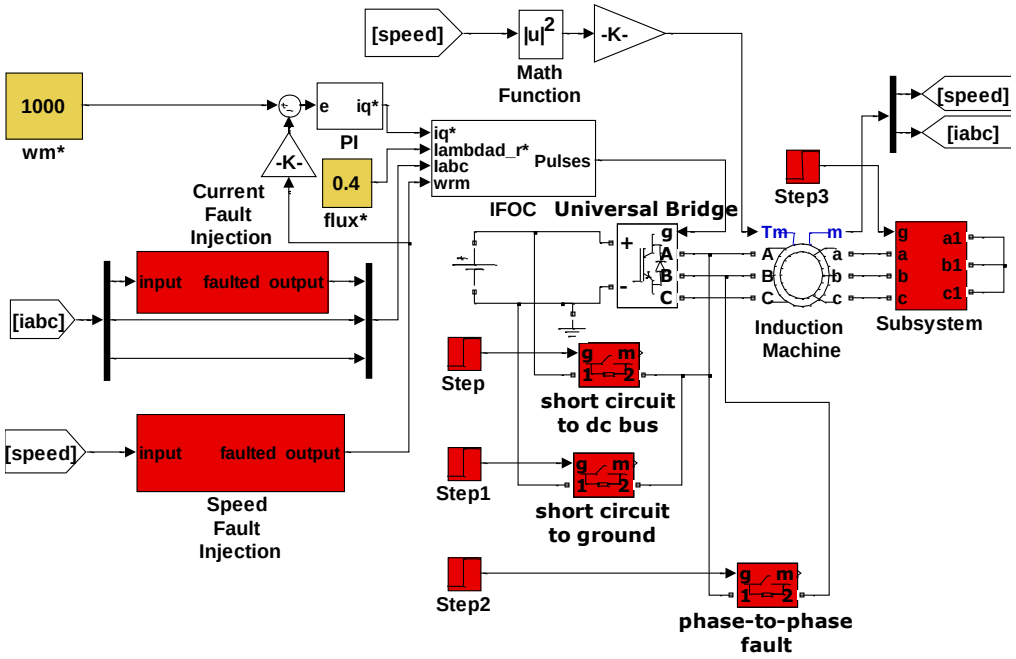

Fig. 51. Simulation model in Simulink ©2010 IEEE

The blocks highlighted in red in Fig. 51 show the fault injection locations. The *Speed Fault Injection* and *Current Fault Injection* blocks have the structure shown in Fig. 48. The SCDC fault is triggered using the *Step* block between phase *a* and the dc bus. The SCG fault is triggered using *Step*1 between phase *a* and ground. The PP fault is triggered using *Step*2 between phases *a* and *b*. The SCDC, SCG, and PP faults could also occur on any other phases and the results would be similar due to machine symmetry. *Step*3 triggers the BR fault where the rotor resistance is increased from R_r to $1.1\times R_r$. The 1.1 factor can be changed as desired depending on the actual number of intact and broken rotor bars. Note that the effect of inductance change is assumed to be negligible [172]. The load shown in Fig. 51 is quadratic as shown in (42) where k_{load} =1.816×10^{-4}. While this models a propulsion load or fan, it could also be used for certain operating points in a vehicle motor drive. The λ_{dr} command is shown as *flux** for the case when λ_{dr}=0.4V·s; it is varied for the fault coverage study.

Before proceeding with the reliability modeling based on the simulation model shown in

Fig. 51, the model was validated against the experimental setup described in Appendix C. A similar load characteristic was used and the system was tested under faults shown to survive or cause mild failures in simulations. Results that validate the model are shown in Figs. 52–57 for SEO, CSC, and OC. There are three main differences between the experimental setup and the simulation model: (1) The experimental setup includes an extra torque control loop to avoid undesired acceleration or mechanical breakdown of the machine or dynamometer. (2) The setup includes protection circuitry which is activated under gate, over-voltage, and over-current faults. This circuitry does not interfere with the results shown here, but it could affect the system response under other faults. (3) The hysteresis band used in experiments is larger than that in simulations due to the limited switching frequency on the DSP and experimental inverter. This leads to higher current peaks in the experiments.

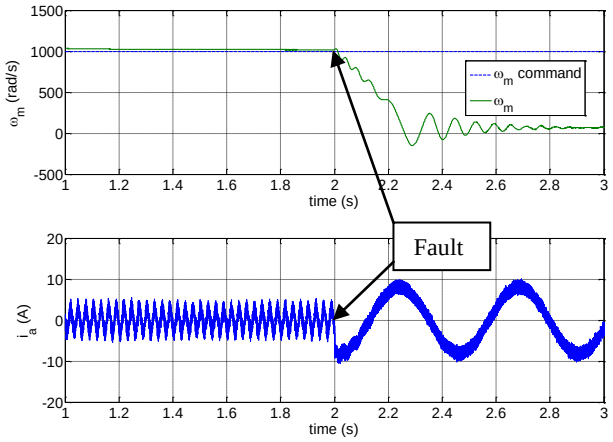

Fig. 52. SEO simulation results: Actual and command speed (500 rpm/div, top), current in phase *a* (10A/div, bottom) ©2010 IEEE

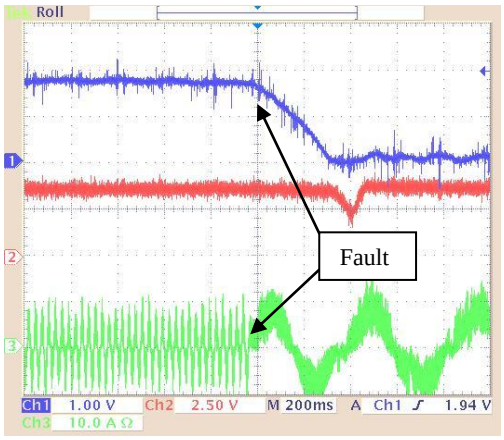

Fig. 53. SEO experimental results: Speed (500 rpm/div, top), torque (2 N·m/div, middle) current in phase *a* (10A/div, bottom) ©2010 IEEE

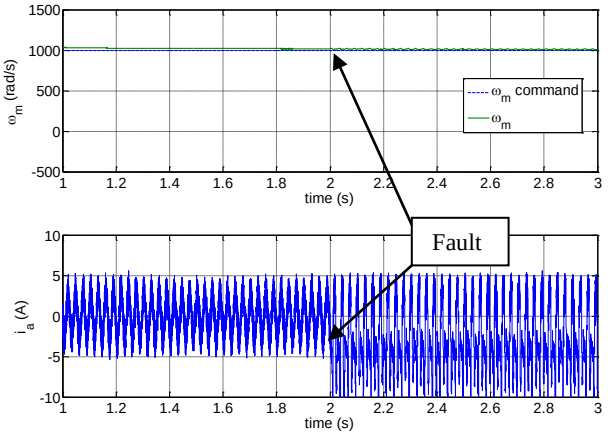

Fig. 54. CSC simulation results: Actual and command speed (500 rpm/div, top), current in phase *a* (5A/div, bottom) ©2010 IEEE

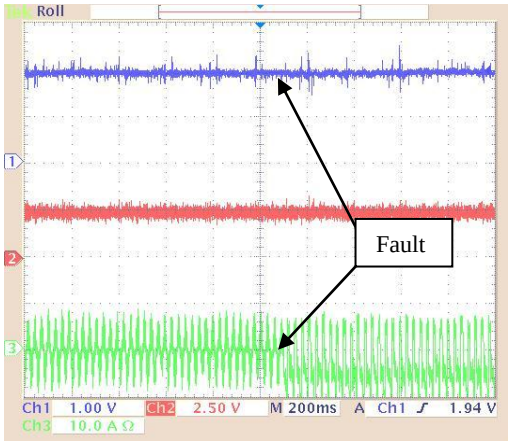

Fig. 55. CSC experimental results: Speed (500 rpm/div, top), torque (2 N·m/div, middle) current in phase *a* (10A/div, bottom) ©2010 IEEE

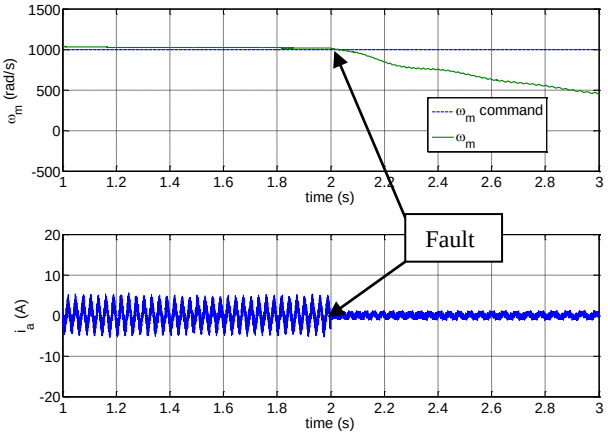

Fig. 56. OC Simulation results Actual and command speed (500 rpm/div, top), current in phase *a* (10A/div, bottom) ©2010 IEEE

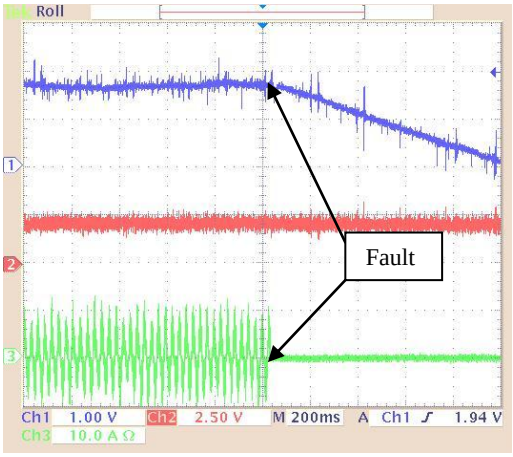

Fig. 57. OC experimental results: Speed (500 rpm/div, top), torque (2 N·m/div, middle) current in phase *a* (10A/div, bottom) ©2010 IEEE

The results in Figs. 52-57 for ω_m=1000 rpm and λ_{dr}=0.4 V·s show that, in general, the simulation model matches the experimental setup except for some minor discrepancies, e.g., the current peaks explained earlier. Figs. 52 and 53 show that the system fails after the SEO fault—the speed drops to zero and does not comply with the performance requirements. The system also fails after the CSC fault, as shown in Figures 54 and 55, because the current peaks exceed the acceptable performance bound of 10 A. Another failure is demonstrated in Figs. 56 and 57 due to the OC fault where the speed decreases to zero. In Fig. 56, the phase *a* current is not exactly zero due to the snubber resistance across the OC switch, required to avoid a numerical simulation error. But, the current and speed waveforms and responses match and show that the model generally behaves as expected. Also, it is important that the response of both experiments and simulations under faults match almost perfectly because the faulty states are the decisive factor in determining the system states and constructing the Markov model.

5.4.2 Reliability Model

Reliability analysis can proceed with fault injection and impact assessment in the simulation model. Two fault levels are injected with the following considerations: (1) If the first fault occurs in one component, the second fault will occur in another one. The probability of having two faults occur consequently in the same component is set to be very low. (2) Any third fault is treated as causing the system to fail. Even though this assignment introduces truncation errors to the system, the probability that the system survives three consecutive faults is relatively small and does not impact the analysis. Also, the final absorbing state (third-level in this case) is essential for constructing $\mathbf{\Phi}$ and solving (47). (3) Faults are injected after the system reaches its steady state to avoid amplifying any transient. (4) Once a first-level fault causes the system to

fail, the system state is absorbing and no second-level fault is injected. (5) The values used for the SEG, SEC, CSG, CSB, and CSC are shown in Table 18. These values are used to illustrate the fault effect in Sections 5.4 and 5.5, but can be changed as desired.

Table 18. Values used for SEG, SEC, CSG, CSC, and CSB ©2010 IEEE

Fault Type	Speed Encoder	Current Sensor
Gain	1.5	1.5
Constant	900rpm	3A
Bias	N/A	+1A

The first fault level was injected and impact and performance requirements were checked. Fault coverage for different λ_{dr} commands between 0.2 and 0.6 V·s was studied in 0.1 V·s steps. The only fault for which the λ_{dr} variation has any effect is CSO where the coverage is c_1=4/5. The results for the first fault are shown in Table 19 where *S* and *F* stand for survival and failure, respectively. Notice that 7 of 12 tested faults were survived as shown in Table 19. These seven faults are then followed with a second level of faults. The results are shown in Table 20.

Table 19. Results for the first fault level ©2010 IEEE

Fault 1	Status	Fault 1	Status
SEO	*F*	CSC	*F*
SEG	*F*	SCDC	*S*
SEC	*F*	SCG	*S*
CSO	*S*, c_1=4/5	OC	*F*
CSG	*S*	PP	*S*
CSB	*S*	BR	*S*

Table 20. Results for the second fault level ©2010 IEEE

	Fault 1						
Fault 2	CSO	CSG	CSB	SCDC	SCG	PP	BR
SEO	*F*	*F*	*F*	*F*	*F*	*F*	*F*
SEG	*F*	*F*	*F*	*F*	*F*	*F*	*F*
SEC	*F*	*S*	*F*	*F*	*F*	*F*	*F*
CSO	N/A	N/A	N/A	*S*, c_5=4/5	*S*, c_7=4/5	*S*	*S*, c_9=2/5
CSG	N/A	N/A	N/A	*S*	*S*	*S*	*S*
CSB	N/A	N/A	N/A	*S*	*S*	*S*	*S*
CSC	N/A	N/A	N/A	*S*	*F*	*S*, c_8=3/5	*F*
SCDC	*S*, c_3=1/2	*S*	*S*	N/A	N/A	*S*	*S*
SCG	*S*, c_2=3/4	*S*	*S*	N/A	N/A	*S*	*S*
OC	*F*	*F*	*F*	N/A	N/A	*F*	*F*
PP	*S*, c_3=1/2	*S*	*S*	*S*, c_4=2/5	*S*, c_6=2/5	N/A	N/A
BR	*S*, c_3=1/2	*S*	*S*	*S*	*S*	N/A	N/A

The N/A cells in Table 20 correspond to second faults that cannot occur after the first fault in the same component, and c_2– c_9 are coverage terms. Notice that even after two faults, several states survive. The third-level absorbing failure state is a necessity to avoid exponential growth of the number of states. The total number of states from Tables 19 and 20 is 52 divided as follows: zero-level—one initial state (one state total), first level—seven survival states and one failure state which includes all five failures (eight states total), second level—35 survival states and seven failure states, each corresponding to system failure after the first and second faults occur (42 states total), third level: one failure state (one state total). Thus, the dimensions of the sparse $\mathbf{\Phi}$ are 52×52 and the Markov model is shown in Fig. 73 in Appendix D. Absorbing failure states should be eliminated to solve equation (47). As there is a total of nine failure states, the new dimensions of $\mathbf{\Phi}$ are 42×42 and the non-zero elements of $\mathbf{\Phi}$ are shown in Table 28 in Appendix D.

With $\mathbf{\Phi}$ available, equation (47) is solved for $\mathbf{P}^T(t)$, and $R(t)$ is found using equation (48). The Mathematica script used to find $\mathbf{P}^T(t)$ and $R(t)$ is shown in Appendix D. For the failure rates shown in Table 16, $R(t)$ is

$$\begin{aligned} R(t) = {} & 2.585e^{-9.65\times10^{-6}t} - 1.052e^{-9.25\times10^{-6}t} - 1.0167e^{-8.15\times10^{-6}t} \\ & + 0.008042e^{-7.9\times10^{-6}t} + 0.522e^{-7.75\times10^{-6}t} - 1.4167e^{-3.25\times10^{-6}t} \\ & + 0.742e^{-2.85\times10^{-6}t} + 0.629e^{-1.75\times10^{-6}t} + 0.7(-e^{-9.65\times10^{-6}t} + e^{-9.25\times10^{-6}t}) \cdot \\ & + \frac{2}{3}(-e^{-9.65\times10^{-6}t} + e^{-8.15\times10^{-6}t}) - e^{-9.65\times10^{-6}t} + e^{-3.25\times10^{-6}t} \end{aligned} \tag{49}$$

Applying equation (45) to $R(t)$ shown in (49) yields an MTTF = 57.2 years = 501×10^3 hours. This MTTF is very impressive for induction motor drive applications, even though most of the failure rates from [175] and other sources are conservative. This result shows that augmenting

more motor drives in transportation, propulsion, and industrial applications is a reliable strategy for current and future applications.

The highest failure rate in Table 16 is associated with the speed encoder. To test system impacts of this sensor, all failure rates of other faults are set to be negligible, and the analysis is rechecked. The same procedure shown earlier is followed and a reliability function $R_{se}(t)$ is generated. The plots of $R(t)$ and $R_{se}(t)$ are shown in Fig. 58. The MTTF calculated from $R_{se}(t)$ is 742×10^3 hours. As expected, this MTTF is greater than 501×10^3 hours because not all faults are considered. It shows that the encoder accounts for 68% of the overall reliability impact. While this result justifies further research on speed sensorless control, it also suggests that other faults should not be ignored and appropriate redundancy, fault detection, and fault isolation should be implemented.

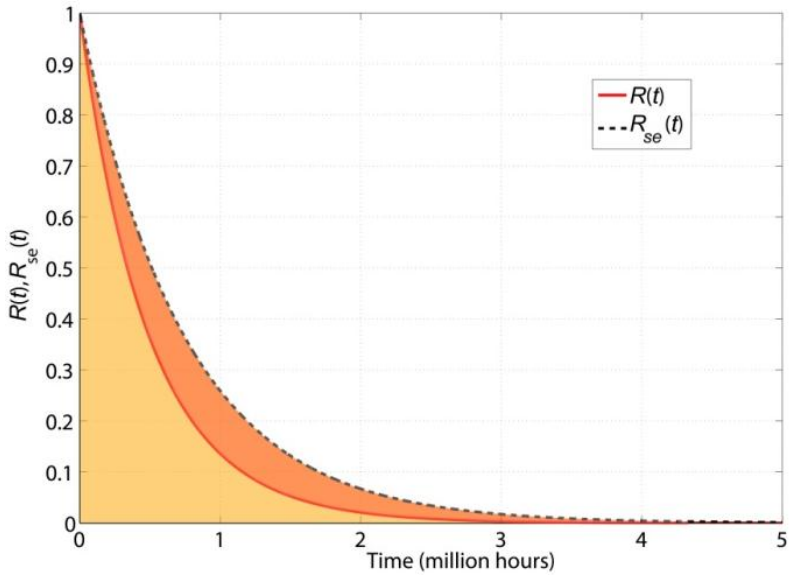

Fig. 58. System reliability functions under all faults and only speed encoder faults ©2010 IEEE

Table 16 shows that failure rates are either on the order of 10^{-6} or 10^{-7} failures/hour. These two orders can be modeled as λ_{high} and λ_{low}. λ_{high} is 3.2×10^{-6} failures/hour for PP and BR, and λ_{low}

is found to be 3×10^{-7} failures/hour by averaging all other failure rates. The simplified $R_s(t)$ from the new $\mathbf{\Phi}$ is

$$\begin{aligned} R_s(t) = {} & 0.277e^{(-9.4\times10^{-6}t)} - 0.35e^{(-8.5\times10^{-6}t)} - 0.4e^{(-8.2\times10^{-6}t)} \\ & + 0.521e^{(-7.3\times10^{-6}t)} - 0.417e^{(-3\times10^{-6}t)} \\ & + 0.642e^{(-2.1\times10^{-6}t)} + 0.726^{(-1.8\times10^{-6}t)} \end{aligned} ,$$

which almost overlaps with $R(t)$ shown in Fig. 58. The MTTF found from $R_s(t)$ is 581×10^3 hours, less than a 16% difference when using $R(t)$. This result suggests that knowing only the order of failure rates can lead to acceptable reliability modeling and estimates of $R(t)$ and MTTF.

5.5 Safe-Mode Analysis

The results shown in Section 5.4 for speed encoder fault impact suggest that if there is an open-loop control that avoids sensor faults, system reliability can improve. While this is a good intuitive idea, open-loop controls have poor dynamic response compared to IFOC and other closed-loop controls. Thus, even though the effect of sensor faults is eliminated for open-loop controllers, their response under other faults is expected to be worse than closed-loop controllers, especially when the settling time is among the performance requirements. The work presented in [180] follows a procedure similar to that described in Section 5.4, and in [9, 171]. There are two main differences between the simulation models used in [180] and Chapter 5: First, [180] uses a circuit-based machine model shown in Fig. 18 rather than the induction machine block from SimPowerSystems. Second, the controller in [180] uses *dq0* controlled voltage sources rather than a current-source inverter.

The analysis here proceeds with the models presented in [180] as follows. First, the IFOC motor drive system reliability is identified to compare its MTTF to that shown in Section 5.4.2.

Second the IFOC drive reliability is estimated without sensor faults in order to check the effect of sensors on drive system reliability. Third, the constant-V/f open-loop drive reliability is found for machine and power electronics faults where sensor faults have no impact. Finally, a backup safe mode, shown in Fig. 10, is tested and its reliability is estimated. The last step also shows the effect of the switching delay time as the system transitions between both controllers.

A procedure similar to that followed in Section 5.4 is used to estimate the IFOC motor drive reliability shown in Fig. 59, where ω_a is the frequency of an arbitrary reference frame. The terms v_{qs} and v_{ds} are defined in [181] and shown below for convenience.

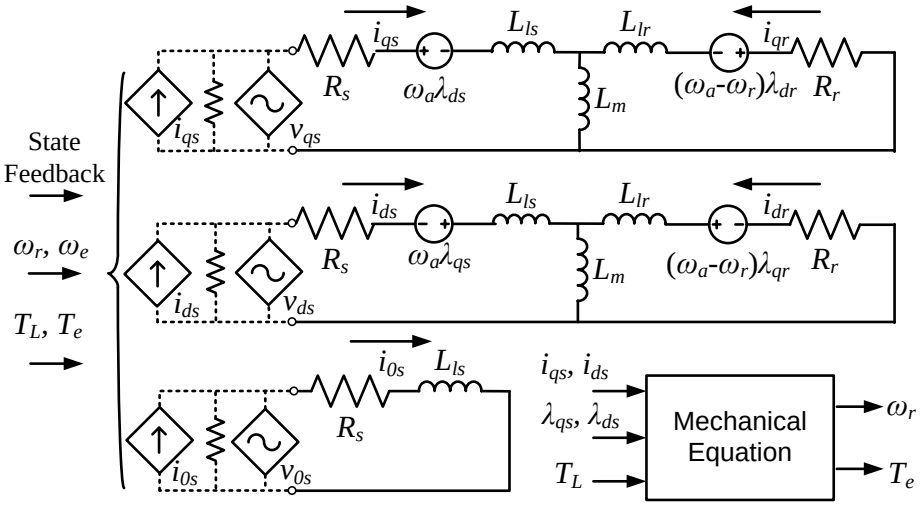

Fig. 59. Circuit-based motor drive model

$$v_{qs} = \sigma_L \left[n_p \omega_r i_{ds} + \frac{R_r}{L_r} L_m i_{ds} \frac{\left(i_{qs}\lambda_{dr} - i_{ds}\lambda_{qr} \right)}{\lambda_{qr}^2 + \lambda_{dr}^2} + \frac{\lambda_{dr}}{\sqrt{\lambda_{qr}^2 + \lambda_{dr}^2}} u_{speed} + \frac{\lambda_{qr}}{\sqrt{\lambda_{qr}^2 + \lambda_{dr}^2}} u_{flux} \right] + \frac{L_m}{L_r} n_p \omega_r \lambda_{dr} \quad (50)$$

$$v_{ds} = \sigma_L \left[-n_p \omega_r i_{qs} - \frac{R_r}{L_r} L_m i_{qs} \frac{\left(i_{qs}\lambda_{dr} - i_{ds}\lambda_{qr} \right)}{\lambda_{qr}^2 + \lambda_{dr}^2} - \frac{\lambda_{qr}}{\sqrt{\lambda_{qr}^2 + \lambda_{dr}^2}} u_{speed} + \frac{\lambda_{dr}}{\sqrt{\lambda_{qr}^2 + \lambda_{dr}^2}} u_{flux} \right] - \frac{L_m}{L_r} n_p \omega_r \lambda_{qr} \quad (51)$$

The resulting MTTF for IFOC in this model is 58.53 years which is only 2.3% longer than that shown in Section 5.4.2. This step verifies that the model in Fig. 59, which is very convenient for simulating switched control systems with the control inputs v_{qs} and v_{ds}, performs as expected. In order to determine the effect of sensor faults on drive reliability under IFOC, sensor faults were eliminated from the analysis and simulations. This step helps identify the ultimate IFOC performance under all faults to achieve the best-case scenario of an ideal safe-mode and mitigate sensor faults. Performing this analysis yields an MTTF of 96.63 years, significantly higher than 58.53 years. This result implies that having an effective open-loop safe-mode that takes over the drive system when a sensor fault occurs will lead to a significant increase in the system's MTTF.

The most common open-loop induction motor controller is constant V/f. An evaluation of its MTTF gives an idea of possible improvement in the combined IFOC-safe-mode drive. As V/f control it is not affected by sensor faults, its MTTF is expected to be higher than IFOC. But its dynamic response is not enhanced by the corrective feedback under machine and power electronics faults as in the IFOC case; thus, its MTTF is expected to be lower than IFOC without sensor faults. Reliability modeling and simulations were performed for the open-loop constant V/f drive, and the MTTF was found to be 65.03 years. As expected, this MTTF falls between that of IFOC and IFOC without sensor faults. The MTTFs are tabulated in Table 21 and $R(t)$ for IFOC and constant V/f are shown in Fig. 60.

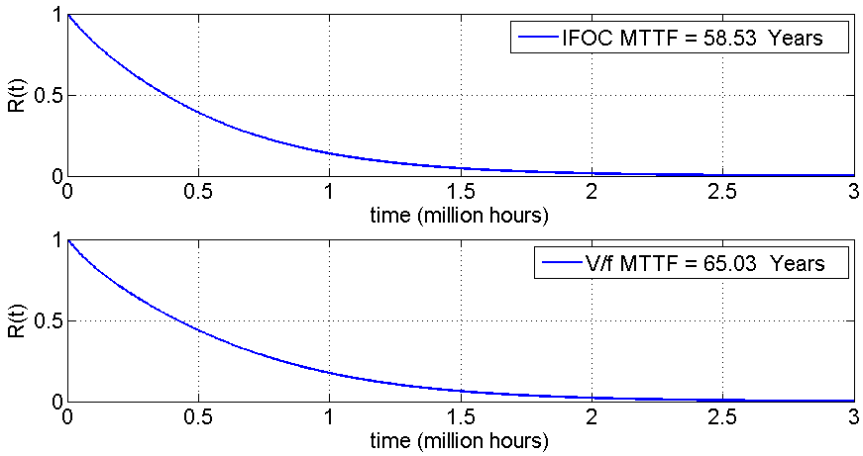

Fig. 60. $R(t)$ of the motor drive system under IFOC and constant V/f

Table 21. MTTF summary

Controller	MTTF (years)
IFOC	58.53
IFOC (no sensor faults)	96.63
Constant V/f	65.03

Reliability analysis of the safe-mode operation shown in Fig. 10 assumes that the decision maker detects sensor faults perfectly. The variable in the safe-mode operation is the time between sensor fault occurrence and switching to the open-loop controller. This time is notated as t_f and it is the only time during which the system operates under a sensor fault. Note that the system will switch to the safe mode whether the sensor fault causes failure or not.

Different values of t_f were tested and the reliability model of the drive system was found. $R(t)$ for different t_f are shown in Fig. 61. As expected, the MTTF increases as t_f is smaller. The results are tabulated in Table 22. These results are expected because with larger t_f, the system would spend more time under the sensor fault before the safe-mode is engaged. During this period, higher overshoots could happen, and longer settling times that do not satisfy the performance requirements might result.

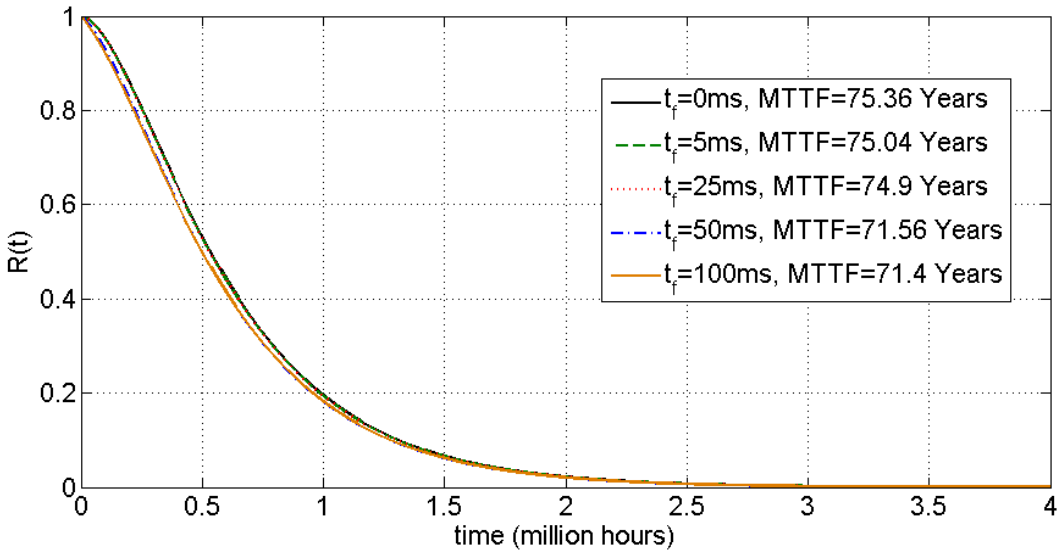

Fig. 61. Effect of t_f on the system MTTF

Table 22. MTTF summary for safe-mode operation for different values of t_f

t_f (ms)	MTTF (years)
0	75.36
5	75.04
25	74.9
50	71.56
100	71.4

The results in Table 22 show that combining IFOC and constant V/f yields MTTFs that are higher than those of either IFOC or V/f. But, even for the ideal case when the system switches to the safe-mode with t_f=0s, the MTTF does not reach that of IFOC without sensor faults. This is due to two main reasons. First, the voltages resulting from IFOC and V/f might have some discrepancy where v_{abc} does not have synchronous or seemless transition when the switching occurs. Thus, it would be worthwhile to study the smooth transition requirements with safe-mode switching. Second, when the system is operating under V/f after a sensor fault and a new fault occurs in the machine or power electronics, V/f would be less reliable due to its dynamic response under these faults. Note that the mathematical derivation of the t_f effect on the system reliability is not straightforward and is not addressed here for several reasons, which

include the use of the nonlinear fifth-order induction machine model, which is hard to fit to available dwell-time analysis and the complexity and nonlinearity of the voltage control equations shown in (50) and (51).

System complexity can be reduced by using a simplified first-order transfer function of the machine, but such an analysis is left for future research. The results shown in this section imply that having an open-loop safe-mode controller in an IFOC drive system yields higher system reliability. These results also lead to a quantitative analysis of the t_f effect which verifies that as t_f increases, the MTTF decreases.

CHAPTER 6

LOSS ESTIMATION IN POWER SEMICONDUCTORS FOR BETTER INVERTERS

6.1 Introduction to Electro-Thermal Design Optimization

Faults addressed in Chapter 5 include those in the machine, power electronics, and sensors.[6] The effect of sensor faults was shown to be reduced in Section 5.5 using an open-loop safe-mode controller. Machine faults can be reduced by appropriately cooling the machine, reducing the electrical and mechanical stresses, using more than three phases, using multiple windings per phase, etc. Semiconductor devices are the remaining components that affect motor drive reliability. As mentioned in Section 5.3.1, power electronics SC and OC faults are among the common faults in motor drive systems. These are usually caused by thermal management problems where their junction temperatures exceed the allowed limit tolerated by semiconductor material and packaging. Switches in motor drive systems with several kW ratings are commonly IGBTs rather than MOSFETs. IGBTs have no inherent body diode, so a diode is always connected in parallel with the IGBT. The operation of an IGBT-based half-bridge inverter is discussed in Section 6.2.1 and can be extended to three-phase inverters, common in induction motor drives. Approximating and analyzing losses in an inverter helps achieve better cooling strategies and thus more reliable operation.

Losses considered in an IGBT are turn-on, turn-off, and conduction losses where the first and second constitute the switching losses. Diode losses are the reverse recovery turn-off switching loss and conduction loss. There is always a trade-off between switching and conduction losses in IGBTs and diodes: for the same period of time, more switching leads to less conduction and vice versa. While switching loss can be evaluated from the voltage-current

[6] Some of the results presented in this chapter were published in [182].

transient in the switching device, conduction loss is the product of the voltage and current across the switch. An example of an IGBT turn-on switching transient is shown in Fig. 62 where V_{off} and V_{on} are the voltages across the IGBT when off and on, respectively; I_{on} is the current passing through the IGBT when on, and t_{on} is the turn-on transient time.

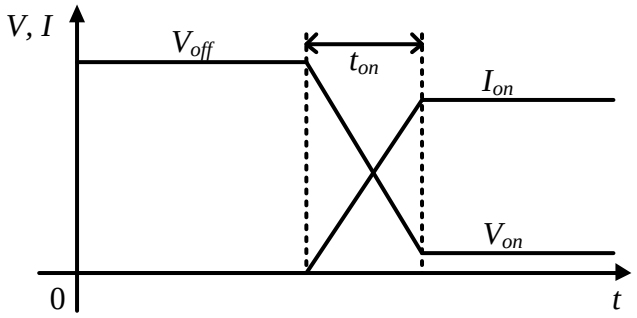

Fig. 62. Turn-on transient of an IGBT

The switching energy depends on the intersection between the voltage and current waveforms and can be found as

$$E_{sw} = \frac{V_{off} I_{on}}{2 s_f} \left(t_{on} + t_{off} \right), \tag{52}$$

where s_f is a switching factor set by the transient shape and t_{off} is the turn-off time. For transients that occur at a rate of r_t per second, the switching loss can be evaluated as $P_{sw}=E_{sw}\times r_t$. If the switching occurs periodically at a switching frequency f_{sw}, then $r_t=f_{sw}$. The conduction period changes for different r_t and the conduction energy (E_{cond}) is

$$E_{cond} = V_{on} I_{on} t_{cond}, \tag{53}$$

where t_{cond} is the conduction time. Figures 63 (a) and (b) show two different switching patterns which would have different total power loss. Switching and conduction are affected by the device physics, the number of switching transients, and the switching and conduction times. Thus, some minimum combination of these losses should exist.

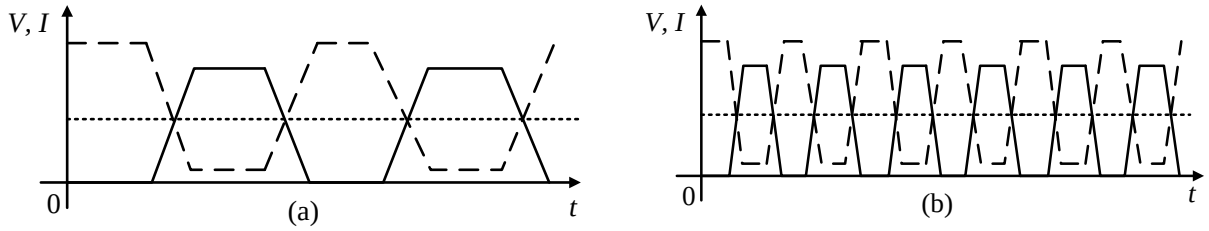

Fig. 63. (a) Longer conduction times and less switching (b) More switching and shorter conduction times

An approach for future optimal electro-thermal designs of power converters is proposed here and is based on power loss estimation. An IGBT-diode loss-estimation tool is presented. As discussed in Section 2.5, loss estimation is an essential step in the electro-thermal design process of power converters. Also, an estimation tool that is model-independent, fast, and experimentally-verified to estimate losses under any switching scheme is desired. Such a tool enables loss estimation and design evaluation for different devices, control methods, and operating points. For example, an IFOC motor drive with a hysteresis-controlled current source inverter has several design variables including the IGBT-diode pair selection, hysteresis band, maximum possible switching frequency, etc. Accurate and fast loss estimation helps identify the optimal power electronics design. The optimization process can also account for the cost of semiconductor devices and thermal management system. Thus, losses and cost of an IFOC motor drive can be evaluated for different combinations of devices, switching patterns, etc., for rapid prototyping. A possible future approach to minimum-loss and cost-effective power electronics designs is to find an empirical formula that relates the cost function, including losses, cost, and other design criteria, to the design variables. This formula can be found from measurements that reflect general characteristics. Curve-fitting could be used for this purpose.

It is important to note that system-level loss minimization is possible by augmenting inverter and machine losses into one cost function. Inverter losses can be modeled using the empirical formula described above and augmented to the loss minimization process. In such a

scenario, an LMT will be extended to a system level. An example is to have both the machine and inverter cost functions with the phase current as the control variable, i.e. stator current in the machine. While P_{loss} is expected to be flat around the minimum-loss point for the machine, losses in the inverter decrease significantly with lower currents and the overlay of both functions is expected to be as shown in Fig. 64. Note that the general curve shapes are intended in Fig. 64 based on results shown in the literature, e.g. [53, 122]. Adding both losses to the cost function will have a positive effect on penalizing higher currents and thus avoiding operating points close to saturation. But, this could drive the minimum-loss point below the current or flux that can support the load and should be carefully considered.

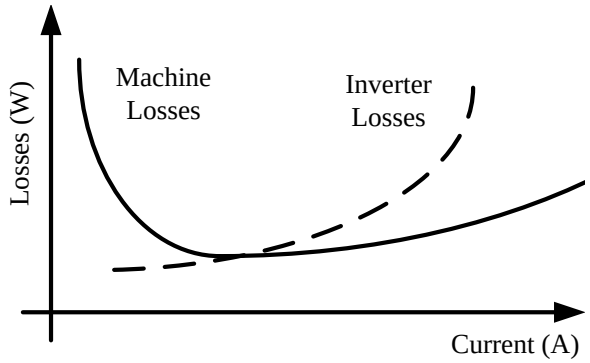

Fig. 64. Machine and inverter losses for system-level loss minimization

6.2 Proposed Loss-Estimation Tool

6.2.1 Overview

The proposed analysis tool analyzes the IGBT and diode states based on the IGBT switching pulse, p, and load current, I_L, both at a time instant and the previous instant. The time step is set by the sampling rate of experimental or simulation data being processed. The tool is independent of IGBT-diode circuit models, detailed knowledge of physical characteristics, thermal measurements, and switching scheme. The relationship of these waveforms is given in

Table 23 for the upper IGBT (*Q*) and diode (*D*) in a half-bridge. The terms *i* and *i*-1 refer to the current and previous samples, respectively. I_L is assumed to be positive when flowing to the load, i.e., when *Q* conducts. *p* is 0 when *Q* is off, and 1 when *Q* is on. The operation can be summarized as follows:

i) If *Q* is off and its gate signal changes from 0 to 1, it turns on and current passes through.

ii) If *Q* is on and its gate signal changes from 1 to 0, it turns off and its current stops flowing.

iii) If the current was flowing and is still flowing in *Q* and *Q* was on and is still on, then it conducts.

iv) If *p* changes from 1 to 0, i.e., the lower IGBT is off and then turns on, the current is flowing in *D* and then *D* turns off.

v) If *p* was 1 and is still 1, i.e., the lower IGBT was off and is still off, the current was flowing and is still flowing in *D*, and it conducts.

Table 23. Operation under different current and pulse conditions

Case	Current Direction	Gate signal of *Q*	Operation
i	$I_L(i) \geq 0$	$p(i\text{-}1)=0$ & $p(i)=1$	*Q* turns on
ii	$I_L(i\text{-}1) \geq 0$	$p(i\text{-}1)=1$ & $p(i)=0$	*Q* turns off
iii	$I_L(i\text{-}1) \geq 0$ & $I_L(i) \geq 0$	$p(i\text{-}1)=1$ & $p(i)=1$	*Q* conducts
iv	$I_L(i\text{-}1) \leq 0$	$p(i\text{-}1)=1$ & $p(i)=0$	*D* turns off
v	$I_L(i\text{-}1) \leq 0$ & $I_L(i) \leq 0$	$p(i\text{-}1)=1$ & $p(i)=1$	*D* conducts

Table 23 does not include open circuits, short circuits, or faulty conditions. Figure 65 shows a summary of the proposed tool where the main steps involve saving the data, setting up the tool to curve-fit the required datasheet curves, and processing the data in software such as MATLAB. Note that only the average V_{dc} is required for curve fitting. This will be explained in Section 6.2.2. Power loss computation, shown as the last step in Fig. 65, is based on incrementing energy losses for the cases in Table 23. Section 6.2.3 explains incrementing energy losses.

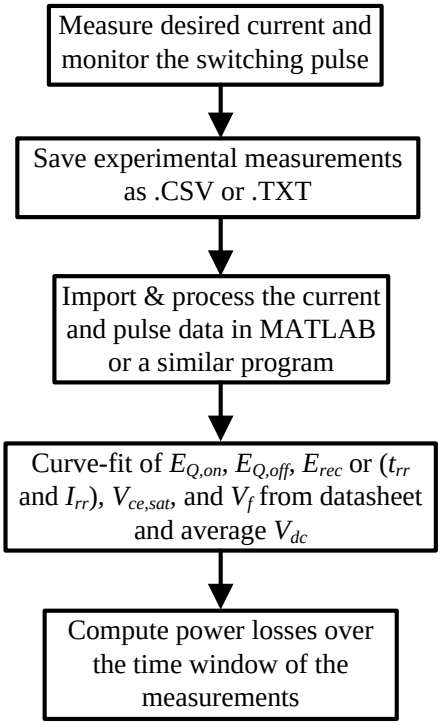

Fig. 65. High-level block diagram of the proposed tool

6.2.2 Curve Fitting

The tool curve-fits $E_{Q,on}$, $E_{Q,off}$, and the diode turn-off energy, E_{rec}, or I_{rr} and t_{rr}, in addition to voltages $V_{ce,sat}$ and V_f . Four or more points given in the datasheet curves are used for curve fitting. When E_{rec} is not given, t_{rr} and I_{rr} curves are used. Curves are fit as second-order polynomials. Minor improvement can be achieved with higher order polynomials or logarithmic functions. The functions are scaled depending on the actual V_{dc}, relative to the voltage in the datasheet.

A simple scheme similar to (13) is followed as the main purpose is to develop a general tool for any switching scheme based on datasheet information. Such a scheme provides satisfactory results in [123]. The effect of T_j is dropped because this tool is intended to avoid temperature measurements. Equation (13) accounts for the different values of V_{dc} between

experiments and datasheet test conditions. If desired, more extensive modeling can be augmented in the tool, as in (15). But (15) is dependent on specific IGBT-diode modules, and considering it in the tool requires adding a preset number of IGBT-diode pairs whose curves should be generated individually in the lab. Experimental results presented later in Section 6.3 show that the tool is not significantly affected by using the approximation in (13). In order to study the effect of discrepancies between V_g and V_{base}, T_j and T_{base}, and R_g and R_{base}, a case-by-case modeling procedure should be followed as in [124] for every module. The ratios of the base values to the actual values differ from one application or datasheet test to another, and the constants υ, σ, κ, μ, ς, and ζ also differ from a module to another. It is well understood that such discrepancies could affect the estimation accuracy, but the effects of such discrepancies are not studied here so as to keep the focus on the tool.

6.2.3 Data Processing

A window is chosen from I_L and p measurements. Curve fitting is performed as explained in Section 6.2.2, and measurements are fetched by the tool. When the tool detects conduction or change in the IGBT or diode state, energy and voltage values are estimated depending on the value of I_L at the instants i and i-1. The energies are initialized to zero and incremented as shown in (54) – (59). Following the conditions in Table 23, $E_{Q,on}$ is incremented as shown in (54) when Q turns on; $E_{Q,off}$ is incremented as shown in (55) when Q turns off; $E_{Q,sw}$ is incremented as shown in (56) when Q turns on or off; E_{rec} is incremented as shown in (57) when D turns off; $E_{Q,cond}$ and $E_{D,cond}$ are incremented as shown in (58) and (59), when Q or D conduct, respectively. A flowchart summarizing energy increments is shown in [182].

$$E_{Q,on}(i)=E_{Q,on}(i\text{-}1) + g_1 I_L(i)^2 + g_2|I_L(i)| + g_3 \quad (54)$$

$$E_{Q,off}(i)=E_{Q,ff}(i\text{-}1) + g_4 I_L(i)^2 + g_5|I_L(i)| + g_6 \quad (55)$$

$$E_{Q,sw}(i)= E_{Q,on}(i) + E_{Q,off}(i) \quad (56)$$

$$E_{rec}(i)=E_{rec}(i\text{-}1) + g_7 I_L(i)^2 + g_8|I_L(i)| + g_9 \quad (57)$$

$$E_{Q,cond}(i)=E_{Q,cond}(i\text{-}1)+V_{ce,sat}(i)\times|I_L(i)|\times[t(i)\text{-}t(i\text{-}1)] \quad (58)$$

$$E_{D,cond}(i)=E_{D,ccond}(i\text{-}1)+V_f(i)\times|I(i)|\times[t(i)\text{-}t(i\text{-}1)], \quad (59)$$

where $V_{ce,sat}(i)=g_{10}I_L(i)^2+g_{11}|I_L(i)|+g_{12}$ and $V_f(I)=g_{13}I_L(i)^2+ g_{14}|I_L(i)|+g_{15}$. In (54)–(59) $E_{Q,sw}$ and $E_{Q,cond}$ are the IGBT total switching and conduction energies, respectively; $E_{D,cond}$ is the diode conduction energy, and all $g_{1\text{-}15}$ are the curve-fitting coefficients for $E_{Q,on}$, $E_{Q,off}$, $E_{D,sw}$, $V_{ce,sat}$, and V_f. When all data points in the selected window are processed, the accumulated energies are divided by the window time width to determine the power losses.

6.3 Tool Validation

Several methods can be used to validate the tool, including measurements of losses, temperatures, or parasitic elements. Direct loss measurements include semiconductor losses, as well as copper losses in connectors, and need special considerations under switching voltage and current waveforms. The tool uses no parasitic models; thus these are not used for validation. Temperature measurements are straightforward but they have two drawbacks. First, thermal resistances shown in Fig. 11 must be known. Second, the temperature measurements vary from one spot to another on the semiconductor devices. Thermal resistances from the device and heat sink datasheets are used to address the first drawback. The second is addressed by assuming a uniform temperature distribution across the device area and the hottest spot is at the center.

An experimental half-bridge inverter, described in Section 6.3.1, was built to validate the tool under periodic and aperiodic switching. Temperature measurements are used to compare measured and estimated losses. Validation under PWM periodic switching is shown in Section 6.3.2, and under aperiodic switching in Section 6.3.3. An example application of the tool for is shown in Section 6.3.4.

6.3.1 Experimental Setup

Verification of the tool based on simulation waveforms was presented in [182]. The tool was compared to Melcosim— an industry-standard loss-estimation commercial software from Mitsubishi— which uses fixed-frequency PWM and implements (9)–(12). Even though comparison with a commercial software is useful for preliminary evaluation, this software contains several approximations, e.g., sinusoidal current shape. Here, the verification is achieved with calorimetry, in addition to comparison with commercial software.

The schematic of a simple experimental half-bridge inverter and R-L load is shown in Fig. 66 where R_L = 1.58 Ω and L_L = 3.1 mH. The resistor R_d forms a current path when I_L < 0. Figure 67 shows the experimental setup where the gate signal comes from the controller for either PWM or hysteresis switching.

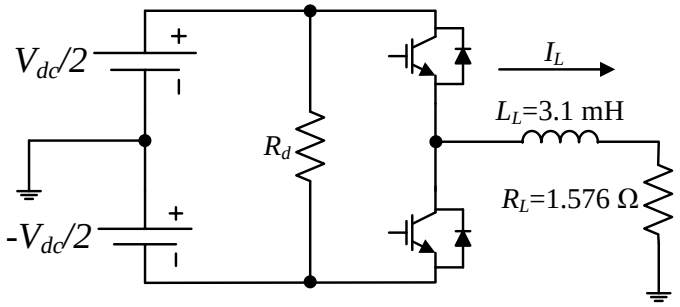

Fig. 66. Schematic of the test circuit

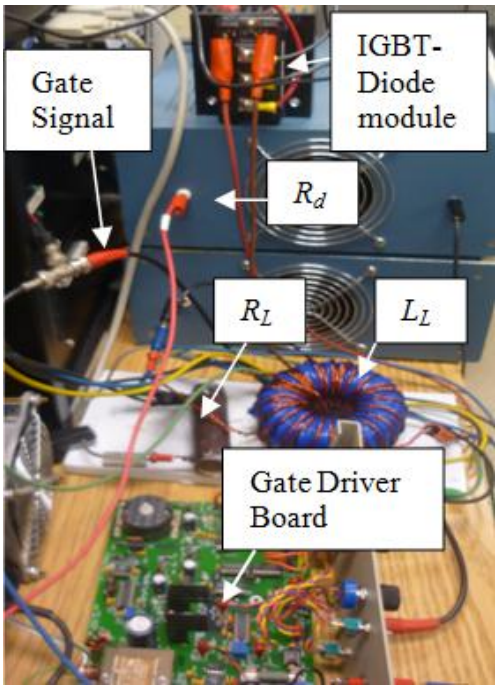

Fig. 67. Experimental setup

The tool is independent of the circuit model; thus load information is not required. I_L and the average V_{dc} are the required measurements; in addition, p is monitored. The commercial software requires measuring the power factor of the fundamental components of I_L and load voltage and the modulation index of the fundamental component of the load voltage. These were obtained using a digital power analyzer but are not required by the tool. The sampling frequency of the oscilloscope was 250 kHz when $f \leq 30$ Hz and 500 kHz when $f > 30$ Hz where f is the fundamental electrical frequency. These sampling frequencies have larger periods than the IGBT and diode turn-on and turn-off times and introduce estimation errors. For better estimation accuracy, measurements with higher sampling rates can be used, but these were not available for this setup.

A CM200DY-12NF half-bridge IGBT-diode module was used for testing. The heat sink was mounted vertically according to the manufacturer specifications under natural convection

cooling. The characteristic curve of $R_{s\text{-}a}$ is shown in Fig. 68 [183]. $R_{c\text{-}s}$ = 0.07 ^{o}C/W as given in the module datasheet. T_c was measured at the module center through a small hole in the heat sink as shown in Fig. 69. Using the zero-order model in Fig. 11, if T_c, T_a, $R_{c\text{-}s}$, and $R_{s\text{-}a}$ are known, P_T can be estimated as $P_T = (T_c - T_a)/(R_{c\text{-}s} + R_{s\text{-}a})$.

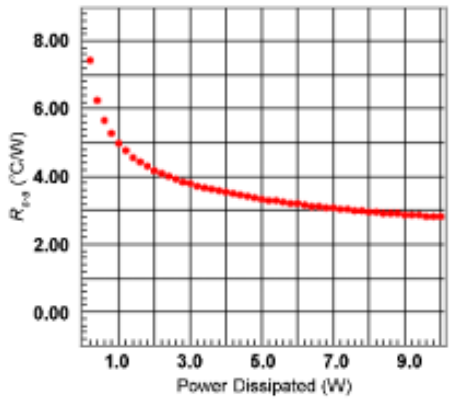

Fig. 68. Heat sink thermal resistance $R_{s\text{-}a}$ [183]

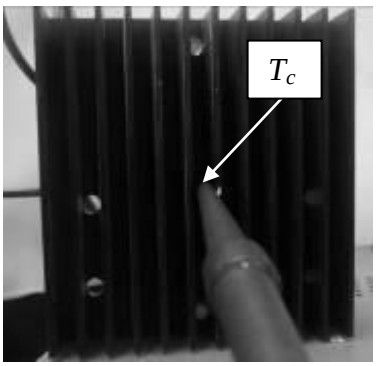

Fig. 69. T_c measurement through a hole at the heat sink center

Two scenarios are studied: the first is fixed-frequency PWM where the commercial software is also compared; the second is under hysteretic control, i.e., aperiodic switching. While both scenarios verify the tool, the second scenario is also intended to demonstrate an example of possible research topics based on the tool—finding a fixed-switching frequency that can be used to model losses under hysteresis switching in commercially available loss-estimation tools. Given a maximum switching rate (f_{max}) that can be achieved by hysteresis, it was shown in [182]

that $f_{max}/2$ could be a good approximation to estimate losses under hysteresis using fixed-frequency tools.

6.3.2 Validation under PWM Switching

The IGBT switching frequency is set to a fixed known value. Several values of f_{sw}, V_{dc}, and f were used to demonstrate that the tool can be applied for different operating conditions. A window of the current and switching pulse is captured over several fundamental cycles. Three methods are used to estimate the total power loss: the proposed tool, temperature measurements, and the commercial software. For 10^5 data points, the total run time of the tool did not exceed 1 minute on a 3.2 GHz, Pentium 4 computer with 1 GB of RAM. A sample result is shown in Fig. 70 for f_{sw} =10 kHz and f = 15 Hz where I_L is not a perfect sinusoid since the R-L load is a first-order filter. Table 24 shows the results of fixed-frequency operation under PWM with measurements used as the reference for error calculation.

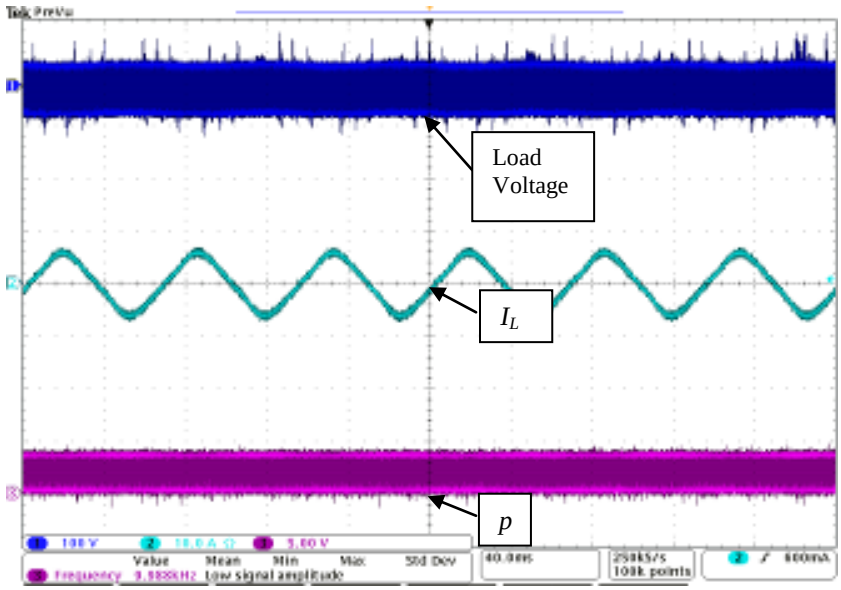

Fig. 70. PWM switching waveforms: Load voltage across R-L (top, 100 V/div), I_L (middle, 10 A/div), logic-level switching pulse (bottom, 5 V/div)

Table 24. Estimates of P_T from the tool, measurements, and commercial software under PWM switching

f_{sw} (kHz)	f (Hz)	V_{dc} (V)	I_L (Arms)	Load Voltage (Vrms)	φ (deg)	T_c (^{o}C)	T_a (^{o}C)	$R_{c\text{-}s}+R_{s\text{-}a}$ (^{o}C/W)	P_T Measured (W)	P_T Tool (W)	Tool Error (%)	P_T Commercial Software (W)	Commercial Software Error (%)
5	50	69.84	7.64	34.29	55.88	42	23	3.07	6.189	7.003	**13.15**	5.96	**-3.699**
10	25	90.17	5.53	43.89	64.73	46	23	3.07	7.492	6.989	**-6.71**	6.00	**-19.913**
10	15	93.96	3.40	45.84	66.52	42	23	3.17	5.994	6.454	**7.68**	4.35	**-27.424**
10	50	70.92	7.39	34.49	56.33	46	23	2.97	7.744	7.719	**-0.32**	6.88	**-11.158**

It is clear in Table 24 that the tool performs well compared to measurements and has an average absolute error of 7%. As seen in the literature, estimation errors that are less than 15% are acceptable in such applications where model uncertainties, curve-fitting approximations, and/or sensitive measurements introduce errors. Results from the commercial software show a higher average absolute error of 15.58%, which is still useful for virtual prototyping, but less accurate than the proposed tool. Results show that the assumption of linear voltage scaling of E_{sw} does not significantly affect the tool performance.

6.3.3 Validation under Hysteresis Switching

Hysteretic current control was implemented in the circuit shown in Fig. 66, resulting in aperiodic switching, as shown in Fig. 71. These waveforms are typical for inductive loads, including motor drives with hysteresis current control. The tool was compared to power loss estimates from temperature measurements as shown in Table 25. These results show that the tool is able to estimate the power loss with an average error of 8.5%. The worst case error is less than 12%. Thus, the tool successfully predicted loss estimates under aperiodic switching using datasheet information. These estimates are believed to be the first experimentally validated results (using calorimetry) of a loss estimation tool under aperiodic switching.

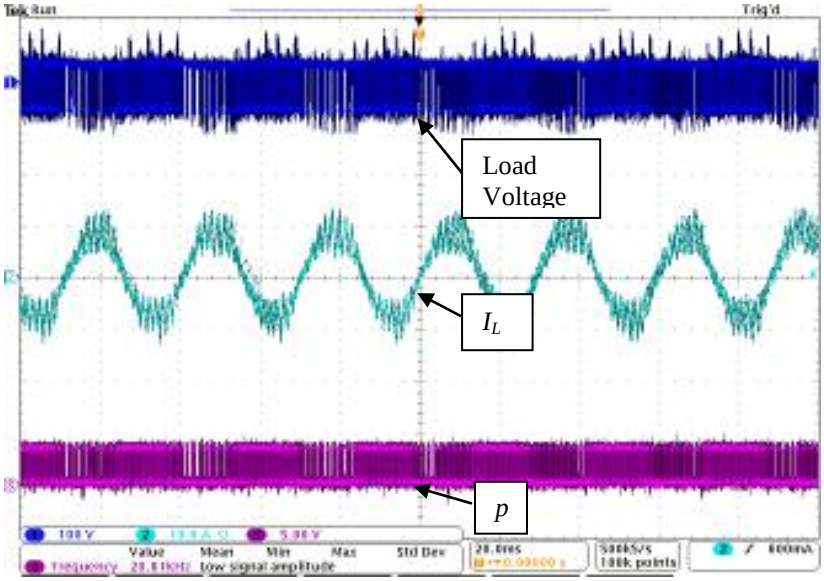

Fig. 71. Hysteresis switching waveforms: Load voltage across R-L (top, 100 V/div), I_L (middle, 10 A/div), logic-level switching pulse (bottom, 5 V/div)

Table 25. Estimates of P_T from the tool and measurements under hysteretic switching

f (Hz)	V_{dc} (V)	I_L (Arms)	T_c (^{o}C)	T_a (^{o}C)	$R_{c\text{-}s}+R_{s\text{-}a}$ (^{o}C/W)	P_T Measured (W)	P_T Tool (W)	Tool Error (%)
30	88	6.32	56	24	2.97	10.774	11.284	**4.73**
15	88.25	4.80	56	24	2.97	10.774	9.507	**-11.76**
50	88.6	4.70	58	24	2.97	11.448	10.618	**-7.25**
50	86	5.80	58	24	2.97	11.448	10.275	**-10.24**

6.3.4 Tool Application Example

The development of such an accurate loss estimation tool is expected to lead to further research in power electronics thermo-electric designs. Such applications include selection of the minimum-loss switching scheme for a certain application, design of minimum-loss power electronics converters, as explained in Section 6.1, etc. One application of the tool was presented in [182] where a fixed-frequency loss-estimation tool was shown to estimate losses under variable switching frequencies. For a certain f_{max} under hysteresis switching, $f_{max}/2$ was shown to give accurate loss estimates of IGBT-diode losses. The tool established here was used to rapidly

estimate losses under different characteristic rates, such as f_{max}, $f_{max}/2$, the average switching frequency (f_{avg}), and the number of switching instants (f_T). No experimental measurements were presented in [182] to validate $f_{max}/2$ as the acceptable value that can be used in fixed-frequency tools. Here, this is validated with calorimetry.

The same experimental setup described earlier was used to update Table 25 with the results from the commercial software at $f_{max}/2$ where f_{max}=50,000 switching instants/second. Again, the tool only requires measurements of I_L, p, and V_{dc}, but the commercial software requires more measurements shown in Table 26. Results from the commercial software at $f_{max}/2$ have higher errors than the tool, with an average of 14.46%. These results are still useful as preliminary approximations of the losses.

Table 26. Estimates of P_T from the tool, measurements, and commercial software under hysteretic switching

f (Hz)	V_{dc} (V)	I_L (Arms)	Load Voltage (Vrms)	φ (degrees)	T_c (^{o}C)	T_a (^{o}C)	$R_{c-s}+R_{s-a}$ (^{o}C/W)	P_T Measured (W)	P_T Tool (W)	Tool Error (%)	P_T @ $f_{max}/2$ Commercial Software (W)	Commercial Software Error (%)
30	88	6.32	42.55	62.14	56	24	2.97	10.774	11.284	**4.73**	10.49	**-2.64**
15	88.25	4.80	42.20	64.00	56	24	2.97	10.774	9.507	**-11.76**	8.90	**-17.34**
50	88.6	4.70	42.50	63.00	58	24	2.97	11.448	10.618	**-7.25**	8.80	**-23.13**
50	86	5.80	42.00	62.10	58	24	2.97	11.448	10.275	**-10.24**	9.77	**-14.66**

CHAPTER 7

CONCLUSIONS AND OPEN RESEARCH TOPICS

This dissertation presented a system-level approach to design and analyze a better IFOC induction motor drive system for present and future applications. Improvements from the efficiency perspective addressed real-time minimum-loss operation. LMTs were reviewed, categorized, and analyzed. Model-based, physics-based, and hybrid LMT categories were compared. Hybrid LMTs, which were first categorized as a separate group in [18, 19], were also emphasized. Three main LMT applications were studied in detail: pump, HEV, and propulsion system. Energy savings greater than 10% were shown in the pump application under the LMT. Around 5% energy savings were shown in the HEV application, and similar savings in the propulsion application. Most of these results were validated experimentally. Sensitivity analysis of a specific model-based LMT was presented. Results showed that even large inaccuracies in R_r lead to an insignificant shift from the minimum power loss. LMTs will yield significant global energy savings when utilized in machines operating with electronic drives and are an essential add-on to any future motor drive.

Among the hybrid LMTs available in the literature, RCC was studied thoroughly from various perspectives. RCC as VC was briefly introduced. A detailed comparison of RCC and ES proved that they are essentially the same, with the only difference being the source of the perturbations utilized to achieve the extremum—RCC uses inherent ripple to estimate the objective function gradient while modern ES utilizes sinusoidal perturbation injections. Mathematically, RCC and ES were derived and found to be similar and their Lyapunov stability was analyzed. The link between RCC and ES was first established here and is expected to lead to further explorations in both control methods.

The application of RCC as an LMT was studied thoroughly. The high-frequency problem was of special interest, and the main reason behind the inability of RCC to work as an LMT was found—energy storage in the magnetizing and leakage inductances. A compensator that helps RCC utilize higher frequencies was derived and simulated in both time and frequency domains. This compensator and its design guidelines complete the design phase of RCC application to induction motor drives.

Due to the LMT effect on the induction motor drive system operation, reliability modeling of the system is essential. A complete systematic procedure was presented here as previous attempts to establish a reliability model of an induction motor drive system were incomplete. Faults in the machine, power electronics, and sensors were studied. Mathematical analysis and drive simulations, which were experimentally verified, yielded a Markov reliability model and an MTTF of 57.2 years. The systematic procedure can be easily modified for higher or lower levels of detail. In order to enhance the system reliability, an open-loop constant V/f controller is engaged whenever a sensor fault occurs. The effect of wait time before switching to the safe-mode was qualitatively studied; the MTTF decreased when the wait time increased. In general, the MTTF improved to over 70 years, i.e., 22.3%. Such a safe-mode drive can be key in future applications that require high safety and reliability standards, such as vehicles.

Better thermo-electric design procedures are desired as power electronics faults are among the major faults that occur in the drive. Problems in the thermal management of power electronics cause severe faults in the inverter and drive—OC and SC faults. Loss estimation in IGBTs and diodes, the most common semiconductors in modern motor drives, is essential for designing better and cost-effective thermal management systems. This reduces power electronics faults. A loss estimation tool that works under any switching scheme was presented. The tool

requires only three measurements: current in a phase, gate signal in that phase, and an average V_{dc}. This tool was experimentally shown to estimate losses under both fixed-frequency and variable switching schemes with an average error of 8%. This tool is expected to lead to several future research topics in the optimal design of power electronics converters while considering the effects of different switching patterns. An application was studied here—identifying a fixed-switching frequency that can be used in fixed-frequency tools to estimate losses under variable switching patterns, specifically, hysteresis.

Thus, the loss estimation tool will lead to better inverter designs, which in turn will lead to higher drive system reliability. In parallel with this, the MTTF of the drive system under minimum-loss operation was shown to be large, and energy savings were achieved. The procedures, designs, results, and analyses presented in this dissertation will to lead to better induction motor drive systems from the perspective of efficiency, reliability, and power electronics.

Several research topics remain open and should be addressed. One topic is a survey of possible energy savings when LMTs are applied globally. Global savings were demonstrated here, but accurate market surveys could be more attractive for possible commercialization of LMTs through government and private funding programs. Another topic is to analyze system reliability for different performance requirements in various applications. The choice of performance requirements for different applications could significantly affect the resulting MTTF. Another topic is to experimentally apply RCC with compensation and modulation/demodulation techniques similar to ES in order to overcome the high-frequency and low SNR problems, respectively. Other RCC- and ES-related topics include a deeper understanding of the link between RCC and VC—although both have a common characteristic of

utilizing perturbations for control purposes, the link between them has not yet been well established. Another topic is to generalize the link between RCC and ES for any perturbation waveform since only sinusoidal, exponential, and triangular waveforms were studied here; also, mathematical results in the works of Nesić and Kristić on stability, choice of the perturbation frequency and amplitude, and applications of ES to different system forms, can be extended to RCC. One more open research topic is to augment optimal power electronics designs, i.e., choice of devices, switching scheme, operating voltages, etc., to the loss estimation tool to generate several designs. Among them one or more optimal designs are chosen. Such a procedure would be valuable in showing power electronics design trade-offs and the effect of better thermo-electric designs on the overall drive system reliability. The models developed for optimal power electronics designs can also be added to machine loss models to achieve system-level loss minimization.

APPENDIX A

INPUT POWER TRANSFER FUNCTION, FIELD-ORIENTED CONTROL EQUATIONS, AND MACHINE PARAMETERS

The induction machine model in the dq0 synchronous frame is shown in Fig. 18 where ω_e replaces ω_a. For a squirrel-cage induction machine, the rotor voltages are zero, and for balanced conditions, the 0-voltages are zero. The derivation of (29) proceeds as follows:

Let $D = L_m^2 - L_r L_s$, then $i_{qs} = \frac{-L_r}{D}\lambda_{qs} + \frac{L_m}{D}\lambda_{qr}$ and $i_{ds} = \frac{-L_r}{D}\lambda_{ds} + \frac{L_m}{D}\lambda_{dr}$. Also,

$v_{qs} = R_s i_{qs} + s\lambda_{qs} + \omega_e \lambda_{ds}$ and $v_{ds} = R_s i_{ds} + s\lambda_{ds} - \omega_e \lambda_{qs}$ where s is the Laplace domain derivative.

$$P_{in} = \frac{3}{2}\left(v_{qs} i_{qs} + v_{ds} i_{ds}\right) \tag{60}$$

$$P_{in} = \frac{3}{2}\left(R_s i_{qs}^2 + s\lambda_{qs} i_{qs} + \omega_e \lambda_{ds} i_{qs} + R_s i_{ds}^2 + s\lambda_{ds} i_{ds} - \omega_e \lambda_{qs} i_{ds}\right) \tag{61}$$

$$P_{in} = \frac{3}{2}\left(\begin{array}{l} \frac{R_s}{D^2}\left(L_m\lambda_{qr} - L_r\lambda_{qs}\right)^2 + \frac{s}{D}\lambda_{qs}\left(L_m\lambda_{qr} - L_r\lambda_{qs}\right) + \frac{\omega_e\lambda_{ds}}{D}\left(L_m\lambda_{qr} - L_r\lambda_{qs}\right) \\ + \frac{R_s}{D^2}\left(L_m\lambda_{dr} - L_r\lambda_{ds}\right)^2 + \frac{s}{D}\lambda_{ds}\left(L_m\lambda_{dr} - L_r\lambda_{ds}\right) - \frac{\omega_e\lambda_{qs}}{D}\left(L_m\lambda_{dr} - L_r\lambda_{ds}\right) \end{array}\right) \tag{62}$$

$$\frac{\partial P_{in}}{\partial \lambda_{dr}} = \frac{3}{2}\left(\frac{2L_m R_s}{D^2}\left(L_m\lambda_{dr} - L_r\lambda_{ds}\right) + s\frac{L_m\lambda_{ds}}{D} - \frac{\omega_e\lambda_{qs}L_m}{D}\right) \tag{63}$$

$$\therefore \frac{\partial P_{in}}{\partial \lambda_{dr}} = \frac{3L_m}{2D^2}\left(s\lambda_{ds}D - \omega_e\lambda_{qs}D - 2L_r R_s\lambda_{ds} + 2L_m R_s\lambda_{dr}\right) \tag{64}$$

If P_{in} is considered negative as $P_{in} = \frac{-3}{2}\left(v_{qs} i_{qs} + v_{ds} i_{ds}\right)$, then

$$\frac{\partial P_{in}}{\partial \lambda_{dr}} = \frac{-3L_m}{2D^2}\left(s\lambda_{ds}D - \omega_e\lambda_{qs}D - 2L_r R_s\lambda_{ds} + 2L_m R_s\lambda_{dr}\right). \tag{65}$$

The choice of negative or positive P_{in} does not affect the optimal λ_{dr}, but the phase at the optimum would be either 90^o or 270^o. The values of λ_{ds}, λ_{qs}, and ω_e are chosen for an operating point of T_e and ω_r, where $\omega_r = \frac{n_p}{2}\omega_m$ and the relation between T_e and ω_m is a known load characteristic. λ_{dr} is stepped to find its optimal value; thus, it is assumed to be known and the other unknowns are:

$$i_{qs} = \frac{4L_r T_e}{3n_p L_m \lambda_{dr}} \tag{66}$$

$$i_{ds} = \frac{\lambda_{dr}}{L_m} \tag{67}$$

$$i_{qr} = \frac{L_m}{L_r} i_{qs} \tag{68}$$

$$\lambda_{qs} = L_s i_{qs} + L_m i_{qr} \tag{69}$$

$$\lambda_{ds} = L_s i_{ds} \tag{70}$$

where $i_{dr}=\lambda_{qr}=0$ under IFOC. ω_r is known for a given T_e and load, and ω_e can be estimated as

$$\omega_e = \omega_r + \omega_{sl} = \omega_r + \frac{i_{qs} R_r}{i_{ds} L_r}. \tag{71}$$

Machine parameters are given in Table 27.

Table 27. Machine parameters

Motor Parameters	Test Motor	HEV Machine
Rated power	1.5 hp	10 hp
Rated speed	1750 rpm	1746 rpm
Number of poles (n_p)	4	4
Referred rotor resistance (R_r')	0.7309 Ω	0.01438 Ω
Stator resistance (R_s)	1.5293 Ω	0.0248 Ω
Referred rotor leakage inductance (L_{lr}')	0.005343 H	114e-6 H
Stator leakage inductance (L_{ls})	0.00356 H	114e-6 H
Magnetizing inductance (L_m)	0.19778 H	0.0036 H
Core Loss (R_c)	505 Ω	19 Ω
Inertia (J)	0.01 Kg.m^2	0.03 Kg.m^2

APPENDIX B

LOAD SUPPORT ISSUES

The derivation of the lower limit on λ_{dr} proceeds as follows:

$$T_e = \frac{3n_p}{4}\left(\lambda_{qr} i_{dr} - \lambda_{dr} i_{qr}\right) \tag{72}$$

$$P_o = T_e \omega_m \tag{73}$$

$$P_o = \frac{3n_p \omega_m}{4}\left(\lambda_{qr} i_{dr} - \lambda_{dr} i_{qr}\right). \tag{74}$$

Under IFOC, $\lambda_{qr} = 0$, $\lambda_{dr} = \lambda_{dr}^c$, and $P_o = P_o^c$ where the *c* superscript resembles a command quantity. Thus,

$$-\lambda_{dr} i_{qr} \frac{3n_p \omega_m}{4} = P_o^c \tag{75}$$

$$-\lambda_{dr}^c \left(-\frac{L_m}{L_r} i_{qs}\right) \frac{3n_p \omega_m}{4} = P_o^c \tag{76}$$

$$\lambda_{dr}^c = \frac{4P_o^c L_r}{3L_m i_{qs} n_p \omega_m} \tag{77}$$

But $\omega_m = \omega_m^c$ and $T_e^c = \frac{P_o^c}{\omega_m^c}$, then

$$\lambda_{dr}^c = \frac{4T_e^c L_r}{3L_m i_{qs} n_p}. \tag{78}$$

Therefore, if the maximum allowed i_{qs} is its rated value i_{rated},

$$\lambda_{dr}^c \geq \frac{4T_e^c L_r}{3L_m i_{rated} n_p}. \tag{79}$$

Another bound on λ_{dr} can be found as follows:

With λ_{qs} given in (A.10),

$$i_{qr} = \frac{\lambda_{qs} - L_s i_{qs}}{L_m} \tag{80}$$

$$\lambda_{qr} = L_r i_{qr} + L_m i_{qs} \tag{81}$$

Then,

$$\lambda_{qr} - \frac{L_r}{L_m}\lambda_{qs} = i_{qs}\left(L_m - \frac{L_r L_s}{L_m}\right) \tag{82}$$

$$i_{qs} = \left(\lambda_{qr} - \frac{L_r}{L_m}\lambda_{qs}\right)\frac{L_m}{L_m^2 - L_r L_s} = -\frac{L_r}{L_m}\lambda_{qs}\frac{L_m}{L_m^2 - L_r L_s}. \tag{83}$$

Let $\gamma_\lambda = -L_m^2 + L_r L_s$, then

$$i_{qs} = \frac{L_r}{\gamma_\lambda}\lambda_{qs} \tag{84}$$

$$\lambda_{dr}^c = \frac{4T^c L_r}{3L_m\left(\frac{L_r}{\gamma_\lambda}\lambda_{qs}\right)n_p} \tag{85}$$

$$\lambda_{dr}^c = \frac{4\gamma_\lambda}{3L_m n_p}\frac{T^c}{\lambda_{qs}}. \tag{86}$$

For $0 < \lambda_{qs} < \lambda_{qs,\max}$,

$$\lambda_{dr}^c \geq \frac{4\gamma_\lambda}{3L_m n_p}\frac{T^c}{\lambda_{qs,\max}}. \tag{87}$$

For λ_{qs} given in (69), $\lambda_{qs} \leq L_{ls} i_{qs} \leq L_{ls} i_{rated}$ if i_{qr}>0. Thus,

$$\lambda_{dr} \geq \frac{4\gamma_\lambda}{3n_p L_m L_{ls}}\frac{T^c}{i_{rated}}. \tag{88}$$

The derivation of $P_{in,s}$ is as follows:

The objective is to find P_{in} given in (60) as a function of λ_{dr} so that a shift in λ_{dr} can be introduced. When the three-phase induction machine is operating under IFOC and in steady-state, the following is true:

$$v_{qs} = i_{qs}R_s + \omega_e\lambda_{ds} = \frac{4L_rR_sT_e}{3n_pL_m}\frac{1}{\lambda_{dr}} + \frac{\omega_eL_s}{L_m}\lambda_{dr} \tag{89}$$

$$\begin{aligned} v_{ds} &= i_{ds}R_s - \omega_e\lambda_{qs} \\ &= \frac{R_s}{L_m}\lambda_{dr} - \omega_e\left(L_si_{qs} + L_mi_{qr}\right) \\ &= \frac{R_s}{L_m}\lambda_{dr} - \omega_e\left(L_si_{qs} - \frac{L_m^2}{L_r}i_{qs}\right) \\ &= \frac{R_s}{L_m}\lambda_{dr} - \omega_ei_{qs}\left(L_s - \frac{L_m^2}{L_r}\right) \\ &= \frac{R_s}{L_m}\lambda_{dr} - \omega_e\frac{4L_rT_e}{3n_pL_m\lambda_{dr}}\left(L_s - \frac{L_m^2}{L_r}\right) \\ &= \frac{R_s}{L_m}\lambda_{dr} - \frac{4T_e\omega_e}{3n_p\lambda_{dr}}\left(\frac{L_sL_r}{L_m} - L_m\right) \end{aligned} \tag{90}$$

Let $\alpha' = \frac{4L_r}{3n_pL_m}$, $\beta' = \alpha'^2 R_s$, and $\gamma' = \frac{\omega_eL_s}{L_m}\alpha'$. Then,

$$\begin{aligned} v_{qs}i_{qs} &= \left(i_{qs}R_s + \omega_e\frac{L_s}{L_m}\lambda_{dr}\right)i_{qs} = i_{qs}^2R_s + \frac{\omega_eL_s}{L_m}\lambda_{dr}i_{qs} \\ &= \alpha'^2\frac{T_e^2}{\lambda_{dr}^2}R_s + \frac{\omega_eL_s}{L_m}\alpha'T_e \\ &= \beta'\frac{T_e^2}{\lambda_{dr}^2} + \gamma'T_e \end{aligned} \tag{91}$$

Let $\xi' = \frac{R_s}{L_m^2}$, and $\sigma' = \frac{4\omega_e}{3n_pL_m}\left(\frac{L_sL_r}{L_m} - L_m\right)$. Then,

$$
\begin{aligned}
v_{ds}i_{ds} &= \left(\frac{R_s}{L_m}\lambda_{dr} - \frac{4T_e\omega_e}{3n_p\lambda_{dr}}\left(\frac{L_sL_r}{L_m} - L_m\right)\right)\frac{\lambda_{dr}}{L_m} \\
&= \frac{R_s}{L_m^2}\lambda_{dr}^2 - \frac{4T_e\omega_e}{3n_pL_m}\left(\frac{L_sL_r}{L_m} - L_m\right) \\
&= \xi'\lambda_{dr}^2 - \sigma'T_e
\end{aligned}
\quad . \tag{92}
$$

Let $\phi = \frac{3}{2}\beta'$, $\xi'' = \frac{3}{2}\xi'$, and $\delta' = \frac{3}{2}(\gamma' - \sigma')$. Then,

$$
P_{in} = \frac{3}{2}\left(\beta'\frac{T_e^2}{\lambda_{dr}^2} + \gamma'T_e + \xi'\lambda_{dr}^2 - \sigma'T_e\right) = \phi\frac{T_e^2}{\lambda_{dr}^2} + \xi''\lambda_{dr}^2 + \delta'T_e . \tag{93}
$$

For a shift in λ_{dr} given by Δ_λ, $P_{in,s}$ can be found as follows:

$$
\begin{aligned}
P_{in,s} &= \phi\frac{T_e^2}{\left(\lambda_{dr} + \Delta_\lambda\right)^2} + \xi''\left(\lambda_{dr} + \Delta_\lambda\right)^2 + \delta'T_e \\
&= \phi\frac{T_e^2}{\left(\lambda_{dr} + \Delta_\lambda\right)^2} + \phi\frac{T_e^2}{\lambda_{dr}^2} - \phi\frac{T_e^2}{\lambda_{dr}^2} + \xi''\lambda_{dr}^2 + 2\xi''\lambda_{dr}\Delta_\lambda + \xi''\Delta_\lambda^2 + \delta'T_e \\
&= P_{in} + \phi\frac{T_e^2}{\left(\lambda_{dr} + \Delta_\lambda\right)^2} - \phi\frac{T_e^2}{\lambda_{dr}^2} + 2\xi''\lambda_{dr}\Delta_\lambda + \xi\Delta_\lambda^2 \\
&= P_{in} + \phi T_e^2\left(\frac{\lambda_{dr}^2 - \left(\lambda_{dr} + \Delta_\lambda\right)^2}{\lambda_{dr}^2\left(\lambda_{dr} + \Delta_\lambda\right)^2}\right) + 2\xi''\lambda_{dr}\Delta_\lambda + \xi''\Delta_\lambda^2 \\
&= P_{in} + \phi T_e^2\left(\frac{-2\lambda_{dr}\Delta_\lambda - \Delta_\lambda^2}{\lambda_{dr}^4 + 2\lambda_{dr}^3\Delta_\lambda + \lambda_{dr}^2\Delta_\lambda^2}\right) + 2\xi''\lambda_{dr}\Delta_\lambda + \xi''\Delta_\lambda^2
\end{aligned}
\quad . \tag{94}
$$

Let $\Gamma = \left(\frac{-2\lambda_{dr}\Delta_\lambda - \Delta_\lambda^2}{\lambda_{dr}^4 + 2\lambda_{dr}^3\Delta_\lambda + \lambda_{dr}^2\Delta_\lambda^2}\right)$ and $\Lambda = 2\xi''\lambda_{dr}\Delta_\lambda + \xi''\Delta_\lambda^2$. Then,

$$
P_{in,s} = P_{in} + \phi T_e^2\Gamma + \Lambda . \tag{95}
$$

APPENDIX C

EXPERIMENTAL SETUP

The experimental setup is shown in Fig. 72.

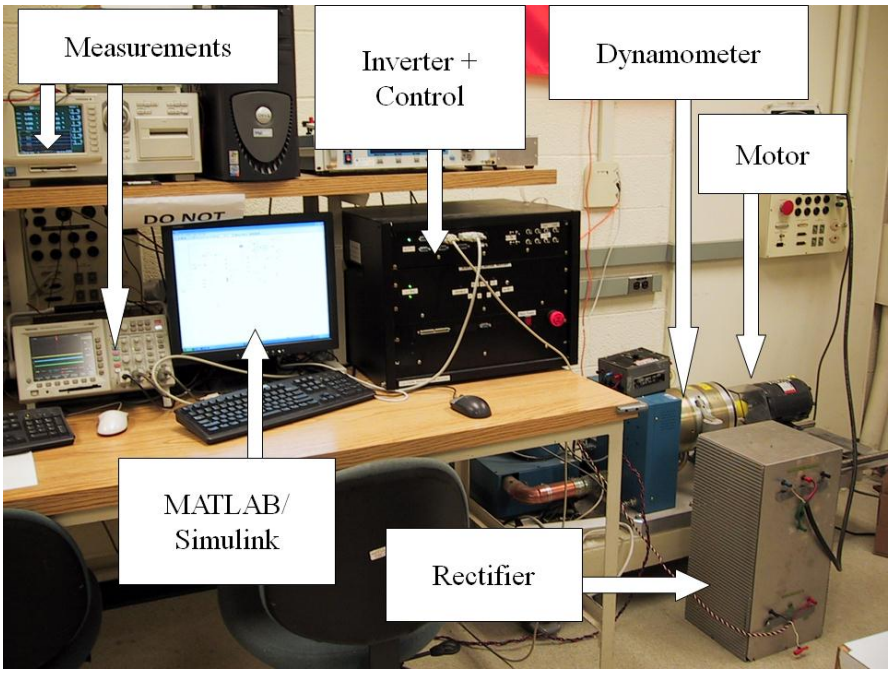

Fig. 72. Experimental setup of the 1.5 hp induction machine ©2010 IEEE

The setup consists of the following main components:

- Modular inverter (inverter+control): three-phase inverter rated at 400 V, 10 A with a built-in control board. The control board utilizes the eZdspF2812 [184] which is based on the TMS320F2812 DSP from Texas Instruments (TI). The eZdspF2812 can be programmed using MATLAB/Simulink graphical programming. C code is generated from the graphical program (block diagram) and compiled to the DSP using Code Composer Studio from TI. Fixed-point math is used in the block diagram as described in [185]. Details about the Simulink blocks used in the DSP are discussed in [186]. The DSP communicates with the computer in real time through real-time data exchange

(RTDX). Users can program a GUI to send and receive data to the DSP in real time using RTDX.

- Dynamometer and controller: The dynamometer is a hysteresis dynamometer controlled using the DSP6001 from Magtrol. The dynamometer acts as the load on the induction machine shaft and can be controlled in either speed or torque modes. In the setup shown in Fig. C.1, speed control is implemented on the DSP using IFOC, and torque control is applied using the dynamometer. Serial communication between the dynamometer controller and the PC allows the user to send torque commands to the dynamometer from the same GUI that runs IFOC. This helps achieve simultaneous torque and speed control. Details about the controller and its setup with the hysteresis dynamometer are available in [187].
- Induction motor: The three-phase induction motor used in the setup has a power rating of 1.5 hp. Its parameters are given in Table A.1 as the "Test motor."
- Rectifier: Straightforward three-phase diode rectifier supplied by the 208 V line-line in the lab and yields around 300 V dc bus. The frontend of the modular inverter is not used in these experiments as RCC would potentially use rectifier ripple at 360 Hz which is filtered out in the frontend, but available in the rectifier used.
- Measurements: Two main pieces of measurement equipment are used. The first and essential one is the Yokogawa WT1600 digital power analyzer which can monitor up to six phases simultaneously. This analyzer can compute power, power factor, harmonic distortion, and several other important power-related measurements. Its documentation is available at [188]. Other measurements are available on the Tektronix oscilloscope model TDS 3034.

APPENDIX D

MARKOV MODEL AND STATE TRANSITION MATRIX

The Markov model of the drive system under IFOC is shown in Fig. 73.

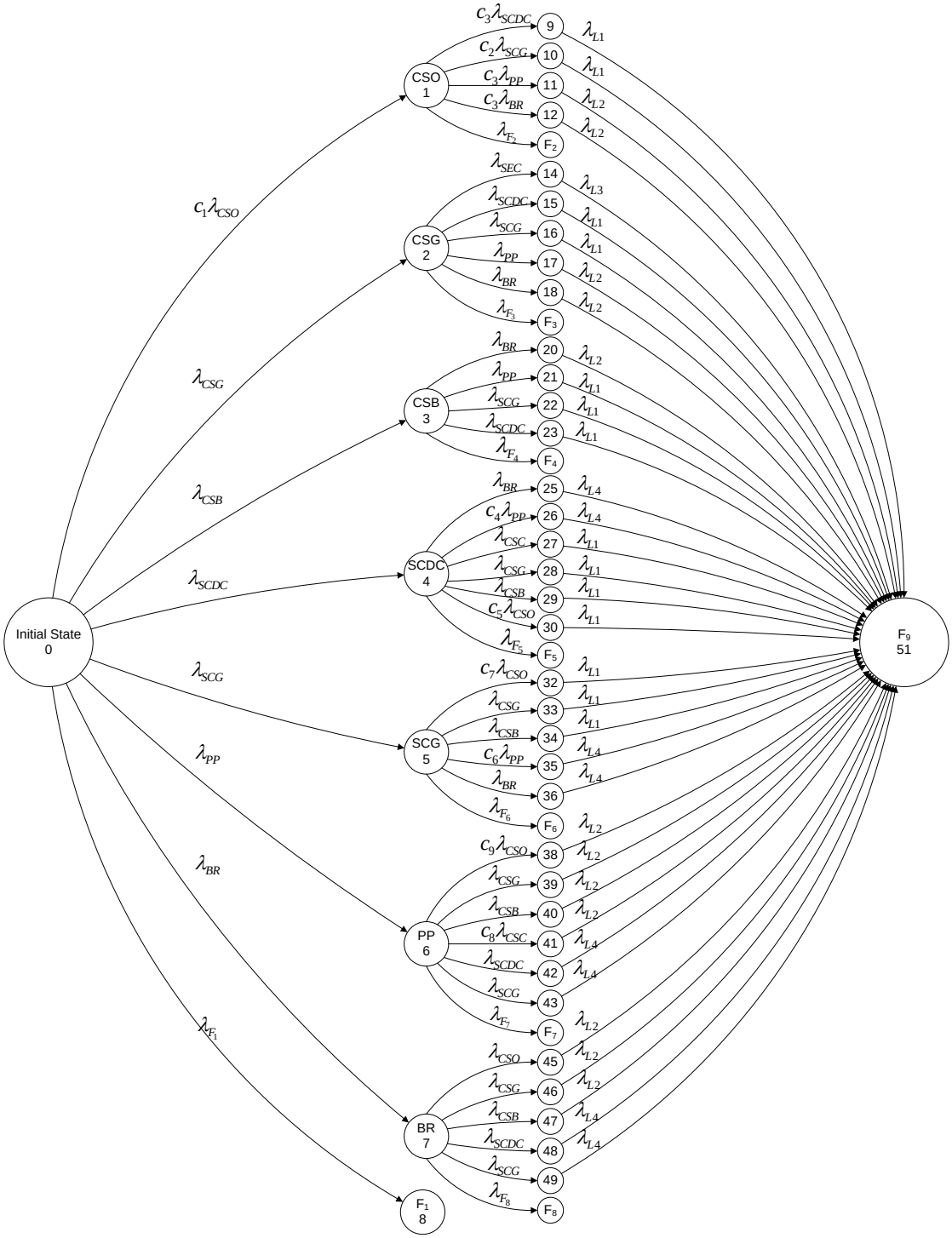

Fig. 73. Markov model of the induction motor drive system under IFOC

Non-zero elements in the state-transition matrix **Φ** are shown in Table 28.

Table 28. Non-zero elements of the state transition matrix

Element	Value
Φ[1,1]	$-(c_1\lambda_{CSO} + \lambda_{CSG} + \lambda_{CSB} + \lambda_{SCDC} + \lambda_{SCG} + \lambda_{PP} + \lambda_{BR} + \lambda_{F1})$
Φ[1,2]	$c_1\lambda_{CSO}$
Φ[2,2]	$-(c_3\lambda_{SCDC} + c_2\lambda_{SCG} + c_3\lambda_{PP} + c_3\lambda_{BR} + \lambda_{F2})$
Φ[2,9]	$c_3\lambda_{SCDC}$
Φ[2,10]	$c_2\lambda_{SCG}$
Φ[2,11]	$c_3\lambda_{PP}$
Φ[2,12]	$c_3\lambda_{BR}$
Φ[3,3]	$-(\lambda_{SEC} + \lambda_{SCDC} + \lambda_{SCG} + \lambda_{PP} + \lambda_{BR} + \lambda_{F3})$
Φ[3,13]	λ_{SEC}
Φ[4,4]	$-(\lambda_{SCDC} + \lambda_{SCG} + \lambda_{PP} + \lambda_{BR} + \lambda_{F4})$
Φ[5,5]	$-(\lambda_{CSC} + \lambda_{CSG} + \lambda_{CSB} + c_5\lambda_{CSO} + c_4\lambda_{PP} + \lambda_{BR} + \lambda_{F5})$
Φ[5,23]	$c_4\lambda_{PP}$
Φ[5,24]	λ_{CSC}
Φ[5,26]	$c_5\lambda_{CSO}$
Φ[6,6]	$-(c_7\lambda_{CSO} + \lambda_{CSG} + \lambda_{CSB} + c_6\lambda_{PP} + \lambda_{BR} + \lambda_{F6})$
Φ[6,28]	$c_7\lambda_{CSO}$
Φ[6,31]	$c_6\lambda_{PP}$
Φ[7,7]	$-(\lambda_{CSO} + \lambda_{CSG} + \lambda_{CSB} + c_8\lambda_{CSC} + \lambda_{SCDC} + \lambda_{SCG} + \lambda_{F7})$
Φ[7,33]	λ_{CSO}
Φ[7,36]	$c_8\lambda_{CSC}$
Φ[8,8]	$-(c_9\lambda_{CSO} + \lambda_{CSG} + \lambda_{CSB} + \lambda_{SCDC} + \lambda_{SCG} + \lambda_{F8})$
Φ[8,39]	$c_9\lambda_{CSO}$
Φ[1,3], **Φ**[5,25], **Φ**[6,29], **Φ**[7,34], **Φ**[8,40]	λ_{CSG}
Φ[1,4], **Φ**[5,27], **Φ**[6,30], **Φ**[7,35], **Φ**[8,41]	λ_{CSB}
Φ[1,5], **Φ**[3,14], **Φ**[4,21], **Φ**[7,37], **Φ**[8,42]	λ_{SCDC}
Φ[1,6], **Φ**[3,15], **Φ**[4,20], **Φ**[7,38], **Φ**[8,43]	λ_{SCG}
Φ[1,7], **Φ**[3,16], **Φ**[4,19]	λ_{PP}
Φ[1,8], **Φ**[3,17], **Φ**[4,18], **Φ**[5,22], **Φ**[6,32]	λ_{BR}
Diagonal elements **Φ**[*i*,*i*] *i*=9, 10, 14, 15, 20, 21, 24– 30.	$\lambda_{SEC} + \lambda_{SEO} + \lambda_{SEG} + \lambda_{PP} + \lambda_{BR}$
Diagonal elements **Φ**[*i*,*i*] *i*=11, 12, 16–19, 33–36, 39–41.	$\lambda_{SEC} + \lambda_{SEO} + \lambda_{SEG} + \lambda_{SCDC} + \lambda_{SCG} + \lambda_{OC}$
Φ[13,13]	$\lambda_{SCDC} + \lambda_{SCG} + \lambda_{OC} + \lambda_{PP} + \lambda_{BR}$
Diagonal elements **Φ**[*i*,*i*] *i*=22, 23, 31, 32, 37, 38, 42, 43.	$\lambda_{SEC} + \lambda_{SEO} + \lambda_{SEG} + \lambda_{OC} + \lambda_{CSG} + \lambda_{CSB} + \lambda_{CSC}$

Mathematica script for finding the MTTF of the drive system under IFOC:

```
Clear["Global`*"]
l0=-(locs (1-c1)+lgcs+lbcs+lscdc+lscg+lpp+lbr+lf1);
l1=-(lscdc (1-c3)+lscg (1-c2)+lpp (1-c3)+lbr (1-c3)+lf2);
l2=-(lcse+lscdc+lscg+lpp+lbr+lf3);
l3=-(lbr+lpp+lscg+lscdc+lf4);
l4=-(lbr+lpp (1-c4)+lccs+lgcs+locs (1-c5)+lf5);
l5=-(locs (1-c7)+lgcs+lbcs+lpp (1-c6)+lbr+lf6);
```

```
l6=-(locs (1-c9)+lgcs+lbcs+lccs (1-c8)+lscdc+lscg+lf7);
l7=-(locs+lgcs+lbcs+lscdc+lscg+lf8);

lf1=lose+lgse+lcse+lccs+loc+c1*locs;
lf2=lose+lgse+lcse+loc+c2*lscg+c3*(lscdc+lpp+lbr);
lf3=lose+lgse+loc;
lf4=lose+lgse+lcse+loc;
lf5=lose+lgse+lcse+c4*lpp+c5*locs;
lf6=lose+lgse+lcse+lccs+c6*lpp+c7*locs;
lf7=lose+lgse+lcse+loc+c8*lccs;
lf8=lose+lgse+lcse+loc+lccs+c9*locs;

ll1=lcse+lose+lgse+lpp+lbr;
ll2=lscdc+lscg+loc+lcse+lose+lgse;
ll3=lscdc+lscg+loc+lbr+lpp;
ll4=lcse+lose+lgse+locs+lgcs+lbcs+lccs


K=… (NOTE: K is very large to show here, but K = Φ)


"Finding the Transpose of K"
KT=Transpose[K];

"Finding the exponential of K_Transpose"
eKT=MatrixExp[KT*t];

"Finding the dimensions of the exponential to set the size of
the initial condition of the probability array"
Dim=Dimensions[eKT]
p0=ConstantArray[0,Dim[[1]]];
p0[[1]]=1;
p0;

"Final probability result"
P=eKT.p0;

"Finding zero layer probability"
P0=P[[1]];

"Finding first layer probability"
P1=P[[2;;8]];
P1sum=Total[P1];

"Finding second layer probability"
P2=P[[9;;42]];
```

```
P2sum=Total[P2];

lscdc=2*10^(-6)*10^(-6);
lscg=2*10^(-6)*10^(-6);
locs=1*10^(-7)*10^(-7);
lgcs=1*10^(-7)*10^(-7);
lbcs=1*10^(-7)*10^(-7);
lccs=1*10^(-7)*10^(-7);
lose=7.4*10^(-7)*10^(0);
lgse=4.2*10^(-7)*10^(0);
lcse=1.9*10^(-7)*10^(0);
loc=1*10^(-7)*10^(-7);
lbr=1*10^(-7)*10^(-7);
lpp=1*10^(-7)*10^(-7);
c1=1/5;
c2=3/4;
c3=1/2;
c4=2/5;
c5=4/5;
c6=2/5;
c7=4/5;
c8=2/5;
c9=2/5;

"Finding Reliability"
R=Total[P]

"Fidning MTTF"
MTTF=Integrate[R,{t,0,∞}
```

REFERENCES

[1] General Motors, http://www.chevrolet.com/pages/open/default/future/volt.do, 2010.

[2] Tesla Motors, http://www.teslamotors.com/roadster/specs, 2010.

[3] M. Amrhein and P. T. Krein, "Dynamic simulation for analysis of hybrid electric vehicle system and subsystem interactions, including power electronics," *IEEE Trans. Veh. Technol.*, vol. 54, pp. 825-836, May 2005.

[4] M. N. Uddin and S. W. Nam, "New online loss-minimization-based control of an induction motor drive," *IEEE Trans. Power Electron.*, vol. 23, pp. 926-933, Mar. 2008.

[5] S. M. Yang, "Loss-minimization control of vector-controlled induction motor drives," in *IEEE Int. Conf. on Power Electron. and Drive Syst.*, 2003, pp. 37-45.

[6] "Up to 70% savings on the energy bills for your motors!" Schneider Electric, Knightdale, NC 2010.

[7] D. S. Kirschen, D. W. Novotny, and W. Suwanwisoot, "Minimizing induction motor losses by excitation control in variable frequency drives," *IEEE Trans. Ind. Appl.*, vol. IA-20, pp. 1244-1250, Sept. 1984.

[8] M. H. Park and S. K. Sul, "Microprocessor-based optimal-efficiency drive of an induction motor," *IEEE Trans. Ind. Electron.*, vol. IE-31, pp. 69-73, Feb. 1984.

[9] A. M. Bazzi, A. D. Dominguez-Garcia, and P. T. Krein, "Markov reliability modeling for induction motor drives under field-oriented control, " *IEEE Trans. Power Electron.*, 2010, submitted.

[10] T. Anzawa, Y. Qiang, M. Yamagiwa, T. Shibutani, and M. Shiratori, "Power cycle fatigue reliability evaluation for power device using coupled electrical-thermal-mechanical analysis," in *Intersociety Conf. on Thermal and Thermomechanical Phenomena in Electron. Syst.*, 2008, pp. 815-821.

[11] C. Liuchen, "Recent developments of electric vehicles and their propulsion systems," *IEEE Aerosp. Electron. Syst. Mag.*, vol. 8, pp. 3-6, Dec. 1993.

[12] K. Clarkson, T. Trumbo, and L. Kueng, "Selection criteria and application of a 16000 HP, 4-pole induction motor for a compressor drive," in *Ind. Applicat. Soc. Annu. Petroleum and Chemical Ind. Conf.*, 1998, pp. 165-172.

[13] J. L. Oldenkamp and S. C. Peak, "Selection and Design of an Inverter-Driven Induction Motor for a Traction Drive System," *IEEE Trans. Ind. Appl.*, vol. IA-21, pp. 259-265, Jan. 1985.

[14] H. Lesch and J. Mantooth, "Design considerations and performance of AC drives on large paper machine," in *Annu. Pulp and Paper Ind. Tech. Conf.*, 1992, pp. 142-147.

[15] M. J. Melfi and R. T. Hart, "Considerations for the use of AC induction motors on variable frequency controllers in high performance applications," in *IEEE Annu. Textile, Fiber and Film Ind. Tech. Conf.*, 1992, pp. 8/1-8/9.

[16] I. Groning and C. Kaehler, "Increase of the performance of induction motors," in *IEEE Int. Elect. Machines and Drives Conf.*, 2007, pp. 1471-1476.

[17] C. Lewis, "The advanced induction motor," in *IEEE Power Eng. Soc. Summer Meeting*, 2002, pp. 250-253.

[18] A. M. Bazzi and P. T. Krein, "A survey of real-time power-loss minimizers for induction motors," in *IEEE Elect. Ship Technologies Symp.*, 2009, pp. 98-106.

[19] A. M. Bazzi and P. T. Krein, "Review of methods for real-time loss minimization in induction machines," *IEEE Trans. Ind. Appl.*, 2010, to be published.

[20] J. M. D. Murphy and M. G. Egan, "A comparison of PWM strategies for inverter-fed induction motors," *IEEE Trans. Ind. Appl.*, vol. IA-19, pp. 363-369, May 1983.

[21] R. Krishnan and A. S. Bharadwaj, "A comparative study of various motor drive systems for aircraft applications," in *IEEE Ind. Applicat. Soc. Annu. Meeting*, 1991, pp. 252-258.

[22] C. S. Kallesoe, V. Cocquempot, and R. Izadi-Zamanabadi, "Model based fault detection in a centrifugal pump application," *IEEE Trans. Control Syst. Technol.*, vol. 14, pp. 204-215, Mar. 2006.

[23] L. Szentirmai and A. Varadi, "Computerised fault diagnosis of induction motor drives," in *Int. Conf. on Elect. Machines and Drives*, 1995, pp. 182-186.

[24] Y. Chia-Chou and N. A. O. Demerdash, "Induction motor-drive systems with fault tolerant inverter-motor capabilities," in *IEEE Int. Elect. Machines and Drives Conf.*, 2007, pp. 1451-1458.

[25] T. G. Habetler, R. Naik, and T. A. Nondahl, "Design and implementation of an inverter output LC filter used for dv/dt reduction," *IEEE Trans. Power Electron.*, vol. 17, pp. 327-331, May 2002.

[26] M. H. Nagrial, A. Hellany, and J. Rizk, "Simulation of the effects of cables on inverter fed motor drive systems," in *Int. Conf. on Simulation*, 1998, pp. 368-374.

[27] D. A. Rendusara and P. N. Enjeti, "An improved inverter output filter configuration reduces common and differential modes dv/dt at the motor terminals in PWM drive systems," *IEEE Trans. Power Electron.*, vol. 13, pp. 1135-1143, Nov. 1998.

[28] L. Umanand and S. R. Bhat, "Optimal and robust digital current controller synthesis for vector-controlled induction motor drive systems," *IEE Proc. Elect. Power Applicat.*, vol. 143, pp. 141-150, Mar. 1996.

[29] M. A. Brdys and T. Du, "Algorithms for joint state and parameter estimation in induction motor drive systems," in *Int. Conf. on Control*, 1991, pp. 915-920.

[30] J. Stephan, M. Bodson, and J. Chiasson, "Real-time estimation of the parameters and fluxes of induction motors," *IEEE Trans. Ind. Appl.*, vol. 30, pp. 746-759, May-Jun. 1994.

[31] J. Jee-Hoon, J. Gang-Youl, and K. Bong-Hwan, "Stability improvement of V/f-controlled induction motor drive systems by a dynamic current compensator," *IEEE Trans. Ind. Electron.*, vol. 51, pp. 930-933, Aug. 2004.

[32] M. N. Uddin, R. S. Rebeiro, and L. Sheng Hua, "Online efficiency optimization of an IPMSM drive incorporating loss minimization algorithm and an FLC as speed controller," in *IEEE Int. Symp. on Ind. Electron.*, 2009, pp. 1263-1268.

[33] H. Hofmann and S. R. Sanders, "Optimal efficiency controller for synchronous reluctance flywheel drive," in *Int. Telecommun. Energy Conf.*, 1998, pp. 724-731.

[34] J. M. Prousalidis, N.D. Hatziargyriou, and B.C. Papadias, "On studying ship electric propulsion motor driving schemes," in *Int. Conf. on Power System Transients*, 2001, pp.1-7.

[35] M. Cacciato, A. Consoli, G. Scarcella, G. Scelba, and A. Testa, "Efficiency optimization techniques via constant optimal slip control of induction motor drives," in *Int. Symp. on Power Electron., Elect. Drives, Automation and Motion*, 2006, pp. 33-38.

[36] S. Ghozzi, K. Jelassi, and X. Roboam, "Energy optimization of induction motor drives," in *IEEE Int. Conf. on Ind. Technology*, 2004, pp. 602-610.

[37] F. Abrahamsen, F. Blaabjerg, J. K. Pedersen, P. Z. Grabowski, and P. Thogersen, "On the energy optimized control of standard and high-efficiency induction motors in CT and HVAC applications," *IEEE Trans. Ind. Appl.*, vol. 34, pp. 822-831, Jul.-Aug. 1998.

[38] "Using variable speed drives (VSDs) in pump applications," ABB, Helsinki 2006.

[39] "Adaptive energy optimization (AEO) for BD35F and BD50F compressors," Danfoss, Flensburg 2003.

[40] "Motor flux, the energy saving function and the operation of parameter P077 on the Eco," Munich: Siemens, 2010.

[41] "E7 drive programming manual," Yaskawa, New Berlin, WI 2008.

[42] G. O. Garcia, J. C. M. Luis, R. M. Stephan, and E. H. Watanabe, "An efficient controller for an adjustable speed induction motor drive," *IEEE Trans. Ind. Electron.*, vol. 41, pp. 533-539, Oct. 1994.

[43] L. Kawecki and T. Niewlerowicz, "Bi-criterial optimization in induction motors speed control taking into consideration the electromagnetic transients," in *IEEE Int. Symp. on Ind. Electron.*, 1996, pp. 935-939.

[44] I. Kioskeridis and N. Margaris, "Loss minimization in induction motor adjustable-speed drives," *IEEE Trans. Ind. Electron.*, vol. 43, pp. 226-31, Feb. 1996.

[45] J. Liu, L. Fei, S. Hu, and T. Q. Zheng, "Optimal efficiency control of linear induction motor for linear metro," in *IEEE Power Electron. Specialists Conf.*, 2008, pp. 673-677.

[46] C. Mademlis, I. Kioskeridis, and T. Theodoulidis, "Optimization of single-phase induction motors-part I: maximum energy efficiency control," *IEEE Trans. Energy Convers.*, vol. 20, pp. 187-95, Mar. 2005.

[47] A. Mannan, T. Murata, J. Tamura, and T. Tsuchiya, "Efficiency optimized speed control of field oriented induction motor including core loss," in *Power Conversion Conf.*, 2002, pp. 1316-1321.

[48] S. Seleme, A. doPrado, and A. Marques, "Sensorless speed control of induction motors with minimum loss," in *Int. Conf. on Control Applicat.*, 2002, pp. 114-119.

[49] G. Mino-Aguilar, J. M. Moreno-Eguilaz, B. Pryymak, and J. Peracaula, "An induction motor drive including a self-tuning loss-model based efficiency controller," in *IEEE Appl. Power Electron. Conf. and Expo.*, 2008, pp. 1119-1125

[50] T. Stefanski and S. Karys, "Loss minimisation control of induction motor drive for electrical vehicle," in *IEEE Int. Symp. on Ind. Electron.* vol. 2, 1996, pp. 952-957.

[51] S. Sujitjorn and K. L. Areerak, "Numerical approach to loss minimization in an induction motor," in *Appl. Energy Conf.*, 2004, pp. 87-96.

[52] E. Poirier, M. Ghribi, and A. Kaddouri, "Loss minimization control of induction motor drives based on genetic algorithms," in *IEEE Int. Elect. Machines and Drives Conf.*, 2001, pp. 475-478.

[53] A. M. Bazzi and P. T. Krein, "Input power minimization of an induction motor operating from an electronic drive under ripple correlation control," in *IEEE Power Electron. Specialists Conf.*, 2008, pp. 4675 - 4681.

[54] J. Miao, L. Huade, and S. Chen, "Study on efficiency optimization control of induction motor drive system," in *Control and Decision Conf.*, 2008, pp. 3244-3247.

[55] J. G. Cleland, V. E. McCormick, and M. W. Turner, "Design of an efficiency optimization controller for inverter-fed AC induction motors," in *IEEE Ind. Applicat. Conf.*, 1995, pp. 16-21.

[56] I. Kioskeridis and N. Margaris, "Loss minimization in scalar-controlled induction motor drives with search controllers," *IEEE Trans. Power Electron.*, vol. 11, pp. 213-220, Mar. 1996.

[57] P. Famouri and J. J. Cathey, "Loss minimization control of an induction motor drive," *IEEE Trans. Ind. Appl.*, vol. 21, pp. 32-37, Feb. 1991.

[58] D. S. Kirschen, D. W. Novotny, and T. A. Lipo, "On-line efficiency optimization of a variable frequency induction motor drive," *IEEE Trans. Ind. Appl.*, vol. IA-21, pp. 610-616, May 1985.

[59] T. Ohnishi, H. Miyazaki, and H. Okitsu, "High efficiency drive of an induction motor by means of V/F ratio control," in *IEEE Annu. Conf. of Ind. Electron. Soc.*, 1988, pp. 780-785.

[60] L. Ramesh, S. P. Chowdhury, S. Chowdhury, A. K. Saha, and Y. H. Song, "Efficiency optimization of induction motor using a fuzzy logic based optimum flux search controller," in *Int. Conf. on Power Electron., Drives and Energy Syst.*, 2006, pp. 1-6.

[61] A. H. B. M. Yatim and W. M. Utomo, "Neuro-fuzzy on-line optimal energy control for variable speed compressor motor drive system," in *Int. Conf. on Power Electron. and Drives Syst.*, 2005, pp. 776-780.

[62] D. L. Logue and P. T. Krein, "Machine efficiency optimization using ripple correlation control," in *IEEE Appl. Power Electron. Conf. and Expo.*, 2001, pp. 642-648.

[63] G. S. Kim, I. J. Ha, and M. S. Ko, "Control of induction motors for both high dynamic performance and high power efficiency," *IEEE Trans. Ind. Electron.,* vol. 39, pp. 323-333, Aug. 1992.

[64] V. T. Buyukdegirmenci, A. M. Bazzi, and P. T. Krein, "A comparative study of an exponential adaptive perturb and observe algorithm and ripple correlation control for real-time optimization," in *IEEE Workshop on Control and Modeling for Power Electron.*, pp. 1-8.

[65] P. Midya, P. T. Krein, and R. J. Turnbull, "Self-excited power minimizer/maximizer for switching power converters and switching motor drive applications," U. S. Patent 5,801,519, Sep. 1, 1998.

[66] J. Wells, P. L. Chapman, and P. T. Krein, "Applications of ripple correlation control of electric machinery," in *IEEE Int. Elect. Machines and Drives Conf.*, 2003, pp. 1498-1503.

[67] J. R. Wells, P. L. Chapman, and P. T. Krein, "Fundamental aspects of ripple correlation control of electric machinery," in *IEEE Power Electron. Specialist Conf.*, 2003, pp. 1659-1662.

[68] J. Bentsman, "Vibrational control of a class of nonlinear systems by nonlinear multiplicative vibrations," *IEEE Trans. Autom. Control,* vol. 32, pp. 711-716, Aug. 1987.

[69] P. T. Kabamba, S. M. Meerkov, and E. K. Poh, "Stability robustness in closed loop vibrational control," in *IEEE Conf. on Decision and Control*, 1993, pp. 1016-1017.

[70] R. Bellman, J. Bentsman, and S. Meerkov, "Vibrational control of nonlinear systems: vibrational stabilizability," *IEEE Trans. Autom. Control,* vol. 31, pp. 710-716, Aug. 1986.

[71] T. Esram, J. W. Kimball, P. T. Krein, P. L. Chapman, and P. Midya, "Dynamic maximum power point tracking of photovoltaic arrays using ripple correlation control," *IEEE Trans. Power Electron.,* vol. 21, pp. 1282-1291, Sept. 2006.

[72] J. W. Kimball and P. T. Krein, "Discrete-time ripple correlation control for maximum power point tracking," *IEEE Trans. Power Electron.,* vol. 23, pp. 2353-2362, Sept. 2008.

[73] K. P. Kroeger, C. Sanghun, A. M. Bazzi, B. B. Johnson, and P. T. Krein, "A digital implementation of continuous-time ripple correlation control for photovoltaic applications," in *Power and Energy Conf. at Illinois*, 2010, pp. 7-11.

[74] M. Rausand and A. Høyland, *System Reliability Theory: Models, Statistical Methods, and Applications*, 2nd ed. Hoboken, NJ: Wiley, 2005.

[75] M. B. d. R. Correa, C. B. Jacobina, E. R. C. da Silva, and A. M. N. Lima, "An induction motor drive system with improved fault tolerance," in *IEEE Ind. Applicat. Conf.*, 2000, pp. 2071-2077.

[76] L. Jingchuan, X. Longya, and Z. Zheng, "An adaptive sliding-mode observer for induction motor sensorless speed control," *IEEE Trans. Ind. Appl.,* vol. 41, pp. 1039-1046, Jul.-Aug. 2005.

[77] D. Kastha and B. K. Bose, "Fault mode single-phase operation of a variable frequency induction motor drive and improvement of pulsating torque characteristics," *IEEE Trans. Ind. Electron.,* vol. 41, pp. 426-433, Aug. 1994.

[78] J. Pontt, J. Rodriguez, J. Rebolledo, L. S. Martin, E. Cid, and G. Figueroa, "High-power LCI grinding mill drive under faulty conditions," in *IEEE IAS Annu. Meeting*, 2005, pp. 670-673.

[79] R. M. Tallam, D. W. Schlegel, and F. L. Hoadley, "Failure mode for AC drives on high resistance grounded systems," in *IEEE Appl.Power Electron. Conf. and Expo.*, 2006, pp. 1587-1591.

[80] V. P. Shevchuk, "Investigations of the operation reliability increase of the alternating current electric machines in diamond extractive industries," in *Int. Scientific and Practical Conf. of Students, Post-graduates and Young Scientists Modern Technique and Technologies*, 2002, pp. 103-104.

[81] Y. Yuexin and A. Y. Wu, "Transient response of electric drives under utility upset conditions," in *Annu. Pulp and Paper Ind. Tech. Conf.*, 1996, pp. 77-85.

[82] A. Fekih and F. N. Chowdhury, "A fault tolerant control design for induction motors," in *Int. Conf. on Syst., Man and Cybernetics*, 2005, pp. 1320-1325.

[83] D. Hirschmann, D. Tissen, S. Schroder, and R. W. De Doncker, "Reliability prediction for inverters in hybrid electrical vehicles," *IEEE Trans. Power Electron.*, vol. 22, pp. 2511-2517, Nov. 2007.

[84] R. Letchmanan, J. T. Economou, A. Tsourdos, I. A. Ashokaraj, and B. A. White, "Fault evaluation of relative-coupled BLDC drives for multi-facet mobile robot with distributed speed factors," in *IEEE Vehicle Power and Propulsion Conf.*, 2006, pp. 1-6.

[85] R. Bozzo, V. Fazio, and S. Savio, "Power electronics reliability and stochastic performances of innovative ac traction drives: a comparative analysis," in *IEEE Power Tech. Conf.*, 2003, p. 7.

[86] P. Wikstrom, L. A. Terens, and H. Kobi, "Reliability, availability, and maintainability of high-power variable-speed drive systems," *IEEE Trans. Ind. Appl.*, vol. 36, pp. 231-241, Jan.-Feb. 2000.

[87] R. D. Klug and M. Griggs, "Reliability and availability of megawatt drive concepts," in *Int. Conf. on Power Syst. Tech.*, 2004, pp. 665-671.

[88] J. C. Salmon and B. W. Williams, "A split-wound induction motor design to improve the reliability of PWM inverter drives," *IEEE Trans. Ind. Appl.*, vol. 26, pp. 143-150, Jan.-Feb. 1990.

[89] J. W. Bennett, A. G. Jack, B. C. Mecrow, D. J. Atkinson, C. Sewell, and G. Mason, "Fault-tolerant control architecture for an electrical actuator," in *IEEE Power Electron. Specialists Conf.*, 2004, pp. 4371-4377.

[90] S. Bolognani, L. Peretti, L. Sgarbossa, and M. Zigliotto, "Improvements in power line communication reliability for electric drives by random PWM techniques," in *IEEE Annu. Conf. on Ind. Electron.*, 2006, pp. 2307-2312.

[91] O. Wallmark, L. Harnefors, and O. Carlson, "Control algorithms for a fault-tolerant PMSM drive," *IEEE Trans. Ind. Electron.*, vol. 54, pp. 1973-1980, Aug. 2007.

[92] B. W. Williams, "High reliability 3-phase variable-frequency inverter," *IEE Proc. Elect. Power Applicat.*, vol. 129, pp. 353-354, Nov. 1982.

[93] G. F. D'Addio, S. Savio, and P. Firpo, "Optimized reliability centered maintenance of vehicles electrical drives for high speed railway applications," in *IEEE Int. Symp. on Ind. Electron.*, 1997, pp. 555-560.

[94] F. A. DeWinter, R. Paes, R. Vermaas, and C. Gilks, "Maximizing large drive availability," *IEEE Ind. Appl. Mag.*, vol. 8, pp. 66-75, Jul.-Aug. 2002.

[95] J. A. Oliver and D. Poteet, "High-speed, high-horsepower electric motors for pipeline compressors: available ASD technology, reliability, harmonic control," *IEEE Trans. Energy Convers.*, vol. 10, pp. 470-476, Sept. 1995.

[96] M. T. Abolhassani and H. A. Toliyat, "Fault tolerant permanent magnet motor drives for electric vehicles," in *IEEE Int. Elect. Machines and Drives Conf.*, 2009, pp. 1146-1152.

[97] S. Green, D. J. Atkinson, A. G. Jack, B. C. Mecrow, and A. King, "Sensorless operation of a fault tolerant PM drive," *IEE Proc. Elect. Power Appl.*, vol. 150, pp. 117-125, Mar. 2003.

[98] O. Jasim, C. Gerada, M. Sumner, and J. Arellano-Padilla, "Investigation of induction machine phase open circuit faults using a simplified equivalent circuit model," in *Int. Conf. on Elect. Machines*, 2008, pp. 1-6.

[99] K. S. Lee and J. S. Ryu, "Instrument fault detection and compensation scheme for direct torque controlled induction motor drives," *IEE Proc. Control Theory and Appl.*, vol. 150, pp. 376-382, Jul. 2003.

[100] O. Ondel, G. Clerc, E. Boutleux, and E. Blanco, "Fault detection and diagnosis in a set inverter induction machine through multidimensional membership function and pattern recognition," *IEEE Trans. Energy Convers.*, vol. 24, pp. 431-441, Jun. 2009.

[101] R. L. A. Ribeiro, C. B. Jacobina, E. R. C. Da Silva, and A. M. N. Lima, "Compensation strategies in the PWM-VSI topology for a fault tolerant induction motor drive system," in *IEEE Int. Symp. on Diagnostics for Elect. Machines, Power Electron. and Drives*, 2003, pp. 211-216.

[102] R. B. Sepe, Jr., B. Fahimi, C. Morrison, and J. M. Miller, "Fault tolerant operation of induction motor drives with automatic controller reconfiguration," in *IEEE Int. Elect. Machines and Drives Conf.*, 2001, pp. 156-162.

[103] W. G. Zanardelli, E. G. Strangas, and S. Aviyente, "Identification of intermittent electrical and mechanical faults in permanent-magnet AC drives based on time-frequency analysis," *IEEE Trans. Ind. Appl.*, vol. 43, pp. 971-980, Jul.-Aug. 2007.

[104] M. H. J. Bollen and P. M. E. Dirix, "Simple model for post-fault motor behaviour for reliability/power quality assessment of industrial power systems," *IEE Proc. Generation, Transmission and Distribution,,* vol. 143, pp. 56-60, Jan. 1996.

[105] W. Hainan, S. Pekarek, and B. Fahimi, "Multilayer control of an induction motor drive: a strategic step for automotive applications," *IEEE Trans. Power Electron.,* vol. 21, pp. 676-686, May 2006.

[106] M. Molaei, H. Oraee, and M. Fotuhi-Firuzabad, "Markov model of drive-motor systems for reliability calculation," in *IEEE Int. Symp. on Ind. Electron.*, 2006, pp. 2286-2291.

[107] K. J. P. Macken, I. T. Wallace, and M. H. J. Bollen, "Reliability assessment of motor drives," in *IEEE Power Electron. Specialists Conf.*, 2006, pp. 1-7.

[108] J. Liu, W.-l. Wang, and Y. Wang, "Research on FOC and DTC switching control of asynchronous motor based on parameter estimation," in *IEEE Int. Conf. on Automation and Logistics*, 2008, pp. 1754-1758.

[109] M. Ishiko and T. Kondo, "A simple approach for dynamic junction temperature estimation of IGBTs on PWM operating conditions," in *IEEE Power Electron. Specialists Conf.*, 2007, pp. 916-920.

[110] S. A. Kharitonov, M. A. Petrov, D. V. Korobkov, M. A. Maslov, and T. Y. Zhoraev, "A principle of calculation dynamic and static power losses with hard-switching IGBT," in *Int. Siberian Workshop and Tutorials on Electron Devices and Materials*, 2005, pp. 147-149.

[111] M. Kurokawa, Y. Konishi, H. Iwamoto, and M. Nakaoka, "Power loss estimations of voltage source three-phase soft switching inverter with resonant DC link assisted lossless snubber capacitor," in *Annu. Conf. of the IEEE Ind. Electron. Soc.*, 2000, pp. 350-355.

[112] A. Lakhsasi, Y. Hamri, and A. Skorek, "Partially coupled electro-thermal analysis for accurate prediction of switching devices," in *Candaian Conf. on Elect. and Comput. Eng.*, 2001, pp. 375-380.

[113] M. Musallam, P. P. Acarnley, C. M. Johnson, L. Pritchard, and V. Pickert, "Estimation and control of power electronic device temperature during operation with variable conducting current," *IET Circuits, Devices and Syst.,* vol. 1, pp. 111-116, Apr. 2007.

[114] U. Schwarzer and R. W. De Doncker, "Power losses of IGBTs in an inverter prototype for high frequency inductive heating applications," in *Annu. Conf. of the IEEE Ind. Electron. Soc.*, 2001, pp. 793-798.

[115] T. A. Stuart and Y. Shaoyan, "Computer simulation of IGBT losses in PFC circuits," *IEEE Trans. Aerosp. Electron. Syst.,* vol. 31, pp. 1167-1173, Jul. 1995.

[116] N. H. Kutkut, D. M. Divan, D. W. Novotny, and R. H. Marion, "Design considerations and topology selection for a 120-kW IGBT converter for EV fast charging," *IEEE Trans. Power Electron.,* vol. 13, pp. 169-178, Jan. 1998.

[117] D. A. Murdock, J. E. R. Torres, J. J. Connors, and R. D. Lorenz, "Active thermal control of power electronic modules," *IEEE Trans. Ind. Appl.*, vol. 42, pp. 552-558, Mar.-Apr. 2006.

[118] "General considerations: IGBT & IPM modules," Powerex application notes 2000.

[119] K. Berringer, J. Marvin, and P. Perruchoud, "Semiconductor power losses in AC inverters," in *IEEE IAS Annu. Meeting*, 1995, pp. 882-888.

[120] M. H. Bierhoff and F. W. Fuchs, "Semiconductor losses in voltage source and current source IGBT converters based on analytical derivation," in *IEEE Power Electron. Specialists Conf.*, 2004, pp. 2836-2842.

[121] A. Consoli, C. Licitra, S. Musumeci, A. Testa, F. Frisina, and R. Letor, "Comparative investigation on power losses in soft-switching insulated gate devices," in *Int. Symp. on Power Semiconductor Devices and ICs*, 1994, pp. 87-92.

[122] L. K. Mestha and P. D. Evans, "Optimization of losses in PWM inverters," in *Int. Conf. on Power Electron. and Variable-Speed Drives*, 1988, pp. 394-397.

[123] F. Blaabjerg, M. P. Kazmierkowski, M. Zelecehowski, D. Swierczynski, and W. Kolomyjski, "Design and comparison direct torque control techniques for induction motors," in *European Conf. on Power Electron. and Applicat.*, 2005, pp. 1-9.

[124] S. Yanqun, X. Yan, J. Jian, D. Yan, H. Xiangning, and Z. Zhaohui, "Switching loss analysis and modeling of power semiconductor devices base on an automatic measurement system," in *IEEE Int. Symp. on Ind. Electron.*, 2006, pp. 853-858.

[125] L. Abraham and M. Reddig, "Determination of switching losses in IGBTs by loss-summation-method," in *IEEE IAS Annu. Meeting*, 1995, pp. 1061-1068.

[126] S. Munk-Nielsen, L. N. Tutelea, and U. Jaeger, "Simulation with ideal switch models combined with measured loss data provides a good estimate of power loss," in *IEEE Ind. Applicat. Conf.*, 2000, pp. 2915-2922.

[127] J. W. Kimball, "Modeling controlled switches and diodes for electro-thermal simulation," in *IEEE Power Electron. Specialists Conf.*, 2005, pp. 2175-2179.

[128] X. Dewei, L. Haiwei, H. Lipei, S. Azuma, M. Kimata, and R. Uchida, "Power loss and junction temperature analysis of power semiconductor devices," *IEEE Trans. Ind. Appl.*, vol. 38, pp. 1426-1431, Sept.-Oct. 2002.

[129] U. Drofenik and J. Kolar, "A general scheme for calculating switching and conduction-losses of power semiconductors in numerical circuit simulations of power electronic systems," in *Int. Power Electron. Conf.*, 2005, CD-ROM, ISBN: 4-88686-065-6.

[130] B. Cassimere, S. D. Sudhoff, D. C. Aliprantis, and M. D. Swinney, "IGBT and PN junction diode loss modeling for system simulations," in *Int. Conf. on Electric Machines and Drives*, 2005, pp. 941-949.

[131] M. Leblanc, "Sur l'electrifaction des chemins de fer au moyen de courants alternatifs de frequence elevee," *Revue Generale de l'Electricite*, vol. 2, pp. 275-277, 1922.

[132] A. G. Ivakhnenko, "Problems of extremal control," *Avtomatika*, vol. 3, p. NA, 1956.

[133] V. P. Kazakov, "Studies of the dynamics of relay-pulse automatic control systems," *Automatic and Remote Control,* vol. 18, p. NA, 1957.

[134] R. Leyva, C. Alonso, I. Queinnec, A. Cid-Pastor, D. Lagrange, and L. Martinez-Salamero, "MPPT of photovoltaic systems using extremum-seeking control," *IEEE Trans. Aerosp. Electron. Syst.*, vol. 42, pp. 249-258, Jan. 2006.

[135] P. Tinglong, J. Zhicheng, and J. Zhenhua, "Maximum power point tracking of wind energy conversion systems based on sliding mode extremum seeking control," in *IEEE Energy 2030 Conf.* , 2008, pp. 1-5.

[136] M. Jankovic and S. Magner, "Optimization and scheduling for automotive powertrains," in *American Control Conf.*, 2004, pp. 4054-4059.

[137] Z. Chunlei and R. Ordonez, "Numerical optimization-based extremum seeking control with application to ABS design," *IEEE Trans. Autom. Control,* vol. 52, pp. 454-467, Mar. 2007.

[138] W. Hsin-Hsiung, S. Yeung, and M. Krstic, "Experimental application of extremum seeking on an axial-flow compressor," *IEEE Trans. Control Syst. Technol.*, vol. 8, pp. 300-309, Mar. 2000.

[139] P. T. Krein, "Ripple correlation control, with some applications," in *IEEE Int. Symp. on Circuits and Syst.*, 1999, pp. 283 - 286.

[140] C. S. Draper and J. T. Li, "Principles of optimalizing control systems and an application to internal combustion engine," *ASME Publications*, p. NA, 1951.

[141] I. S. Morosanov, "Methods of extremum control," *Automatic and Remote Control,* pp. 1077-1092, 1957.

[142] I. I. Ostrovskii and M. G. Eskin, "An extremum regulator for turbine boring of oil wells," *Automatic and Remote Control,* vol. 17, p. NA, 1956.

[143] L. A. Zalmanzon, "Some considerations on the production of pneumatic extremum regulators," *Automatic and Remote Control,* vol. 18, p. NA, 1957.

[144] M. Krstic and W. Hsin-Hsiung, "Stability of extremum seeking feedback for general nonlinear dynamic systems," *Automatica,* vol. 36, pp. 595-601, 2000.

[145] C. Olalla, M. I. Arteaga, R. Leyva, and A. El Aroudi, "Analysis and comparison of extremum seeking control techniques," in *Int. Symp. on Ind. Electron.*, 2007, pp. 72-76.

[146] J. Sternby, "Extremum control systems - an area for adaptive control?" in *Joint American Control Conf.*, 1980, pp. WA2-A.

[147] T. Ying, D. Nesic, I. Mareels, and A. Astolfi, "On global extremum seeking in the presence of local extrema," in *IEEE Conf. on Decision and Control*, 2006, pp. 5663-5668.

[148] A. Cocconi, S. Cuk, and R. D. Middlebrook, "High-frequency isolated 4kW photovoltaic inverter for utility interface," in *Seventh Int. PCI Conf.*, 1983, pp. 325-345.

[149] K. Ariyur and M. Krstic, *Real-Time Optimization by Extremum-Seeking Control*, 1st ed. Hoboken, NJ: Wiley, 2003.

[150] J. Y. Choi, M. Krstic, K. B. Ariyur, and J. S. Lee, "Stability of extremum seeking control for a class of discrete-time systems," in *IEEE Conf. on Decision and Control*, 2001, pp. 1717-1722.

[151] D. Nesic, T. Ying, and I. Mareels, "On the choice of dither in extremum seeking systems: a case study," in *IEEE Conf. on Decision and Control*, 2006, pp. 2789-2794.

[152] A. M. Bazzi, "Maximum power point tracking of multiple photovoltaic arrays," M.S. thesis, American University of Beirut, Beirut, Lebanon 2007.

[153] H. Patel and V. Agarwal, "Maximum power point tracking scheme for PV systems operating under partially shaded conditions," *IEEE Trans. Ind. Electron.*, vol. 55, pp. 1689-1698, Apr. 2008.

[154] P. C. Krause, O. Wasynczuk, and S. D. Sudhoff, *Analysis of Electric Machinery and Drive Systems*, 2nd ed. New York: Wiley - IEEE Press, 2002.

[155] "ABB drives for HVAC applications," ABB, New Berlin, WI, 2005.

[156] P. T. Krein, S. Splater, C. Hidrovo, and D. Logue, "Hybrid vehicle testing and simulation final report," Univ. Illinois, Tech. Rep. PAP-TR-97-6, Urbana, IL, Jul. 1997.

[157] R. C. Kroeze and P. T. Krein, "Electrical battery model for use in dynamic electric vehicle simulations," in *IEEE Power Electron. Specialists Conf.*, 2008, pp. 1336-1342.

[158] S. Choi, A. M. Bazzi, and P. T. Krein, "Ripple correlation control applied to electric vehicle regenerative braking," in *Power and Energy Conf. at Illinois*, 2010, pp. 88-92.

[159] S. Williamson, M. Lukic, and A. Emadi, "Comprehensive drive train efficiency analysis of hybrid electric and fuel cell vehicles based on motor-controller efficiency modeling," *IEEE Trans. Power Electron.*, vol. 21, pp. 730-740, May 2006.

[160] M. Amrhein, P. T. Krein, and B. I. Fierro, "Evaluation of a re-rated induction machine," in *IEEE Int. Conf. on Elect. Machines and Drives*, 2005, pp. 1400-1407.

[161] A. M. Bazzi and P. T. Krein, "Comparative evaluation of machines for electric and hybrid vehicles based on dynamic operation and loss minimization," in *IEEE Energy Conversion Congr. and Expo.*, 2010, pp. 3345-3351.

[162] Federal Urban Driving Schedule, U.S. Department of Transportation, http://www.epa.gov/nvfel/testing/dynamometer.htm, 2010.

[163] M. J. Tavernini, B. A. Niemoeller, and P. T. Krein, "Real-time low-level simulation of hybrid vehicle systems for hardware-in-the-loop applications," in *IEEE Vehicular Power and Propulsion Conf.*, 2009, pp. 890-895.

[164] T. J. McCoy, "Trends in ship electric propulsion," in *IEEE Power Eng. Soc. Transmission and Distribution Conf.*, 2002, pp. 343-346.

[165] P. Prempraneerach, J. Kirtley, C. Chryssostomidis, M. D. Triantafyllou, and G. E. Karniadakis, "Stochastic modeling of integrated power system coupled to hydrodynamics

in the all-electric ship," in *Int. Symp. on Power Electron., Elect. Drives, Automation and Motion*, 2008, pp. 563-568.

[166] C. Hodge, S. Williamson, and S. Smith, "Direct drive marine propulsion motors," in *Int. Conf. on Elect. Machines*, 2002, pp. 1421-1427.

[167] S. Lu and K. Corzine, "Multilevel multi-phase propulsion drives," in *IEEE Elect. Ship Tech. Symp.*, 2005, pp. 363-370.

[168] F. Terrien, S. Siala, and P. Noy, "Multiphase induction motor sensorless control for electric ship propulsion," in *Int. Conf. on Power Elect., Machines and Drives*, 2004, pp. 556-561.

[169] G. Diamantis and J. M. Prousalidis, "Simulation of a ship propulsion system with DTC driving scheme," in *Int. Conf. on Power Electron., Machines and Drives*, 2004, pp. 562-567.

[170] W. G. Bouricius, W. C. Carter, and P. R. Schneider, "Reliability modeling techniques for self-repairing computer systems," in *ACM Annu. Conf./Annu. Meeting*, 1969, pp. 295-309.

[171] A. M. Bazzi, A. Dominguez-Garcia, and P. T. Krein, "A method for impact assessment of faults on the performance of field-oriented control drives: A first step to reliability modeling," in *IEEE Appl. Power Elect. Conf. and Expo.*, 2010, pp. 256-263.

[172] A. F. Alshandoli, "Model-predicted induction motor behaviour under different operating conditions," in *Int. Conf. on Elect. Eng.*, 2007, pp. 1-7.

[173] D. Kastha and B. K. Bose, "Investigation of fault modes of voltage-fed inverter system for induction motor drive," *IEEE Trans. Ind. Appl.*, vol. 30, pp. 1028-1038, Jul.-Aug. 1994.

[174] A. D. Dominguez-Garcia, "An integrated methodology for the performance and reliability evaluation of fault-tolerant systems," Ph.D. Thesis, Massachusetts Institute of Technology, Cambridge, MA June 2007.

[175] *Military Handbook Reliability Prediction of Electronics Equipment*, MIL-HDBK-217F, Department of Defense, 1995.

[176] *IEEE Standard Reliability Data for Pumps and Drivers, Valve Actuators, and Valves*, ANSI/IEEE Std. 500, 1984.

[177] A. Ristow, M. Begovic, A. Pregelj, and A. Rohatgi, "Development of a methodology for improving photovoltaic inverter reliability," *IEEE Trans. Ind. Electron.*, vol. 55, pp. 2581-2592, Jul. 2008.

[178] E. M. Hope and A. D. Dominguez-Garcia, "Design verification of power electronics systems subject to bounded uncertain inputs," in *IEEE Energy Conversion Congr. and Expo.*, 2009, pp. 1126-1132.

[179] K. D. Jackson, M. D. McCulloch, and C. F. Landy, "A study of the suitability of electric drives to the task of driving conveyors," in *IEEE IAS Annu. Meeting*, 1993, pp. 488-495.

[180] A. M. Bazzi, X. Ding, A. D. Dominguez-Garcia, and P. T. Krein, "Circuit-based reliability model of an induction motor drive under different control schemes," in *IEEE Appl. Power Electron. Conf.*, 2010, to be published.

[181] P. T. Krein, F. Disilvestro, I. Kanellakopoulos, and J. Locker, "Comparative analysis of scalar and vector control methods for induction motors," in *IEEE Power Electron. Specialists Conf.*, 1993, pp. 1139 - 1145.

[182] A. M. Bazzi, J. W. Kimball, K. Kepley, and P. T. Krein, "TILAS: A simple analysis tool for estimating power losses in an IGBT-diode pair under hysteresis control in three-phase inverters," in *IEEE Appl. Power Electron. Conf. and Expo.*, 2009, pp. 637-641.

[183] AAVID Thermalloy, datasheet for product no. 62200, available at www.aavidthermalloy.com.

[184] "eZdsp(TM) F2812 technical reference 506265-0001 rev. F," Spectrum Digital, Stafford, TX, 2003.

[185] "C28x IQmath library: A virtual floating point engine V1.5a," Texas Instruments Dallas, TX, 2009.

[186] A. M. Bazzi and P. T. Krein, "Comprehensive flux estimator implementation procedures for advanced control of inverter-fed induction machines," in *Elect. Manufacturing and Coil Winding Conf.*, 2009, pp. 1-9.

[187] "Model DSP6001 high speed programmable dynamometer controller," Magtrol Inc., Buffalo, NY, 2010.

[188] "WT1600 digital power meter," Yokogawa Electric Corporation, Sugar Land, TX, 2009.